

Experimental Aspects and Mechanical Modeling Paradigms for the Prediction of
Degradation and Failure in Nanocomposite Materials Subjected to Fatigue Loading
Conditions

A Dissertation
Presented to
The Academic Faculty

by

Rodney D. Averett

In Partial Fulfillment
of the Requirements for the Degree
Doctor of Philosophy in the
School of Polymer, Textile, and Fiber Engineering

Georgia Institute of Technology
August 2008

Copyright 2008 by Rodney D. Averett

Experimental Aspects and Mechanical Modeling Paradigms for the Prediction of
Degradation and Failure in Nanocomposite Materials Subjected to Fatigue Loading
Conditions

Approved by:

Dr. Mary L. Realff, Co-Advisor
School of Polymer, Textile, and Fiber
Engineering
Georgia Institute of Technology

Dr. Karl Jacob, Co-Advisor
School of Polymer, Textile, and Fiber
Engineering
Georgia Institute of Technology

Dr. Meisha Shofner
School of Polymer, Textile, and Fiber
Engineering
Georgia Institute of Technology

Dr. Gary S. May
School of Electrical and Computer
Engineering
Georgia Institute of Technology

Dr. Samuel M. Graham
School of Mechanical Engineering
Georgia Institute of Technology

Date Approved: June 20th, 2008

To Grannie, “Buck,” Melody, Jordan, and Kaitlyn

ACKNOWLEDGEMENTS

I would like to thank the Almighty God, the Heavenly Father of the Universe for allowing this dream to become a reality. Without God's help, I would not have been able to complete the doctoral degree. Also, I would like to thank my wife (Melody) for all of her support and dedication throughout the years. It has been a long rough road, but we have finally made it! In the famous words of Mary J. Blige: "One day we'll look back on this, we'll be like remember this, and it's going to make us smile, because in the end we stay down!" We've been down for 13 years strong and still counting! Also, I would like to thank the chocolate drops in my life, Jordan and Kaitlyn Averett. You girls have made me realize what life is really about and the importance of family in one's life. I love you girls! Everyday that I would come home from the lab, I would look at you and think, "This is all worth it!"

I would also like to thank my mother and father (Corene and Jesse Averett) for all of their financial and moral support throughout these tumultuous years. I definitely could not have accomplished this task without all of your support and help. There were many times that I wanted to quit, but you all would just say, "Son, you'll have this behind you soon." Mom, there are two songs that come to mind now that this long journey has ended: "Dear Mama" by 2Pac and "I Made It" by Jay Z. Mama I made it! Mom, I appreciate all of your help. Whenever I needed you, you were just a phone call away. Daddy, I appreciate everything you've done for me financially, physically, and spiritually over these years. You always told me to persevere and that the end would come soon.

I also appreciate the moral support from my brothers and sister (Steve, Cheryl Lynn, and Anthony). You guys have been a great help and a great deal of support. Talking on the phone and discussing with you all some of the problems that I was having while in graduate school really helped to relieve my stress. Also, no matter what time of the day or night that I contacted you, you all took the time to listen to me and talk. I would also like to thank Mrs. Rose Walker for all of her help and support over the years while I was pursuing my Ph.D. All of your help and support has been greatly beneficial to both Melody and me throughout these years.

I would also like to thank my advisors Dr. Mary L. Realff and Dr. Karl Jacob for all of their support over the years. Dr. Realff, you and I have had a long journey on this road to the Ph.D. There have been some rough and rocky times, and there have been some beautiful and great times. I have learned a lot from you over the years. I know that we'll stay in contact and hopefully continue to work together on various projects in the future. Dr. Jacob, I would like to thank you for all of your advice about life and technical advice over the years. It has been very beneficial and I thank you sincerely. I also hope that we can collaborate on some projects in the future. I would also like to thank Dr. Meisha Shofner, Dr. Gary S. May, and Dr. Samuel Graham for serving on my committee and for providing me with helpful advice throughout this Ph.D. process. Dr. May, I would also like to thank you for allowing me to be a part of the FACES Program since being in undergraduate school at Georgia Tech. The mentorship and guidance that you have provided has helped me a lot through these years. I would also like to thank you for your advice on the computational aspects of my dissertation. I would also like to thank Dr. Satish Kumar at Georgia Tech and Dr. Miko Cakmak at the University of Akron for

collaborative research ideas and for supplying necessary materials and advice on completing my experimental research.

In terms of other associates, friends, and family members that have helped me throughout these years, I would like to thank: Dr. Anselm Griffin, Dr. William Wepfer, Dr. Stephen Michielsen, Dr. Iwona Jasiuk, Linda Roberson, Mike Boyett, Angie Abbott, Drew Buckingham, Lisa Shurtz, Ted Craig, Jamal Wilson, Calvin King, Roderick Jackson, Dr. Christopher Green, Marlon Bonner, Dr. Timothy Thornton, Dr. Thomas Brown, Dr. Dave Howerton, Dr. David Hall, Timothy Vines, Grandmother Martha Averett, Jeffrey Averett, James Averett, John Averett, Amanda Thornton, Geraldine Parris, Lucy Baldwin, Essie Francis, Ida Boykins, Martha Ann Patterson, Lois Swan, Raiford McCray, Robert McCray, Ardella Atkinson, Fred McCray, Janice Arrington, Eulysses Arrington, Aisha Arrington, Joyce Lee, Miranda Banks, Peggy Henry, Dr. Mike Edmondson, Charlie Jarrell, Jason Hamburg, and Anita Huff. Lastly, I would like to thank the Office of Naval Research Future Faculty Fellowship and the Ford Foundation Fellowship at the National Academies for funding that made my doctoral research possible.

TABLE OF CONTENTS

ACKNOWLEDGEMENTS.....	iv
LIST OF TABLES.....	xii
LIST OF FIGURES.....	xiii
SUMMARY.....	xix
CHAPTER 1 - INTRODUCTION.....	1
CHAPTER 2 - Literature review.....	5
2.1. Mechanical Fatigue of Polymeric Materials.....	5
2.1.1. Overview of Fatigue.....	5
2.1.2. Scatter in <i>S-N</i> curves.....	10
2.1.3. Mechanical and Fatigue of Poly(ethylene Terephthalate) (PET) Single Filaments.....	15
2.1.4. Fracture Behavior of PET and other Polymeric Single Filaments.....	16
2.2. Polymeric Nanocomposite Materials.....	17
2.2.1. Enhancements in Material Properties and Mechanical Behavior.....	17
2.2.2. Mechanical Behavior of Nanocomposite Fibers.....	18
2.2.3. Poly(lactic acid) Nanocomposite Films.....	20
2.3. Artificial Neural Networks (ANNs) – Applications in Mechanics and Engineering	21
2.3.1. Overview of ANNs.....	21
2.3.2. Applications of Neural Networks: Classification and Regression.....	24
2.3.3. Learning Paradigms in ANNs.....	26
2.3.4. Applications of genetic training algorithms in neural networks.....	28
2.3.5. Types of ANNs applied in engineering applications.....	30

2.3.6. ANNs Applied to Fatigue Behavior of Composites.....	31
2.4. Material Degradation due to Fatigue.....	34
2.4.1. Definition of Damage.....	34
2.4.2. Elastic Modulus Degradation.....	35
2.4.3. Inelastic strain.....	36
CHAPTER 3 - MECHANICAL AND FATIGUE BEHAVIOR OF POLY(LACTIC ACID) NANOCOMPOSITE FILMS.....	37
3.1. Experimental.....	37
3.1.1. Sample Preparation and Mechanical Testing.....	37
3.1.2. Light Transmission Experiments.....	38
3.2. Uniaxial Tensile Test Results.....	40
3.3. Results from DMA.....	43
3.4. Results from Light Transmission Experiments.....	45
3.5. Results from Constant Stress Fatigue.....	49
3.6. Further Discussion about Results from Fatigue of PLA and PLA Nanocomposite Samples.....	53
CHAPTER 4 - MECHANICAL AND FATIGUE BEHAVIOR OF POLY(ETHYLENE TEREPHTHALATE) (PET) AND NANOCOMPOSITE FIBERS: EXPERIMENTAL RESULTS.....	57
4.1. Introduction.....	58
4.2. Sample Preparation.....	59
4.3. Fatigue & Uniaxial Tensile Tests.....	60
4.4. Uniaxial Tensile Tests (Specimens Without Prior Fatigue)	61
4.5. Fatigue Experimentation Phase.....	66
4.6. Tensile Tests Subsequent to Load-Controlled Fatigue.....	69

4.7. Mechanical Tests Subsequent to Fatigue.....	72
4.7.1. Relative Tensile Stress Subsequent to Fatigue.....	72
4.7.2. Elastic Modulus Subsequent to Fatigue.....	75
4.7.3. Tensile Energy Analysis of Fibers in Uniaxial Tension Subsequent to Fatigue.....	77
4.7.4. Hardening Modulus Subsequent to Fatigue.....	79
4.7.5. Yield Strain Subsequent to Fatigue.....	81
4.8. SEM Fractography.....	83
4.9. Further Discussion.....	86
CHAPTER 5 - RESIDUAL PROPERTY PREDICTIONS OF PET AND PET-VGCNF FIBERS: MODELING AND PREDICTION USING ARTIFICIAL NEURAL NETWORKS.....	92
5.1. Introduction.....	93
5.2. Definition of Damage.....	94
5.3. Experimental Methods.....	95
5.3.1. Sample Preparation and Mechanical Testing.....	95
5.3.2. Application of Artificial Neural Networks (ANNs) - Introduction to ANNs	95
5.4. Learning Paradigms Used for Computation.....	96
5.4.1. Standard backpropagation and backpropagation with momentum learning..	96
5.4.2. Conjugate Gradient algorithm.....	99
5.5. Material Degradation due to Fatigue.....	100
5.5.1. Elastic Modulus Degradation.....	100
5.5.2. Inelastic strain.....	100

5.5.3. Neural Network Architecture for Prediction of Residual Mechanical Properties - PET Control Samples.....	103
5.5.4. Neural Network Architecture for Prediction of Residual Mechanical Properties – PET-VGCNF Samples.....	105
5.6. Results and Discussion.....	106
5.6.1. Results From Training and Testing Procedures.....	106
5.6.2. Residual Strength as a Function of Number of Cycles and residual strain – PET Control.....	109
5.6.3. Residual Strength as a Function of Number of Cycles and residual strain – PET-VGCNF.....	111
5.6.4. Mechanical Property Predictions of PET and PET-VGCNF Fibers Subsequent to Fatigue Loading as a Function of Residual Strain.....	113
5.7. Comparison of the Residual Mechanical Properties of PET Control and PET-VGCNF Fibers Under Various Loading Configurations.....	117
CHAPTER 6 - PREDICTING THE MECHANICAL BEHAVIOR OF PET AND PET-VGCNF FIBERS SUBSEQUENT TO FATIGUE LOADING USING GENETIC ARTIFICIAL NEURAL NETWORKS.....	123
6.1. Experimental.....	125
6.1.1. Sample Preparation and Mechanical Testing.....	125
6.1.2. Genetic neural network training.....	126
6.1.3. Artificial Neural Network (ANN) Computations.....	129
6.2. Results and Discussion.....	131
6.2.1. Results from Fatigue – DMA Results.....	131
6.2.2. Results from Fatigue – Fatigue in the Viscoelastic/Glassy Regime.....	132
6.2.3. Results from Fatigue - Training & Testing Results.....	134
6.2.4. Results for Prediction of Constitutive Response – Different Approach....	138
CONCLUSIONS OF DISSERTATION.....	145

FUTURE WORK.....	147
APPENDIX A.....	149
APPENDIX B.....	150
APPENDIX C.....	151
APPENDIX D.....	156
APPENDIX E.....	157
REFERENCES.....	158

LIST OF TABLES

Table 2.1. Characteristics of the NNs used in the numerical examples.....	13
Table 2.2. PMMA nanocomposite properties for two different grades of PMMA (PR-21-PS) and PR-24 PS.....	20
Table 3.1. Uniaxial tensile test results for poly(lactic acid) PLA neat films.....	40
Table 3.2. Uniaxial tensile test results for PLA films with 5 wt% nanoclay particles	41
Table 4.1. Properties of PET control and PET/VGCNF filaments at elongation rate of 10mm/min under uniaxial stress conditions without prior fatigue.....	62
Table 5.1. Nondimensional residual strength ANN performance data for PET Control samples, $R=0$, $\sigma_{max}=0.6\sigma_f$	108
Table 5.2. Nondimensional residual strength ANN performance data for PET-VGCNF samples, $R=0$, $\sigma_{max}=0.6\sigma_f$	108
Table 5.3. Elastic modulus degradation ANN performance data for PET control Samples, $R=0$, $\sigma_{max}=0.6\sigma_f$	109
Table 5.4. Elastic modulus degradation ANN performance data for PET-VGCNF samples, $R=0$, $\sigma_{max}=0.6\sigma_f$	109
Table 6.1. Upper and lower bound properties of step size, momentum, and PE element optimization parameters for genetic algorithm training.....	128
Table 6.2. Optimization summary results for GA neural networks-conjugate gradient (5-10-10-1 architecture) for PET-VGCNF samples.....	135

LIST OF FIGURES

Figure 2.1. Idealized deformation process in a linear viscoelastic solid depicting the residual strain that remains as a result of a constant load experiment.....	6
Figure 2.2. Idealized relaxation curve for a polymer.....	6
Figure 2.3. A typical S - N curve for prediction of failure.....	7
Figure 2.4. Stable stress-strain hysteresis loop.....	8
Figure 2.5. Elastic, plastic, and total strain vs. life curves.....	9
Figure 2.6. Plot showing heteroscedasticity of a variable.....	10
Figure 2.7. Actual fatigue data and NN estimated family of S - N curves for $P=(10, 50, \text{ and } 90\%)$ probabilities of failure at $K_t=2$ – Weibull distribution.....	13
Figure 2.8. Actual fatigue data and NN estimated family of S - N curves for $P=(10, 50, \text{ and } 90\%)$ probabilities of failure at different temperatures – Lognormal distribution.....	14
Figure 2.9. Tensile modulus of PAN/SWNT fibers as a function of SWNT content.....	19
Figure 2.10. Tensile modulus and strength of gel-spun PAN fibers as a function of draw ratio.....	19
Figure 2.11. Perceptron architecture composed of two layers of cells connected by synaptic weights.....	23
Figure 2.12. Architecture of ANN model.....	26
Figure 2.13. Basic procedure used for genetic algorithm training.....	28
Figure 2.14. Schematic representing how ANNs are used to estimate global (effective) properties in a metallic composite.....	33
Figure 2.15. Dependence of the asymptotic root-mean-square error, RMS_a , on the number of nodes of the hidden layer, n_h	33
Figure 2.16. Predicted non-dimensional applied stress, $(\sigma/\sigma_c)_p$, against actual non-dimensional applied stress, σ/σ_c , for the two ANN architectures examined.....	34
Figure 3.1. Example stress-strain curves of PLA neat and PLA 5wt% samples under uniaxial tensile loading conditions.....	41

Figure 3.2. Yield stress vs. particle volume fraction for polymer system with rigid CaCO_3 particles displaying the decrease as a function of particle volume fraction.....	42
Figure 3.3. tan delta and storage modulus vs. frequency for neat PLA sample and 5 wt% PLA sample.....	43
Figure 3.4. Stored and loss modulus vs. temperature for PLA neat and PLA 5 wt% samples.....	44
Figure 3.5. Tan delta vs. temperature for PLA neat and PLA 5 wt% samples.....	45
Figure 3.6. Uniaxial tensile test results: example light transmission vs. wavelength in the visible spectrum (360 nm-750 nm) for PLA 5 wt% sample tested under uniaxial loading to failure.....	46
Figure 3.7. Fatigue results: light transmission vs. wavelength for PLA neat and PLA 5 wt% nanocomposite samples.....	47
Figure 3.8. Percentage light transmission vs. maximum stress for PLA neat and PLA 5 wt% samples as a function of maximum fatigue stress.....	48
Figure 3.9. Maximum stress vs. number of cycles to failure (S-N curve) for PLA and PLA 5 wt% samples conducted at 3 Hz and 30 Hz.....	52
Figure 3.10. Empirical curves of time to failure vs. maximum fatigue stress for PLA neat and PLA 5 wt% samples.....	52
Figure 3.11. Envisioned process of microvoid coalescence-fibrillated fracture behavior in PP nanocomposite.....	54
Figure 4.1. Stress-strain curve results from uniaxial tensile tests on PET control & PET-VGCNF samples.....	63
Figure 4.2. Cox model prediction of the elastic modulus as a function of aspect ratio...	65
Figure 4.3. Stress-strain curve for material showing elastic and plastic regions depicting a method to determine the yield stress.....	66
Figure 4.4. Oscilloscope output of load vs. time and displacement vs. time response of PET control sample undergoing uniaxial sinusoidal loading (Prescribed load values: 0-8 g-stress ratio=0 (R=0))	68
Figure 4.5. Oscilloscope output of load vs. time and displacement vs. time response of PET/VGCNF sample undergoing uniaxial sinusoidal loading (Prescribed load values: 0-15 g-stress ratio=0 (R=0))	68

Figure 4.6. Dynamic mechanical analysis properties for PET control (C) and PET/VGCNF samples (9)	69
Figure 4.7. Residual stress-strain response of fibers in uniaxial tension subsequent to fatigue under various loading configurations.	70
Figure 4.8. Relative maximum stress of PET/VGCNF and PET Control samples in uniaxial tension (subsequent to fatigue) vs. residual strain for the R=0 loading condition	73
Figure 4.9. Relative maximum stress of PET/VGCNF and PET Control samples in uniaxial tension (subsequent to fatigue) vs. residual strain for the R=0.333 condition....	74
Figure 4.10. Representative elastic modulus of PET/VGCNF sample before and subsequent to fatigue (up to 1% strain)	75
Figure 4.11. Relative elastic moduli of PET control and PET/VGCNF samples (subsequent to fatigue) vs. residual strain for the R=0 loading condition.....	76
Figure 4.12. Relative elastic moduli of PET control and PET/VGCNF samples (subsequent to fatigue) vs. residual strain for the R=0.333 condition.....	77
Figure 4.13. Relative total energy of PET control and PET/VGCNF samples (subsequent to fatigue) vs. residual strain for the R=0 loading condition.....	78
Figure 4.14. Relative total energy of PET control and PET/VGCNF samples (subsequent to fatigue) vs. residual strain for the R=0.333 condition.....	79
Figure 4.15. Relative hardening modulus of PET control and PET/VGCNF samples (subsequent to fatigue) vs. residual strain for the R=0 loading condition.....	80
Figure 4.16. Relative hardening modulus of PET control and PET/VGCNF samples (subsequent to fatigue) vs. residual strain for the R=0.333 condition.....	81
Figure 4.17. Relative yield strain of PET control and PET/VGCNF samples (subsequent to fatigue) vs. residual strain for the R=0 loading condition.....	82
Figure 4.18. Relative yield strain of PET control and PET/VGCNF samples (subsequent to fatigue) vs. residual strain for the R=0.333 condition.....	83
Figure 4.19. (a) SEM fractograph of a PET unreinforced specimen without prior fatigue (uniaxial tensile fracture) and (b) specimen with prior fatigue and 0.024 (2.4%) residual strain from fatigue process indicated slight material degradation due to tiny microfailures along fiber axis.....	84
Figure 4.20. (a) SEM fractograph of a PET/VGCNF specimen without prior fatigue (uniaxial tensile fracture), (b) specimen with prior fatigue and 0.0078 (0.78%) residual	

strain from fatigue process indicated highly distorted and tortuous crack pattern and (c) PET/VGCNF specimen with prior fatigue and 0.0093 (0.93%) residual strain from fatigue process indicating defibrillation along the fiber axis.....86

Figure 5.1. Topology of a three-layer feedforward backpropagation network.....97

Figure 5.2. Example strain amplitude vs. time for specimen that underwent 5,000 cycles illustrating the creep evolution and retention of strain.....103

Figure 5.3. Schematic of ANN architecture used for prediction of residual mechanical properties in PET control samples.....105

Figure 5.4. PET control sample under $R=0$ conditions: 3-D schematic illustrating the nondimensional residual strength as a function of the number of cycles (N), and the residual strain (ϵ_R)110

Figure 5.5. Sensitivity analysis indicating the weak dependence of the residual strength on the number of cycles.....111

Figure 5.6. PET-VGCNF sample, $R=0$ conditions: 3-D schematic illustrating the nondimensional residual strength as a function of the number of cycles (N), and the residual strain (ϵ_R)112

Figure 5.7. PET control sample ($R=0$, $\sigma_{max}=0.6\sigma_f$): Actual experimental results and ANN production data sets (BP with momentum and conjugate gradient) of nondimensional residual modulus vs. the residual strain.....114

Figure 5.8. PET-VGCNF sample ($R=0$, $\sigma_{max}=0.6\sigma_f$): Actual experimental results and ANN production data sets (BP with momentum and conjugate gradient) of nondimensional residual modulus vs. the residual strain.....114

Figure 5.9. Comparison of the mechanical behavior of PET control and PET-VGCNF samples subsequent to fatigue loading utilizing ANN predictions based on BP with momentum and conjugate gradient algorithms.....115

Figure 5.10. Residual strength and elastic modulus degradation predictions of PET control and PET-VGCNF as a function of residual strain for $R=0$ and $R=0.333$ stress ratios ($\sigma_{max} = 0.6\sigma_f$) utilizing MLP ANN architecture and BP with momentum training algorithm.....118

Figure 5.11. Residual strength and elastic modulus degradation predictions of PET control samples at various residual strains ($\epsilon_R = 0.01$, $\epsilon_R = 0.05$, $\epsilon_R = 0.10$, $\epsilon_R = 0.15$) utilizing ANNs with BP with momentum training scheme.....120

Figure 5.12. Residual strength and elastic modulus degradation predictions of PET-VGCNF fibers at various residual strains ($\epsilon_R = 0.01$, $\epsilon_R = 0.05$, $\epsilon_R = 0.10$, $\epsilon_R = 0.15$)

utilizing ANNs with BP with momentum training scheme.....	121
Figure 6.1. Schematics of (a) unoriented amorphous polymer chains and (b) oriented amorphous polymer chains.....	125
Figure 6.2. Process flow for Genetic Algorithm (GA) training.....	126
Figure 6.3. Schematic of ANN architecture used in this study for prediction of constitutive behavior of the PET-VGCNF samples subsequent to fatigue.....	130
Figure 6.4. Representative DMA curve for PET-VGCNF sample indicating stiffness and phase angle vs. frequency.....	132
Figure 6.5. Results from fatigue tests at 50 Hz indicating the superior fatigue properties of the PET-VGCNF samples in the viscoelastic/glassy state.....	133
Figure 6.6. Randomized trial 1: Experimental stress (actual) vs. predicted stress from GA ANN for constitutive behavior prediction of samples representing good correlation	135
Figure 6.7. Randomized trial 2: Experimental stress vs. predicted stress from GA ANN for constitutive behavior prediction of samples representing overestimation of the predicted stress (poor correlation)	136
Figure 6.8. Genetic ANN sensitivity analysis of the input parameters for prediction of the constitutive behavior of PET-VGCNF samples.....	137
Figure 6.9. Results from Trials 1 and 2 from ANN genetic neural networks used to predict unfatigued and post-fatigue constitutive response of PET and PET-VGCNF fibers, indicating the poor capability of the ANN genetic procedure to capture the sharp transition in stress-strain behavior at ϵ_y	138
Figure 6.10. MSE vs. generation for 3 ANN genetic trials: hardening modulus ($H(X)$) prediction.....	140
Figure 6.11. Actual vs. ANN genetic predicted hardening modulus ($H(X)$) of PET & PET-VGCNF fibers.....	140
Figure 6.12. MSE vs. generation for 3 ANN genetic trials: yield strain ($\epsilon_y(X)$) prediction of PET & PET-VGCNF fibers.....	141
Figure 6.13. Actual vs. ANN genetic predicted yield strain ($\epsilon_y(X)$) of PET & PET-VGCNF fibers.....	141
Figure 6.14. MSE vs. generation for 3 ANN genetic trials: elastic modulus ($E(X)$) prediction of PET & PET-VGCNF fibers.....	142

Figure 6.15. Actual vs. ANN genetic predicted elastic modulus ($E(X)$) of PET & PET-VGCNF fibers.....	142
Figure 6.16. Representative normalized stress-strain curves of PET control and PET-VGCNF samples (experimental and GA neural network predictions) subsequent to fatigue loading. The data to the left of the curve prescribe the testing conditions of the sample.....	143
Figure 6.17. Idealized ANN architecture for prediction of number of cycles to failure (N_f) in PLA and PLA nanoclay films.....	147
Figure B.1. Example BP with momentum ANN architecture with various network parameters utilizing Neurosolutions modeling SW.....	150
Figure B.2. Example conjugate gradient ANN architecture with various network parameters using Neurosolutions modeling SW.....	150
Figure E.1. ANN structure for material property prediction of PET and PET-VGCNF fibers using GA training. Here $M(X)$ corresponds to the material property output (elastic modulus, hardening modulus, or yield strain).....	157

SUMMARY

The employment of polymeric materials reinforced with nano-sized reinforcing agents is ubiquitous throughout the science and engineering composites community. Spherical nanoparticles, single-walled nanotubes (SWNTs), double-walled nanotubes (DWNTs), multi-walled nanotubes (MWNTs), and vapor-grown carbon nanofibers (VGCNFs) are all excellent candidates for reinforcement of polymer matrices when advanced material performance is the objective. Obtaining beneficial mechanical property characteristics through utilization of reinforcing agents typically depends on several factors, to include:

- impurity concentration within the nano-agent or on the surface of the nano-agent
- cohesion between polymer matrix and reinforcing agent
- matrix-to-agent compatibility

In regards to the strength of nanocomposite materials under simple loading conditions, several researchers have investigated the strength and durability with respect to the aforementioned parameters [1-7]. In addition, the study of the strength/durability of polymeric nanocomposites tested under fatigue conditions has been conducted by researchers in [8-10]; however, it is not well established. Designers and manufacturers in the polymeric and nanocomposites community could benefit greatly from studies that relate the fatigue conditions to the residual strength and change in material properties. In addition, a specific qualitative methodology that evaluates whether the critical state of fracture in nanocomposites occurs through debonding or fracture of nanotubes from the polymeric surface could be a useful protocol for designers that seek to improve interfacial strengths.

CHAPTER 1

INTRODUCTION

The objective of the current research was to contribute to the area of mechanics of composite polymeric materials. This objective was reached by establishing a quantitative assessment of the fatigue strength and evolution of mechanical property changes during fatigue loading of nanocomposite fibers and films. Both experimental testing and mathematical modeling were used to gain a fundamental understanding of the fatigue behavior and material changes that occurred during fatigue loading. In addition, the objective of the study was to gain a qualitative and fundamental understanding of the failure mechanisms that occurred between the nanoagent and matrix in nanocomposite fibers. This objective was accomplished by examining scanning electron microscopy (SEM) fractographs. The results of this research can be used to better understand the behavior of nanocomposite materials in applications where degradation due to fatigue and instability of the composite under loading conditions may be a concern. These applications are typically encountered in automotive, aerospace, and civil engineering applications where fatigue and/or fracture are primary factors that contribute to failure.

Testing and modeling the evolution of damage and change to underlying microstructural properties in polymeric homogeneous and nanocomposite materials subjected to fatigue is a formidable task. For quantitative analysis, often times the researcher is given the task of associating a single variable or group of damage variables that can specifically map the changes to material structure. In reality, the problem of tracking material property and behavioral changes as a result of fatigue becomes computationally complex, since there are a plethora of testing conditions and variables

that can take on a range of values. For materials and structures that experience fatigue, the history of the material is often difficult to track and map because the materials often experience a variety of sporadic fatigue loads differing in magnitude and type. The goal of a true prognostic damage model should be to accurately identify a critical damage variable (or set of damage variables) that can be quantified and related to the overall degradation of the material.

For the fatigue research, the sole efforts of the research were not meant to merely replicate the fatigue-life experiments that are conducted on materials, where a relationship is sought for the stress level (amplitude) to the number of cycles to failure (typical S-N curve) [1-3]. In fact, for the current study, this type of analysis has been conducted on nanocomposite PLA films with success. These important analyses have yielded useful material characterization results to help researchers understand the response of these materials to fatigue. The objective of the research on the PLA nanocomposite films was to evaluate a biodegradable polymeric film (poly(lactic acid)) and its reinforced counterpart with nanoclay particles to assess the fatigue performance. Currently, there is a large gap in the literature with regards to research on fatigue of polymers reinforced nanoparticles. The current study addressed this gap by highlighting experimental and phenomenological aspects that can be utilized to address the failure in both unreinforced and nanocomposite fibers and films, which can then be extrapolated for use in the failure detection of other unreinforced and nanocomposite systems.

Although a very useful tool, fatigue-life data alone are not sufficient for describing the evolution of damage in nanocomposite materials under fatigue loading. Particularly, for single polymeric fibers, there is typically a large amount of scatter in S-N

curve behavior. Therefore, for the nanocomposite fibers, a residual strength fatigue model that tracked the evolution behavior of the materials was developed. In essence, the objective of the fatigue research on residual mechanical properties was to establish a quantitative assessment of the evolution of mechanical property changes during fatigue loading of nanocomposite fibers. The objective of the research on instability and fracture in nanocomposite fibers was to elucidate the degree of residual strength degradation using analytical methods and artificial neural networks (ANNs). These objectives were realized through the completion of the following tasks:

- 1) Unreinforced (homogeneous) and nanocomposite fibers were tested in uniaxial tension and uniaxial tensile fatigue to assess the residual strength and degradation mechanisms
- 2) The quantitative results were implemented into a phenomenological (mathematical) ANN model for the prediction of residual strength and mechanical property changes for various loading conditions

The major contributions to the scientific and engineering community that were realized at the conclusion of this research project include: An investigation of the fatigue performance of poly(lactic acid) unreinforced and nanocomposite films and the development of an assessment tool for monitoring and predicting damage accumulation in unreinforced and nanocomposite single fibers under fatigue loading. The literature and scientific community could benefit greatly from a fatigue study on unreinforced and nanocomposite materials subjected to fatigue loading. The scientific and research community could benefit greatly from a systematic and more robust method for predicting failure in materials subjected to fatigue loading. Currently, the methods that

have been reviewed in the literature do not take into consideration damage that evolves as a result of the fatigue loading process. Instead, the conventional fatigue models assume that fatigue life is a random variable that exhibits a functional dependency on the maximum stress and other test variables. Although these methods have proven sufficient over the years, the application is quite limited because in some cases the fatigue life distribution can be separated by an order of magnitude difference. The current approach has utilized both fatigue life models and damage variables such as inelastic strain and modulus degradation to monitor the changes in fracture strength and other constitutive properties as a result of the fatigue loading process.

Although there is some research that exists on the topics of fatigue in nanocomposites [4-7], there have been very few studies that have investigated the residual strength decreases as a function of fatigue variables and a damage variable(s). In terms of single nanocomposite fibers, there has been even less research conducted in the area of fatigue with the utilization of mathematical tools to monitor changes in residual strength and other mechanical properties. The purpose of the fatigue research was to provide value to scientists and engineers that wish to design better and more robust materials that can withstand cyclic stresses and strains in engineering applications.

CHAPTER 2

LITERATURE REVIEW

2.1. Mechanical Fatigue of Polymeric Materials

2.1.1. Overview of Fatigue

The process of fatigue that is conducted for performance evaluation of materials entails subjecting the materials to a series of load-unload iterations for a prescribed number of cycles. The dynamic stress-strain response of a viscoelastic polymer sample under fatigue conditions is given as:

$$\begin{aligned}\varepsilon &= (\Delta\varepsilon)\sin\omega t \\ \sigma &= (\Delta\sigma)\sin(\omega t + \delta)\end{aligned}\tag{2.1}$$

In this formulary, ε is the instantaneous strain, $\Delta\varepsilon$ is the strain amplitude, ω is the angular frequency, σ is the instantaneous stress, $\Delta\sigma$ is the stress amplitude, and δ is the phase lag component of the stress and strain. In ordinary polymer materials, typically the strain lags behind the stress response due to the viscous component of the sample. One can envision that this phase lag, δ , of the strain component is the direct result of the imaginary viscous dashpot inhibiting the strain function from being directly in phase with the applied sinusoidal stress. Fatigue tests are either tested in load control or displacement control, depending upon the nature of the test and the desired results. For load controlled experiments, subsequent to an initial step strain input, the mean cyclic amplitude of the strain will increase with time (cycles) to compensate for the fixed amplitude of stress. This phenomenon is analogous to the creep evolution that occurs in polymers that are exposed to a constant static stress for a long period of time (Figure 2.1).

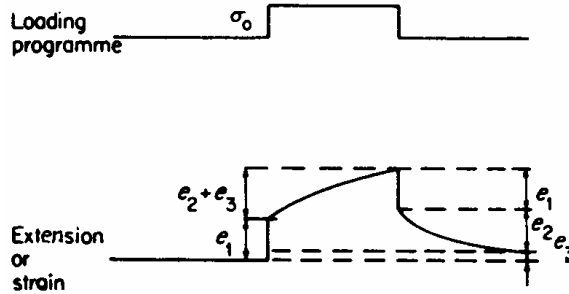


Figure 2.1. Idealized deformation process in a linear viscoelastic solid depicting the residual strain that remains as a result of a constant load experiment [8]

If the fatigue tests are conducted in displacement (or strain) control, the mean value of the cyclic load of the viscoelastic sample will experience a relaxation phenomenon, in which the macroscopic stress on the polymer chains relaxes to compensate for the fixed amplitude of strain. This fatigue relaxation phenomenon is equivalent to the relaxation behavior observed in conventional polymer systems (Figure 2.2).

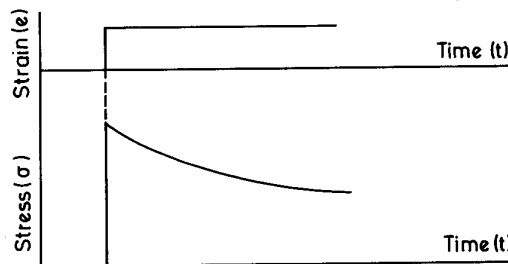


Figure 2.2. Idealized relaxation curve for a polymer [8]

Mechanical fatigue conducted on polymeric materials is typically conducted to determine a relationship of the resistance of the material under various cyclic load amplitudes to the number of cycles to failure. Early studies related to fatigue on polymeric materials were conducted to generate S versus N (stress vs. number of cycles to failure) curves. These studies were useful for predictions of fatigue life in metallic

materials [8]. A depiction of a typical S vs. N curve is shown in Figure 2.3. To develop this relationship, multiple experiments were run at various maximum stress levels to determine the number of cycles of endurance for a particular specimen.

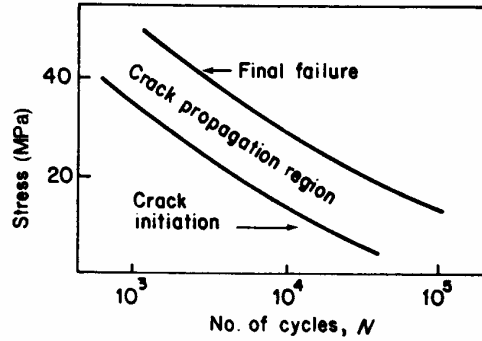


Figure 2.3. A typical S - N curve for prediction of failure [8]

Primordial studies that were conducted on polymers were mainly focused on rubber materials [9-11]. In these studies, a tearing energy fracture concept was applied based on quantitative analyses of Rivlin and Thomas [8]. A power-law fatigue crack growth empirical law was established as:

$$\frac{dc}{dN} = A \zeta^n \quad (2.2)$$

In (2.2), c is the crack length, N represents the number of cycles, ζ is the surface work parameter, and A and n are material parameter constants. This type of analysis is equivalent to the strain-energy release rate/stress intensity analysis that is conducted for linear elastic fracture mechanics problems [12].

Typically, Coffin-Manson curves are utilized to establish a relationship between the strain amplitude and the number of cycles to failure. Strain amplitude based fatigue life prediction is based upon Coffin-Manson curves that are obtained from isothermal

mechanical fatigue testing. The Coffin–Manson equation is a strain-life based fatigue formula and is given as [13-14]:

$$\varepsilon_a = \frac{\sigma_f'}{E} (2N_f)^b + \varepsilon_f' (2N_f)^c \quad (2.3)$$

This Coffin-Manson equation can be partitioned into two strain components, namely elastic and plastic strains, that are engendered based upon the maximum stress level that the polymeric sample experiences under fatigue deformations:

$$\varepsilon_a = \varepsilon_{ea} + \varepsilon_{pa} \quad (2.4)$$

In these equations, ε_a represents the strain range, σ_f' is the fatigue strength coefficient, E is the elastic modulus, N_f represents the number of cycles to failure, ε_f' is the fatigue ductility coefficient, b is the fatigue strength exponent, and c is the fatigue ductility exponent. In Equation 2.4, ε_{ea} represents the elastic component of the strain amplitude and ε_{pa} represents the plastic component of the strain amplitude. A pictorial representation of the cyclic stress-strain hysteresis response of a sample undergoing deformation is shown below in Figure 2.4.

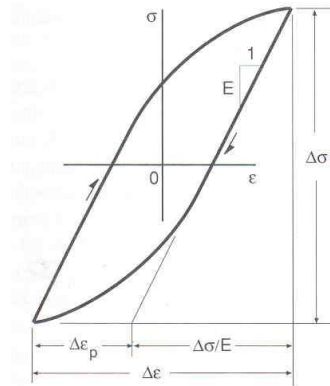


Figure 2.4. Stable stress-strain hysteresis loop [13]

In addition, a strain-amplitude vs. cycles to failure plot is provided in Figure 2.5, which represents a pictorial amalgam of the results from the Coffin-Manson equations and the hysteresis loop in Figure 2.4.

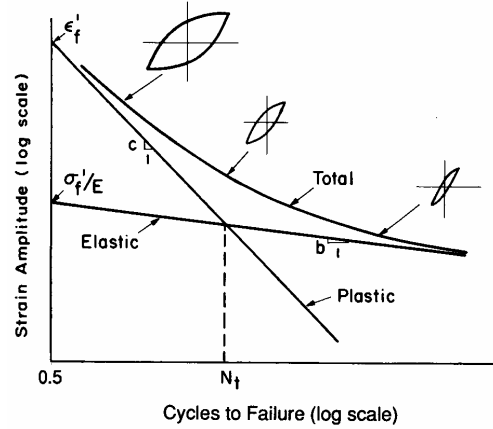


Figure 2.5. Elastic, plastic, and total strain vs. life curves [13]

As mentioned earlier, mechanical fatigue conducted on polymeric systems is quite different from that of metals, ceramics, or other brittle materials because the time dependent (viscous) nature of the samples is a prevailing factor that governs failure. Because of this strong time dependency, it is quite important to understand that the properties of polymeric materials are dependent upon the cyclic stress conditions and may not be static throughout the duration of the test. This is the significant drawback of utilizing $S-N$ curve and Coffin-Manson analyses alone for prediction of failure in polymeric materials. For example, the elastic portion of the Coffin-Manson relationship that was presented above assumes a static modulus E . However, as will be shown later, the modulus of a polymer material that undergoes mechanical cycling experiences severe degradation over the duration of the test and will change significantly, thus altering the prediction of the number of cycles to failure, N_f . In addition, the residual strength of the

material degrades over the duration of the experiment. In a load-controlled fatigue experiment, the value of R (load ratio) would thus be an increasing function over the duration of the test, due to the fact that the residual strength degrades with successive fatigue iterations.

2.1.2. Scatter in S - N curves

Fatigue life curves that provide information about the number of cycles to failure for a particular stress level typically contain large amounts of scatter in the data. In fact, fatigue data is widely known to be heteroscedastic in nature, which means that the scatter becomes more pronounced for longer fatigue lives. See Figure 2.6 for an example of heteroscedasticity of a functional variable.

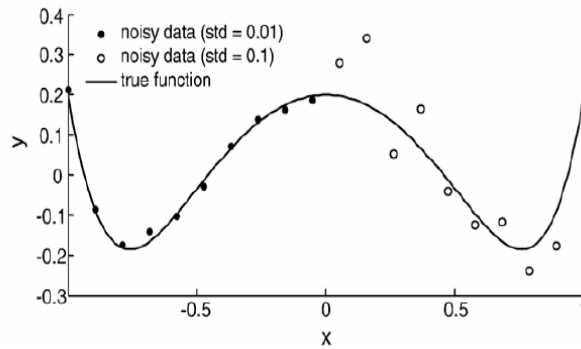


Figure 2.6. Plot showing heteroscedasticity of a variable [15]

Several researchers have attempted to explain heteroscedastic behavior in S - N curve data and how the fatigue life, N_f , is a random variable for a particular stress level [16-19]. Authors in [20] have expounded upon this notion that fatigue life is a random variable with the application of stress for a given amplitude. In addition, the authors in [21] have

proposed that in the randomness of the fatigue resistance of a material, constant amplitude fatigue test results show that at any stress amplitude s , the fatigue life N_{sf} is a random variable. Lognormal or other statistical distribution functions are typically used to describe the variability of the fatigue life. In [21], it is proposed that the fatigue damage, D_{sf} , caused by a cycle is also a random variable that is related to N_{sf} as:

$$D_{sf} = \frac{1}{N_{sf}} \quad (2.5)$$

In addition to these studies, Dowling in [13] has devoted a large portion of the text explaining that for various influential factors there is considerable statistical scatter in the data.

Recently, some research has been conducted using ANNs to explain and predict the scatter observed in fatigue-life data by Bucar et al [22-23]. In [22], Bucar et al. explain that in the randomness of fatigue resistance of a material, constant amplitude fatigue test results dictate that at any stress level the fatigue life is a random variable. To explain this concept of randomness in the number of cycles to failure, N_f , consider the following explanation utilizing the probability distribution concept (p.d.f.) derived in [22]:

Let \mathbf{X} represent a column vector of influential factors in a fatigue test such as S_{max} (maximum stress), S_m (mean stress), K_t (notch factor), frequency, etc:

$$\mathbf{X} = (X_1, X_2, \dots, X_p)^T = (S_{max}, S_m, K_t, F, \dots)^T \quad (2.6)$$

Here, \mathbf{X} is a random variable and the complete description of the problem of mapping the input to output variables can be described through a joint p.d.f. of the form:

$$f_{XY}(x, y) = f_{Y|X}(y|x) \cdot f_X(x) \quad (2.7)$$

Here, $f_{Y/X} = f(y/x)$ is the p.d.f. of Y given that X takes on a particular value and $f_X(x)$ represents the unconditional p.d.f. of X .

To implement the scatter and distribution of the fatigue lives, the authors in [22] expressed the error function in the neural network in terms of either a Weibull distribution or a lognormal distribution as (*Please refer to Section 2.3 of this document for a thorough explanation of neural networks and applications*):

$$f(y|x) = \sum_{l=1}^M \alpha_l(x) \cdot \frac{\beta_l(x)}{\theta_l(x)} \left(\frac{y}{\theta_l(x)} \right)^{\beta_l(x)-1} \exp \left\{ - \left(\frac{y}{\theta_l(x)} \right)^{\beta_l} \right\} \quad (\text{Weibull distribution}) \quad (2.8)$$

$$f(y|x) = \sum_{l=1}^M \alpha_l(x) \frac{1}{\sqrt{2\pi}\sigma_l(x)y} \exp \left\{ - \frac{(\log y - \mu_l(x))^2}{2\sigma_l^2(x)} \right\} \quad (\text{Lognormal distribution}) \quad (2.9)$$

In these distribution functions, β_l and θ_l represent the Weibull shape and scale parameters of the l th component distribution, and μ_l and σ_l represent the mean and standard deviation of $\log(Y)$ of the l th lognormal distribution. The functional relationship between the vector \mathbf{x} and the p.d.f. $f(y/x)$ is determined by values of the synaptic weights w_{ij} of the multilayer perceptron neural network through minimization of the cost function (error function). The statistical distributions (Weibull and lognormal) are implemented into the error function as:

$$E(N) = \sum_{n=1}^N e(n) \quad (2.10)$$

$$e(n) = -\ln \left[\sum_{l=1}^M \alpha_l(x_n) \cdot f_l(y_n|x_n) \right] \quad (2.11)$$

Estimations of the fatigue life were calculated for both the Weibull and lognormal distributions and the characteristics of the networks are shown in Table 1. Figures 2.7

and 2.8 display actual data and neural network estimation data for a family of S - N curves for the Weibull and lognormal distributions, respectively.

Table 2.1. Characteristics of the NNs used in the numerical examples [22]

Table 2 Characteristics of the NNs used in numerical examples		
Configuration of the neural network	Example no. 1	Example no. 2
Size of input layer, N_i	3	2
Type of component distributions in a $f(y x)$	Weibull	Lognormal
No. of component distributions in a $f(y x)$	1	1
No. of hidden layers of neurons	1	1
No. of neurons in hidden layers, N_j	4	2
Activation functions of hidden neurons, φ_j	Tanh	Tanh
No. of neurons in output layer, N_k	3	3
Activation functions of output neurons, φ_k	Linear	Linear
Initial rate of learning, η	0.0001	0.0005
Momentum of learning α	0.05	0.05
Value of parameter, κ	10^{-6}	10^{-6}
Value of parameter, ψ	0.5	0.5
Value of parameter, ξ	0.7	0.7
No. of epochs till the end of the learning	260,000	140,000
Final value of the error function $E(n)$	-425.6	-59.1

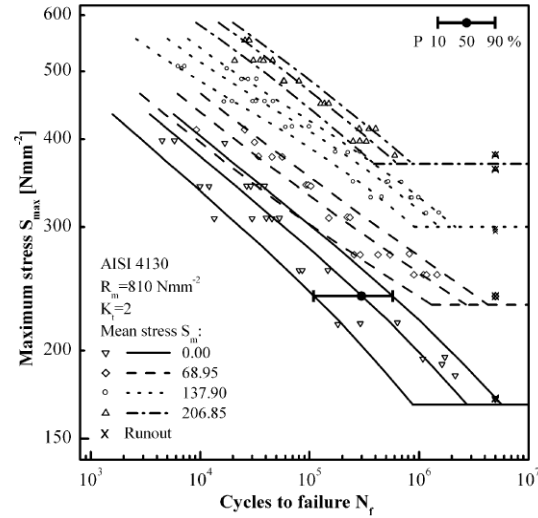


Figure 2.7. Actual fatigue data and NN estimated family of S - N curves for $P=(10, 50, \text{ and } 90\%)$ probabilities of failure at $K_t=2$ – Weibull distribution [22]

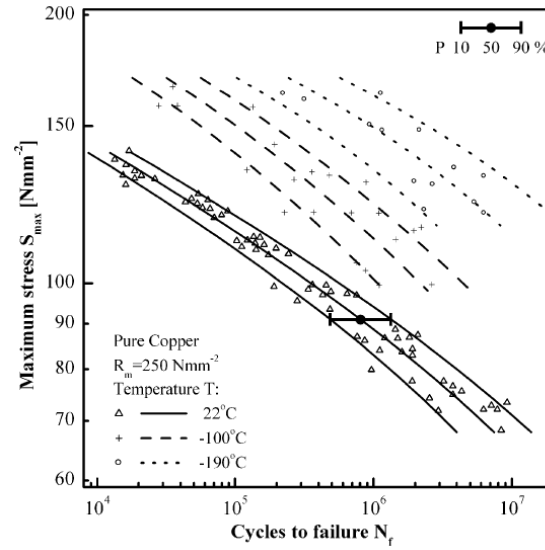


Figure 2.8. Actual fatigue data and NN estimated family of S–N curves for P= (10, 50, and 90%) probabilities of failure at different temperatures – Lognormal distribution [22]

These studies by Bucar et al [22-23] indicate that neural network algorithms can be utilized to predict the scatter in *S-N* curves through implementation of statistical distribution functions such as Weibull and lognormal. These statistical distribution functions were implemented into minimization of the cost (error) function to quantitatively capture the scatter behavior of the fatigue life. However, these recent studies, as well as conventional fatigue studies do not address the underlying damage accumulation that leads to failure in materials. In this dissertation, a different approach will be described that seeks to utilize damage parameters as input variables for a more consistent prediction of failure strength in neat (unreinforced) and nanocomposite materials.

2.1.3. Mechanical and Fatigue of Poly(ethylene Terephthalate) (PET) Single Filaments

Some interesting observations have been made regarding the physical degradation of PET, unreinforced fiber samples [24-26]. In addition, Cho et al. [27] studied the fatigue behavior of unreinforced PET fibers under various processing conditions with the same crystal structure at 10^4 - 10^6 cycles. Thermoluminescence (TL) glow experiments under various fatigue proved that the strain hardening effect was the culprit of enhanced TL glow at early stages of the fatigue process and defect sites were responsible for enhanced glow at later stages in the fatigue process. In essence, they showed that the strain hardening effect altered the stress-strain curve of PET in the early stages of fatigue; however, its effect attenuated after a certain point in the cyclic experiments. They also showed that the viscosity molecular weights were reduced with the increase of the number of fatigue cycles. This effect was attributed to chain scission of the PET molecules during cycling. Other efforts to illuminate the effects of fatigue on the accumulation of damage in PET fibers have been investigated in [28], in which destructive tests were performed. In their experiments, the ultimate failure of PET fibers after 4.22E6 cycles was due to the presence of a congenital, inherent flaw hypothesized to be antimony trioxide (Sb_2O_3), which was used as a catalyst in the production of PET. Liang et al. [29] investigated the effects of chain rigidity on the nonlinear viscoelastic behavior of several polymeric fibers, to include PET. They concluded that the nonlinear viscoelasticity was strongly governed by the rigidity of the chain, with semirigid structures such as PET exhibiting a NVP (nonlinear viscoelastic parameter) between flexible polymeric fibers (Nylon 6 and PVA) and rigid polymers (Vectran and Kevlar). In essence, they showed that NVP increased with increasing chain rigidity. Liang et al.

[29] also concluded that irreversible structural changes occurred faster in polymeric fibers with higher NVP values, thus indicating shorter fatigue lifetimes with increasing molecular chain rigidity. Le Clerc et al. [30] have investigated the response of mechanical properties to changes in temperature for unreinforced PET fibers and assemblies under various loading conditions. Specifically, they determined that for fiber assemblies initially at room temperature ($\sim 20^{\circ}\text{C}$), a temperature rise was observed during fatigue experiments conducted at 50 Hz. The temperature rise was shown to be an increasing function of the maximum stress/load amplitude during fatigue loading and was also dependent on the median stress value (for the same load amplitude, higher maximum temperatures were observed for lower mean loads). Lechat et al. [24] conducted fatigue experiments on PEN (polyethylene naphthalate) and PET fibers at 50 Hz and compared those with creep experiments to demonstrate that static creep lifetimes tested at 70% of the fracture strength were much higher than cyclic lifetimes tested under stress-controlled conditions.

2.1.4. Fracture Behavior of PET and other Polymeric Single Filaments

Some authors have performed past microscopy investigations on single fibers to ascertain failure modes. Particularly, Hearle [31-33] has performed an extensive mechanical testing and SEM study on various polymeric fibers to determine modes of failure. In addition, the authors in [34-43] have performed extensive studies on the fracture performance and mechanical behavior of single polymeric filaments.

In terms of quantitative mechanics studies conducted on single polymeric filaments, there has been limited research and investigations. Michielsen [44] has

investigated the fracture behavior of larger nylon 66 fibers (900 μm wide and 250 μm depth), where the critical strain energy release rate (G_{Ic}) for highly oriented filaments was 17.8 kJ/m^2 . As a comparison, the critical energy release rate for dry as molded (DAM) low-orientation bulk samples was 3.9 kJ/m^2 , as described in [45]. Michielsen [46] also examined the effects of relative humidity (RH) on the strain energy release rate of nylon 66 fibers, where it was shown that increases in RH engendered a decrease in the initial modulus (E_i) and critical strain energy release rate (G_{Ic}) of the samples. In that study, G_{Ic} varied from 31.3 kJ/m^2 at 0% RH to 15.6 kJ/m^2 at 100% RH.

2.2. Polymeric Nanocomposite Materials

2.2.1. *Enhancements in Material Properties and Mechanical Behavior*

Many studies have been conducted on nanocomposite samples under simple loading conditions to ascertain the effects of filler content on the mechanical properties. Sandler et al. [47] have performed uniaxial tensile experiments on melt-spun polyamide 12 fibers employed with various reinforcing agents, to include arc-grown nanotubes (AGNT), aligned catalytically grown nanotubes (aCGNT), entangled catalytically grown nanotubes (eCGNT) and catalytically grown nanofibers (CNF). In all cases, the modulus and yield stress of the nanocomposites were shown to be higher than the unreinforced polyamide 12 fiber, and the values were shown to be linearly correlated with the filler content (increases in modulus and yield strength with increased filler content). The eCGNT reinforced polyamide 12 composites showed the most significant improvements in modulus (1.6 GPa) and yield strength (45 MPa) at a filler content of 10% in comparison with a modulus of 0.8 GPa and yield strength of 21 MPa for the unreinforced

polyamide 12. Breton et al [48] have also noticed significant increases in modulus with decreases in the ultimate strain and fracture strength for epoxy/MWNT composites. This clearly indicates that filling the epoxy with MWNTs led to stiffer and more brittle materials. Other evidence has been provided by Wuite and Adali [49], Chen and Tao [50], and Kim et al. [51] that indicates stiffening of the polymer matrix due to the inclusion of nano-sized reinforcing agents under simple loading conditions. What can be concluded from these studies is that nano-sized reinforcing agents increase the mechanical properties and overall mechanical behavior of the materials for engineering applications.

2.2.2. Mechanical Behavior of Nanocomposite Fibers

In terms of single nanocomposite fibers for engineering applications, Chae et al. [52] have investigated the employment of SWNTs into a PAN matrix with various concentrations. The tensile modulus was shown to be almost linearly correlated with the volume fraction of the reinforcement material, with variations of 0% (control PAN), 0.4%, and 0.8% of SWNT volume fraction (Figure 2.9). In addition, the tensile modulus and strength were shown to be an approximate linearly increasing function of the draw ratio of the fiber, up to 40X, where the modulus and strength values began to plateau with increases in draw ratio (Figure 2.10).

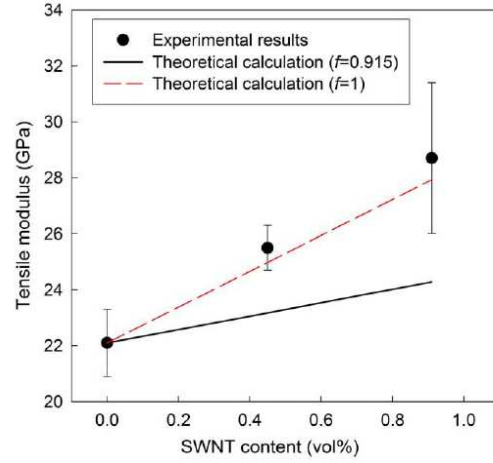


Figure 2.9. Tensile modulus of PAN/SWNT fibers as a function of SWNT content [52]

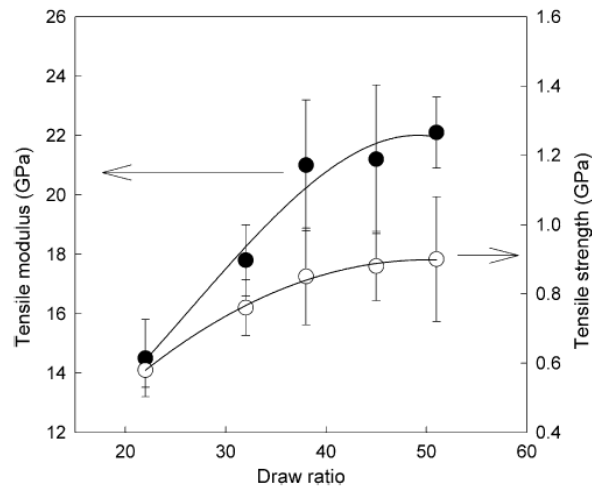


Figure 2.10. Tensile modulus and strength of gel-spun PAN fibers as a function of draw ratio [52]

Reinforcement efficiency studies of PAN fiber with 5 wt% SWNT bundles (20, 10, and 4.5 nm), SWNTs (1 nm), DWNTs (5 nm), MWNTs (20 nm), and VGCNFs (20 nm) have also been conducted by Chae et al [53], where X-ray diffraction, raman spectroscopy, scanning electron microscopy (SEM), tensile tests, DMA, and thermal shrinkage tests were conducted in this research. Improvements in mechanical properties (tensile, DMA,

and thermal shrinkage) were observed for all reinforcing agents. Zeng et al. [54] have also investigated CNFs for increases in mechanical properties of a PMMA fiber matrix. Two different grades of CNFs were employed in the PMMA matrix and Table 2.2 displays the results indicating increases in mechanical properties (PR-21-PS and PR-24-PS). The PR-21-PS grade possessed a larger diameter than PR-24-PS. Other researchers [55-59] have also successfully processed single polymeric fibers with nano-sized reinforcing agents to obtain enhancements in mechanical properties.

Table 2.2. PMMA nanocomposite properties for two different grades of PMMA (PR-21-PS) and PR-24-PS

Sample	Diameter (μm)	Tensile modulus (GPa)	Tensile strength (GPa)	Elongation at break (%)	Compressive strength
PMMA control	60 ± 4	4.7 ± 1.5	0.20 ± 0.04	16 ± 3	28 ± 2
PMMA/PR-21-PS 5 wt%	61 ± 12	8.0 ± 1.2	0.17 ± 0.04	10 ± 6	73 ± 11
PMMA/PR-21-PS 10 wt%	63 ± 10	7.7 ± 1.0	0.16 ± 0.04	10 ± 6	–
PMMA/PR-24-PS 5 wt%	62 ± 5	7.5 ± 1.3	0.16 ± 0.03	10 ± 5	66 ± 20
PMMA/PR-24-PS 10 wt%	63 ± 5	7.6 ± 0.9	0.15 ± 0.01	9 ± 4	–

2.2.3. Poly(lactic acid) Nanocomposite Films

Poly(lactic acid) or polylactide (PLA) is a biodegradable polymeric material that is generated from renewable products, rather than conventional petroleum products, as is the case for ordinary polymeric materials. PLA has become an attractive replacement for materials such as poly(ethylene terephthalate), due to its competitive mechanical properties and amenable manufacturing properties. Currently, PLA is aggressively being researched as a viable renewable resource for the food and agricultural industries [60-61]. PLA is currently used in a number of biomedical applications, such as sutures, stints, dialysis media, and drug delivery devices, but it has also been evaluated as a material for tissue engineering. In addition, films composed of poly(lactic acid) have been employed

in the medical industry as a means to reduce the formation of postoperative cardiac adhesions [62] and as a means to reduce postoperative intra-abdominal adhesions, inflammation, and fibrosis [63]. In these biomedical applications, the PLA system is selected because of its specific composition and molecular architecture. The PLA films possessed a prescribed mechanical strength, flexibility, rate of resorption, and biocompatibility that was needed for these biomedical applications. Thus it can be avowed that PLA is a multi-purposed material that can be utilized due to its superior mechanical strength and biodegradability attributes.

Combining PLA with nanoclay particles for increased barrier and mechanical performance has also become popular [64-66]. Because of the increased interest in PLA as a viable engineering and packaging material, there should be more studies directed at the mechanical and fatigue behavior of the materials. This study seeks to mitigate this research gap by identifying the modes and mechanisms of failure for PLA and PLA 5 wt% samples with nanoclay loaded under uniaxial tension and uniaxial fatigue loading.

2.3. Artificial Neural Networks (ANNs) – Applications in Mechanics and Engineering

2.3.1. *Overview of ANNs*

An artificial neural network is an information processing system that has certain performance characteristics in common with biological neural networks [67]. A neural network is characterized by:

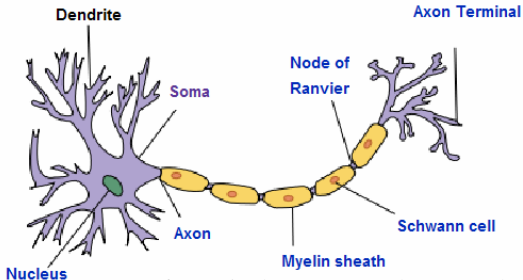
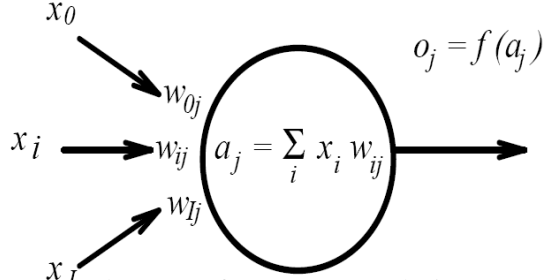
- 1) its pattern of connections between the neurons (called its architecture)
- 2) its method of determining the weights on the connections (called its training, or learning algorithm)

3) its activation function

Artificial neural networks have been successfully utilized in engineering, science, medical, and finance applications. In the past, applications utilizing neural networks have included signal processing, control systems, pattern recognition, medicine, speech production, speech recognition, and mortgage banking [67]. There is a strong similarity between the structure of the biological neuron (i.e. a brain or nerve cell) and the processing element (artificial neuron) of a neural network. The dendrites, soma, and axons of a typical brain nerve cell are reminiscent of the functions of the neural network, as explained in Table 2.3.

Abdi [68] has provided a detailed and thorough explanation of neural networks, where a historical perspective of neural networks is provided, types of neural networks are expounded upon, and examples of modeling applications are given. Figure 2.11 displays a perceptron architecture that is composed of two layers along with modifiable synaptic weights. Despite the recent approbation, ANNs were originally based on antediluvian concepts posed by McCulloch and Pitts in 1943 [69] and Rosenblatt's introduction of the perceptron in 1958 [70]. Later examinations [71-72] proved that these prehistoric models were highly ineffectual in nature and were basically glorified linear regression models with limited capabilities, where associations between inputs and outputs existed only if the output was a linear transformation of the input [68].

Table 2.3. Table describing functions of the dendrites, soma, and axon in a biological neuron

<i>Dendrites</i>	<i>Soma</i>	<i>axon</i>
Receive electric signals from other neurons (across a synaptic gap). The action of the chemical transmitter modifies the incoming signal by scaling the frequency of the signals that are received in a manner similar to weights in an ANN	Cell body – Contains the cell nucleus. The actions are similar to the ANN in which it sums the incoming signals	When sufficient input is received, the cell fires; that is, it transmits a signal over its axon to other cells. It is often supposed that a cell either fires or doesn't fire, so that the transmitted signal can be treated as binary.
 <p>Structure of a typical neuron: each neuron has three basic parts: cell body (soma), one or more dendrites, and a single axon. [73]</p>		 <p>Input and outputs of a perceptron. The inputs are noted as x_i, the synaptic weights are w_{ij}, the total activation is a_j (its response is o_j) [68]</p>

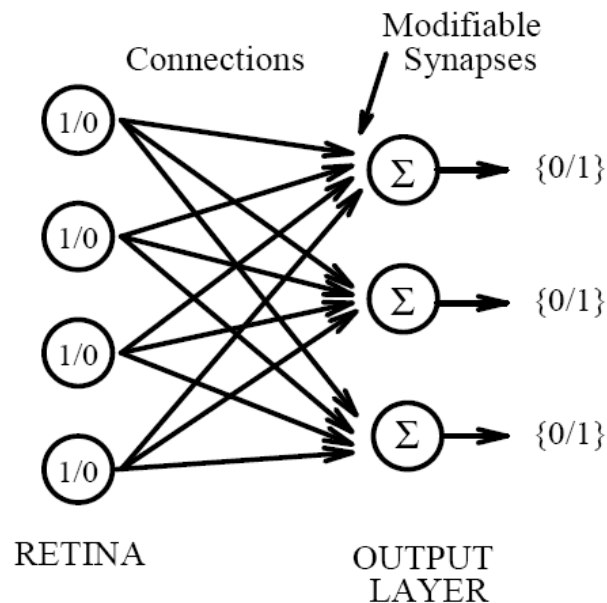


Figure 2.11. Perceptron architecture composed of two layers of cells connected by synaptic weights [68]

2.3.2. *Applications of Neural Networks: Classification and Regression*

Advancements in computational power and development of more rigorous nonlinear models have engendered a new level of success for the employment of neural networks for a plethora of engineering applications. Currently, artificial neural networks can be employed for pattern recognition or regression analysis, depending upon the nature of the problem to be solved.

In applications involving pattern recognition, the goal of the neural network algorithm is to correctly classify species based upon certain input variables that are inherently associated with the type of species. Examples of applications involving classification neural networks include: prediction of secondary structure of a protein from its amino acid sequence [74], sedimentary rock classification [75], and stock market predictions [76]. In general, statistical classification is a procedure in which individual items are placed into groups based on quantitative information of one or more characteristics inherent in the items (referred to as traits, variables, characters, etc.) and based on a training set of previously labeled items [77]. A general mathematical definition of the classification problem can be described as: Given training data $\{(x_1, y_1), \dots, (x_n, y_n)\}$, produce a classifier $h: X \rightarrow Y$ which maps an object $x \in X$ to its classification label $y \in Y$.

In terms of regression analysis, from a statistical standpoint, the objective is to relate a dependent variable(s) to a specified set of independent variables. A regression formulary can either be linear or nonlinear, depending on the relationship between the input and output variables. The types of neural networks that were employed in the current research made use of nonlinear algorithms for determining the relationship

between the input and output variables. Nonlinear regression neural networks, or nonlinear function approximation neural networks, are employed to estimate a function of the input to the output variables when complexity preponderates over the simplicity of a simple linear regression analysis. To illustrate the gamut of applications utilizing nonlinear regression models outside of composites and mechanics, a few examples of recent applications include:

- Food science and engineering – processing of cassava crackers, where the objective was to predict moisture content and water activity during the hot air drying process [78]
- Biomedical engineering – research on pediatric patients with potential kidney ailments, where the goal was to predict a delayed decrease of serum creatinine (breakdown of creatine phosphate in muscle) [79]
- Aquacultural engineering – research on the effect of shrimp farm environment to predict the growth of shrimp based on a set of variable growth conditions [80]
- Agricultural engineering – assessment model to predict ammonia emission from field applied manure utilizing 11 emission factors [81]

As seen from the descriptions in these examples, the range of applications for nonlinear regression models and neural networks is wide-ranging.

The rudimentary concepts of an artificial neural network (with a hidden layer) are shown in Figure 2.12, where an input and an output layer of variables is given. To correctly associate the output variables, the network training begins and initializes with a default set of weights on the synaptic connections. The algorithm progresses in a forward

manner until the desired output is reached. Weight changes are adjusted through employment of a learning algorithm such as a backpropagation scheme, where the output error (mean squared error (MSE) between desired output and predicted output variables) is reduced over a series of epochs (time intervals) until the desired minimum is achieved. Backpropagation typically refers to the supervised learning technique that is utilized for training artificial neural networks [82]. Employed generally in feedforward network systems, the general meaning of the term refers to a “backwards” propagation of the error terms between the input and the output in an effort to reduce the overall mean-squared error.

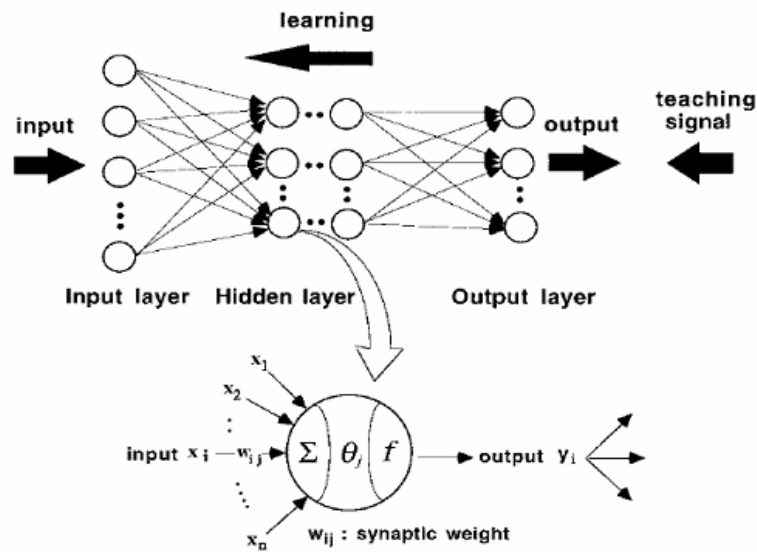


Figure 2.12. Architecture of ANN model [83]

2.3.3. Learning Paradigms in ANNs

In order for a neural network to accurately associate the input variables with the output variable(s), it must first traverse through a series of learning exercises. From a practical standpoint, the process of learning in the network scheme involves being

presented with a set of observations and the network then adjusting itself to solve the algorithm from an optimal standpoint. There are three main types of learning paradigms for ANN architectures. They include:

- Supervised learning
- Unsupervised learning
- Reinforcement learning

The objective of the learning exercises in the neural network scheme is to minimize a cost function, which in typical cases is the mean squared error term (MSE). Most applications in regression analysis and classification analysis utilize supervised learning techniques to minimize the cost function and solve the problem in an optimal manner. In essence, the supervised learning algorithm involves being presented with a sequence of training vectors, or patterns, each with an associated target output vector. The weights are continually adjusted over a series of computation intervals in an effort to reduce the cost function, or MSE. The MSE is calculated based on the following equation [84]:

$$E = \frac{1}{2} \sum_i (t_i - y_i)^2 \quad (2.12)$$

In this equation, t_i represents the target (or desired) response on the i th unit (neuron) and y_i is the actual produced response.

Various algorithms can be used to achieve this learning procedure and minimization of MSE cost. They include:

- Standard backpropagation (gradient descent)
- Backpropagation with momentum
- Conjugate gradient
- Levenberg-Marquardt

- Genetic learning

The most popular of these methods is the backpropagation scheme, which literally refers to a backwards propagation of errors throughout the network. The rudiments of these learning procedures will be briefly discussed in the later sections of this chapter.

2.3.4. Applications of genetic training algorithms in neural networks

The concept of genetic training in neural networks extends that of basic training algorithms such that the training process is optimized through a method similar to evolutionary behavior that occurs in biological systems. The goal of the genetic training algorithm is to find the optimal solution to the problem which results in a minimum error. The genetic training procedure involves selection, crossover, mutation, and evaluation of networks that are tested for fitness. A schematic description of the genetic training process is shown in Figure 2.13 [154].

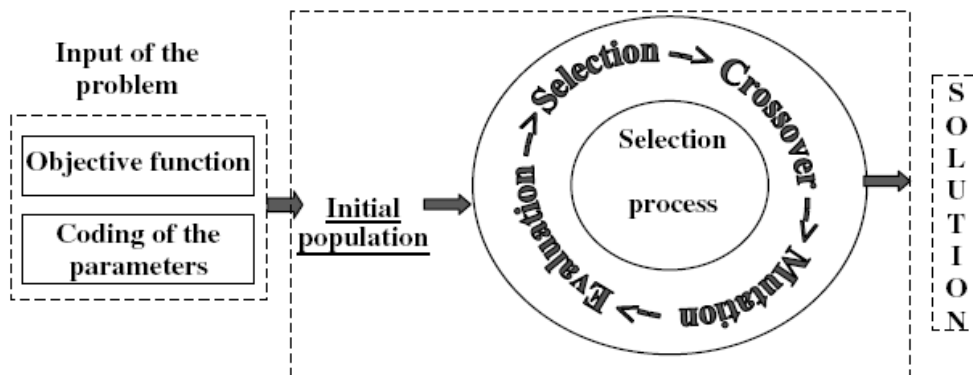


Figure 2.13. Basic procedure used for genetic algorithm training [154]

The authors in [91-95] have investigated the employment of genetic algorithm (GA) neural networks for mechanical behavior predictions in composite materials. Li et

al. [91] have used genetic algorithms for modeling semi-solid extrusion of composite tubes and bars, which involved solidification, heat transmission, and large plastic deformation. The GA was applied in the optimization design of the technical parameters in the semi-solid extrusion processes, where good agreement between the calculated data and the experimental results was achieved. Kemal et al. [92] used GAs to obtain optimal layer sequences in symmetrically laminated square and rectangular plates. The GA and neural networks successfully predicted the natural frequencies of the composite plates and optimal layered sequences, as compared to results from a finite element model. Aijun et al. [93] utilized neural networks and GAs for the analysis and prediction of the correlation between CVI processing parameters and actual properties of carbon-carbon composite materials. The authors in [93] used GAs to optimize the input parameters of the model and select perfect combinations of CVI (chemical vapor infiltration) processing parameters. Suresh et al. [94] used particle swarm optimization and GAs to find the optimal geometry and stacking sequence of rotor blades that satisfied stiffness requirements with elastic couplings. They found that both particle swarm optimization schemes and GAs provided close approximations to the experimental results. Abouhamze and Shakeri [95] used GAs for stacking sequence optimization in laminated composites and obtained good results as compared to the experimental results.

In regards to constitutive behavior prediction of materials, there have been researchers that utilized GAs for the prediction of the mechanical behavior. Early studies by authors in [96-97] were conducted using GAs for the prediction of the constitutive behavior of materials. Recently, Rao et al. [98] have utilized ANNs and GAs for simulation of the stress-strain response of whisker reinforced ceramic-matrix composite

(CMC) materials. The training of the feedforward network was conducted for stress-strain paths of CMCs having various interfacial shear strengths. Successful results were obtained, indicating the capability of the network to replicate the constitutive results from finite element analysis.

Genetic training of an artificial neural network involves optimization of the neural network inputs and network parameters, such as step sizes, momentum values, and number of processing elements in the hidden layer [98, 99]. As stated earlier, the main goal of the optimization scheme is to search for the appropriate parameter settings that yield the lowest minimum error (lowest cost function), as is the case for all learning algorithms.

2.3.5. Types of ANNs applied in engineering applications

The multilayer perceptron model and generalized feedforward model are simple types of ANN architectures that can be utilized to relate a specific set of input variables to a singular or set of multi-targeted output variables. In general, multilayer perceptrons (MLPs) are layered feedforward networks that are trained with static backpropagation algorithms. Their primary advantage rests in the ease-of-use and the capacity to approximate any input/output map. The key disadvantages are that they train slowly, and require lots of training data (typically three times more training samples than network weights) [99]. Similarly, generalized feedforward networks are a generalization of the MLP such that connections can skip one or more layers. In theory, a MLP can solve any complex problem that a generalized feedforward network can solve. However, in practice generalized feedforward networks tend to be much more efficient in computation

time and the training process. In some instances, a standard MLP can necessitate several hundred more training epochs than the generalized feedforward network containing the same number of processing elements.

2.3.6. ANNs Applied to Fatigue Behavior of Composites

Why should researchers and designers apply ANNs to unreinforced polymers and nanocomposites? The answer is quite simple and rests upon the following observations:

- Empirical models that are easy to use
- Neurons can represent and predict nonlinear behaviors
- Computational tools have become easily accessible

Over the past decade, a plethora of ANN applications related to composite materials have been developed by scientists and engineers for various applications. ANNs are useful nonlinear analysis tools for determining complex nonlinear relationships among input and output variables. Researchers have applied ANNs to polymeric matrix composites, metal matrix composites, and ceramic matrix composites to predict mechanical properties based on uniaxial experiments, biaxial experiments, and fatigue [100-105].

In regards to composite materials, Al-Assaf and El Kadi [106] have utilized polynomial classifiers (PCs) and ANNs to predict fatigue lives of unidirectional laminates under tension-tension and tension-compression fatigue loading. The critical input parameters utilized for the ANN were maximum stress, fiber orientation angle, and stress ratio. Multi-layer back-propagation networks and feedforward multi-layer networks were employed to predict the fatigue lives of the composites.

Lucon and Donovan [107] have utilized an ANN technique on metal matrix composites to estimate the macroscopic elastic properties, obviating the need for computationally expensive micromechanics techniques. An eight-celled representative volume element (RVE) was utilized in this research, similar to the micromechanics approach. Inputs into the ANN were achieved by assembling the elastic modulus (E) and Poisson's ratio (ν) values for the RVE into a vector form. The output targets represented the macroscopic effective Young's moduli and effective shear moduli of the system. A MAC3D micromechanics code, based on the generalized method of cells, was used to successfully train the network. The results from the research showed that computation time was significantly reduced as compared to traditional micromechanics approaches (Figure 2.14).

In regards to residual strength of composite materials, Leone et al [83] have investigated the use of ANNs for predicting residual strengths in glass fiber reinforced plastics (GFRPs) for pre-fatigued samples. In this study, the input variables were selected as the stress level, σ , and the number of acoustic emission events, N_t . The solitary output variable was computed as the non-dimensional stress, σ/σ_c , which relates the applied stress to the composite residual strength. Excellent agreement was obtained with the employment of the ANN scheme, and the results are shown in Figures 2.15 and 2.16.

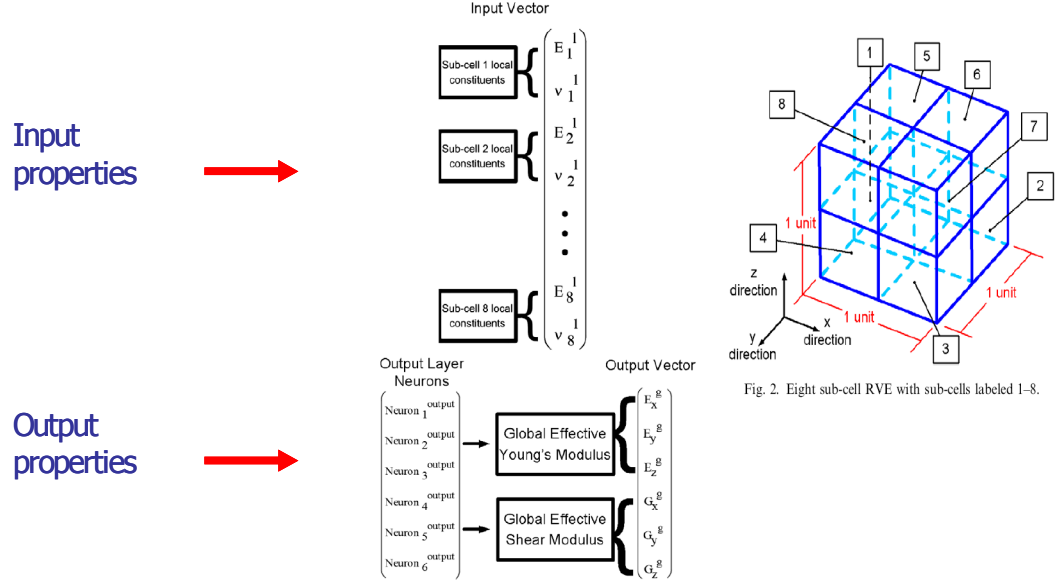


Fig. 3. Input vector and output neurons associated with the target or output vector.

Figure 2.14. Schematic representing how ANNs are used to estimate global (effective) properties in a metallic composite [107]

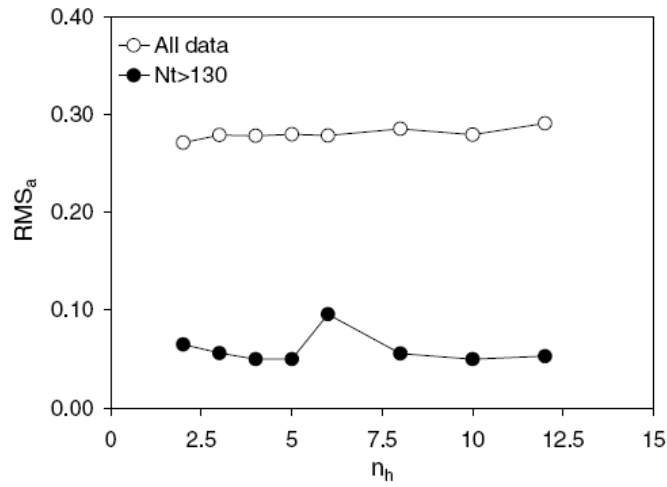


Figure 2.15. Dependence of the asymptotic root-mean-square error, RMS_a , on the number of nodes of the hidden layer, n_h [83]

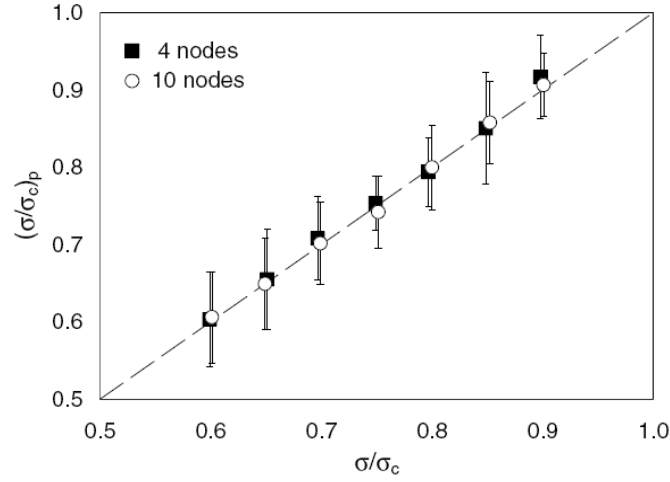


Figure 2.16. Predicted non-dimensional applied stress, $(\sigma/\sigma_c)_p$, against actual non-dimensional applied stress, σ/σ_c , for the two ANN architectures examined [83]

Figure 2.15 illustrates the fact that lower RMS error was achieved when N_t was greater than 130, indicating that a strong correlation existed between the composite residual strength and number of acoustic emission events. Combined with results from Figure 2.16 and elementary fracture concepts [12], these results suggest that critical defects were present in the material at a certain stress level, thus lowering the overall strength of the material due to fatigue. Thus in this research, the critical damage variable was quantified as the number of AE events related to material degradation, which is specifically related to the defects present for a specific load.

2.4. Material Degradation due to Fatigue

2.4.1. Definition of Damage

In order to quantify the actual accumulation of damage in a material due to fatigue loading, one must characterize and quantify the damage. Damage can be defined as the gradual degradation of a material and is an intrinsic material property dictated as a

damage variable [108]. There have been a multitude of authors that consider damage as an intrinsic material state [109-117]. In terms of fatigue, damage can be considered an abstruse concept in relation to conventional approaches such as S-N and Coffin-Manson curves. In fact, damage is not defined in these models since they provide a number of cycles to failure or fatigue life prediction, which does not truly reflect the progressive process of fatigue damage evolution due to growth and coalescence of microcracks. Traditional fatigue theories do not reflect an inherent intrinsic approach, and cannot give the damage distribution of the material under cyclic loading [108].

In conventional materials, damage is characterized in terms of dislocation density or microcrack density used in boundary value continuum mechanics problems due to the fact that elasticity is directly correlated with damage. This elasticity to damage correlation is confirmed because the number of atomic bonds decreases with damage [118]. In our current state of engineering, it is too difficult to develop a prognostic model based solely on dislocation or crack density considerations [108,119]. Thus one has to measure degradation of the global mechanical properties, such as elastic modulus to represent the evolution of dislocation density or microcrack density. Inelastic strain is also considered to be related to fatigue damage evolution [108].

2.4.2. Elastic Modulus Degradation

In engineering, the elastic modulus is measured on samples as a function of strain up to 1% strain [13]. Changes in elastic modulus due to thermal and/or mechanical cycling can illuminate the accumulation of damage in a material, as described in Basaran et al. [108]. Using elastic modulus degradation as a damage metric is highly established

in the mechanics community [119-120]. The elastic modulus degradation metric can be quantified as:

$$D = 1 - \frac{E_i}{E_0} \quad (2.28)$$

In this equation, D is the damage state variable, E_0 is the initial elastic modulus, and E_i is the elastic modulus at any point. At the initiation of the test $D=0$ and for ultimate failure $D=1$.

2.4.3. *Inelastic strain*

Inelastic strain can be considered as any component of strain that is not recoverable as a result of the fatigue loading process. In effect, inelastic strains are considered to occur due to irreversible processes from the standpoint of thermodynamics. This has been established from the Clausius-Duhem inequality of thermodynamics, in which processes such as creep and plastic strains engender irreversible changes in the material. Inelastic strains can occur as a result of the creep process due to constant amplitude fatigue loading or as a result of plastic strains that are engendered due to loading above the yield point of the material. There have been several researchers that consider inelastic strains as a damage evolution criterion [108, 119-120].

CHAPTER 3

MECHANICAL AND FATIGUE BEHAVIOR OF POLY(LACTIC ACID) NANOCOMPOSITE FILMS

Summary of Chapter 3

The mechanical and fatigue behavior of poly(lactic acid) (PLA) neat films and PLA films reinforced with 5 wt% nanoclay particles has been examined using various analytical procedures. The results showed that for the films tested in this study, PLA 5 wt% samples were more susceptible to crazing at the same maximum fatigue stress as the PLA neat samples, as evidenced by results from light transmission experiments in the visible spectrum. In addition, under fatigue loading conditions, the PLA neat samples displayed almost the same fatigue resistance (number of cycles to failure) at 3 Hz and 30 Hz, while the PLA 5 wt% samples showed a shift in the number of cycles to failure to higher values at a frequency of 30 Hz. Using the linear regression curves from the *S-N* data (stress vs. number of cycles to failure), time to failure curves were generated to show the difference between the PLA neat and PLA 5 wt% samples when tested at frequencies of 3 Hz and 30 Hz. Based on these results, it is known that the nanoclay particles served to increase the fatigue resistance at the higher frequency of 30 Hz, when compared to the PLA neat sample.

3.1. Experimental

3.1.1. Sample Preparation and Mechanical Testing

The PLA neat and PLA 5 wt% specimens were prepared and processed at the University of Akron, Akron, OH, USA. The sample specimen size used for the fatigue

tests was 9.5 mm wide by 30 mm long. The thickness of the PLA neat samples and PLA 5 wt% samples was 0.26 ± 0.02 mm and 0.30 ± 0.04 mm, respectively. The BOSE® ELeCtroForce® (ELF®) 3200 testing machine (Enduratec)) was used to conduct the mechanical experiments in uniaxial fatigue at frequencies of 3 Hz and 30 Hz. The Enduratec has a maximum load of 225 N (50 lbf) and a maximum frequency of 400 Hz. A set of low mass grips, Model GRP-TC-DMA450N from BOSE ELeCtroForce® (Eden Prairie, MN USA), were used to conduct the fatigue tests. The ELF 3200 measures displacements via a Capacitec 100 μ m displacement transducer (Model HPC-40/4101) used as a feedback for the control loop. The uniaxial tensile tests for characterization were performed at an elongation rate of 5 mm/min on a standard Instron machine. The Q800 Dynamic Mechanical Analysis (DMA) machine from TA instruments (New Castle, DE USA) was used to evaluate and characterize the dynamic behavior of the samples as a function of frequency and temperature. The specimen size used for the DMA tests was 10 mm wide by 25 mm long. All experiments were conducted at room temperature, laboratory air. The typical humidity of the laboratory air was about 50%.

3.1.2. Light Transmission Experiments

Light transmission experiments were conducted in the visible wavelength spectrum (360-750 nm) on the UltraScan XE spectrophotometer from HunterLab (Reston, VA) to assess the effects of crazing. Due to the small specimen width, an aperture size of 0.375" was attached to the instrument to conduct the light transmission experiments. Light transmission experiments were conducted to determine the effects of mechanical loading on the opacity (reduction in transparency) of the PLA and PLA 5

wt% nanocomposite samples. The samples were loaded into the machine as close to the fracture surface as possible, so as to capture the effects of stress whitening due to crazing that developed around and close to the failure region.

The equation that appositely describes the amount of light that was transmitted through the sample can be determined by considering the Beer-Lambert Law [121-122], considering that the fractional light intensity that was lost can be represented as:

$$\frac{dI}{I} = -a_T dh \quad (3.1)$$

Here, dI represents the fractional loss in intensity, I is the intensity of light, a_T is the extinction coefficient, and dh represents the infinitesimal thickness of the sample. If this equation is integrated, one obtains the following:

$$\int_0^h \frac{dI}{I} = -a_T \int_0^h dh \quad (3.2)$$

The intensity as a function of the extinction coefficient and thickness of the sample is expressed as the Beer-Lambert Law [121]:

$$I = I_0 e^{-a_T h} \quad (3.3)$$

The transmission of light through the sample can be expressed as:

$$T = \frac{I}{I_0} \approx \frac{P}{P_0} \quad (3.4)$$

Here, I and I_0 represent the transmitted intensity and the incident intensity, respectively, and P and P_0 represent the transmitted power and incident power, respectively. In these experiments, the sample thickness of the PLA neat samples was 0.26 ± 0.02 mm and the thickness of the PLA 5 wt% samples was 0.30 ± 0.04 mm.

3.2. Uniaxial Tensile Test Results

The results from the uniaxial tensile tests indicate that the PLA neat films and the PLA 5 wt% films exhibited similar mechanical properties. The modulus of the neat film (3.1 GPa) was very close to that of the PLA 5 wt% nanocomposite film (3.2 GPa). On average, the maximum strain of the neat film sample was very close to that of the nanocomposite sample (0.081 compared to 0.10). The tensile energy of the PLA 5 wt% sample was approximately 5% more than the PLA neat sample. Lastly, the maximum stress of the PLA neat sample was actually 18% higher than the 5wt% sample. These results are not in accordance with similar studies that have evaluated the mechanical behavior of PLA with the inclusion of clay nanoparticles. The authors in [65] noted an increase in the tensile strength of the PLA nanocomposites up to 5 wt%, whereas in the current study a decrease in the tensile strength was observed.

Table 3.1. Uniaxial tensile test results for poly(lactic acid) PLA neat films

	Thickness	E	σ_{\max}	σ_f	ϵ_{\max}	Energy
	mm	GPa	MPa	MPa		kJ/m^3
PLA2002D-NT-1	0.27	3.1	57	51	0.052	2.0
PLA2002D-NT-2	0.27	2.8	58	50	0.053	2.3
PLA2002D-NT-3	0.23	3.2	59	49	0.12	5.5
PLA2002D-NT-4	0.26	3.1	60	49	0.12	5.6
PLA2002D-NT-5	0.22	3.4	58	52	0.055	2.5
PLA2002D-NT-6	0.28	3.1	59	50	0.092	4.3
Average	0.26	3.1	58	50	0.081	3.7
Std. Dev.	0.02	0.21	1.0	1.2	0.032	1.6
95% Confidence		0.22	1.1	1.3	0.033	1.7

Table 3.2. Uniaxial tensile test results for PLA films with 5 wt% nanoclay particles

	Thickness	E	σ_{\max}	σ_f	ϵ_{\max}	Energy
	mm	GPa	MPa	MPa		kJ/m ³
PLA2002D5%C30B-1	0.29	2.9	45	38	0.11	4.0
PLA2002D5%C30B-2	0.28	3.1	49	41	0.14	5.5
PLA2002D5%C30B-3	0.27	3.3	50	42	0.080	3.2
PLA2002D5%C30B-4	0.38	3.4	54	46	0.10	4.3
PLA2002D5%C30B-5	0.28	3.2	49	41	0.087	2.7
Average	0.30	3.2	49	41	0.10	3.9
Std. Dev.	0.040	0.20	2.7	2.5	0.020	0.94

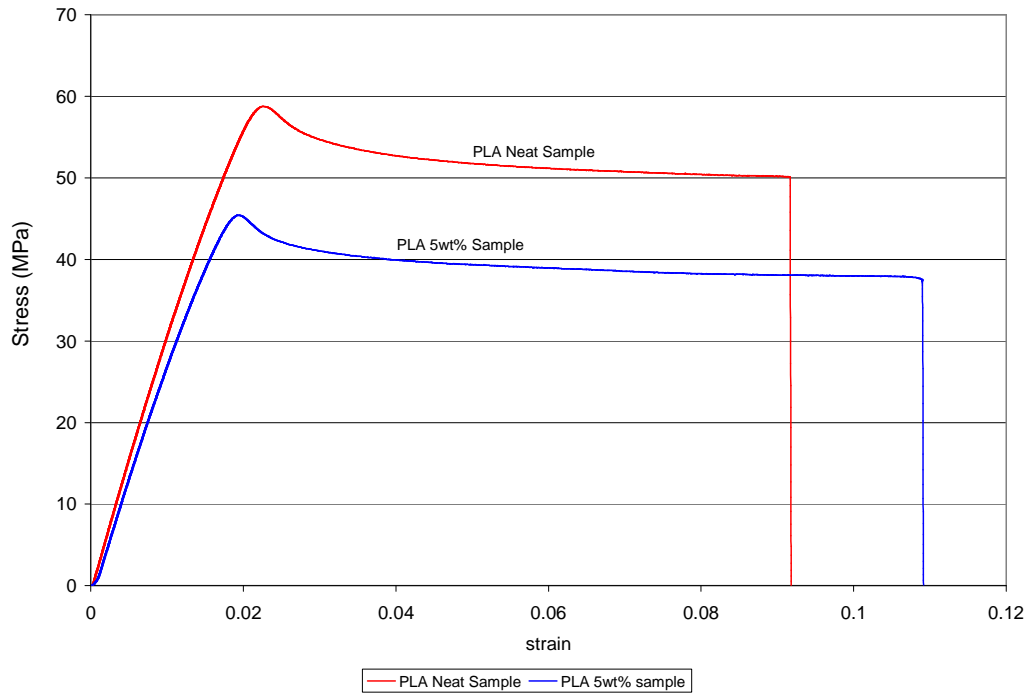


Figure 3.1. Example stress-strain curves of PLA neat and PLA 5 wt% samples under uniaxial tensile loading conditions

These results are somewhat counterintuitive, since one would envision that the addition of rigid platelet clay nanoparticles would have significantly enhanced all of the mechanical properties of the PLA samples. However, the intimacy of the bonding between the matrix and nanoparticle was low, since the addition of functional groups or other bonding agents was not incorporated into the fabrication process. This led to a

lower interfacial strength of the nanocomposite specimens. Due to the low interfacial adhesion between the nanoparticles and PLA matrix, debonding occurred at the site of the interface, leading to lower fracture strengths and higher strains at break under uniaxial conditions. In fact, it has been observed in the literature that systems with low interfacial adhesion between the matrix and polymer exhibit debonding at a stress lower than that of the neat matrix [65,123], leading to lower yield strengths and higher strains at break (due to massive crazing) with increasing nanoparticle concentration. Also, due to the platelet shape of the nanoparticles, stress concentration sites were engendered, causing the debonding to occur more easily. Shown in Figure 3.2, the authors in [124] have illustrated how the yield stress in a polymeric sample decreases with the addition of rigid platelet CaCO_3 nanoparticles. In essence, the researchers in [124] explained that the reduction in yield strength was due to the fact that the particles debonded from the matrix before overall yield. Based on these results, it is believed that under uniaxial conditions, the debonding caused a lower yield and fracture strength of the PLA 5wt% sample, as shown in Figure 3.1.

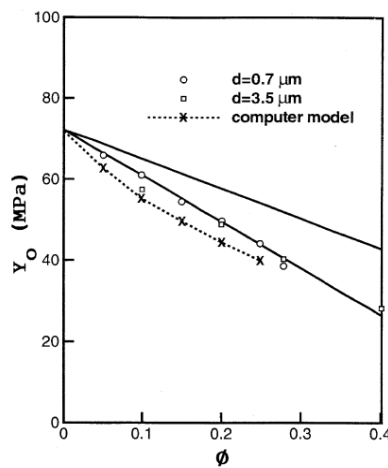


Figure 3.2. Yield stress vs. particle volume fraction for polymer system with rigid CaCO_3 particles displaying the decrease as a function of particle volume fraction [10]

3.3. Results from DMA

The results from the DMA experiments revealed a difference in behavior for the PLA neat and PLA 5 wt% samples. For DMA tests conducted on the mechanical properties as a function of frequency, the results showed that the nanocomposite 5 wt% samples showed a broader transition in tan delta and storage modulus from lower frequencies up to higher frequencies. This is shown in Figure 3.3, where an example result of the tan delta and storage modulus vs. frequency has been plotted for the samples.

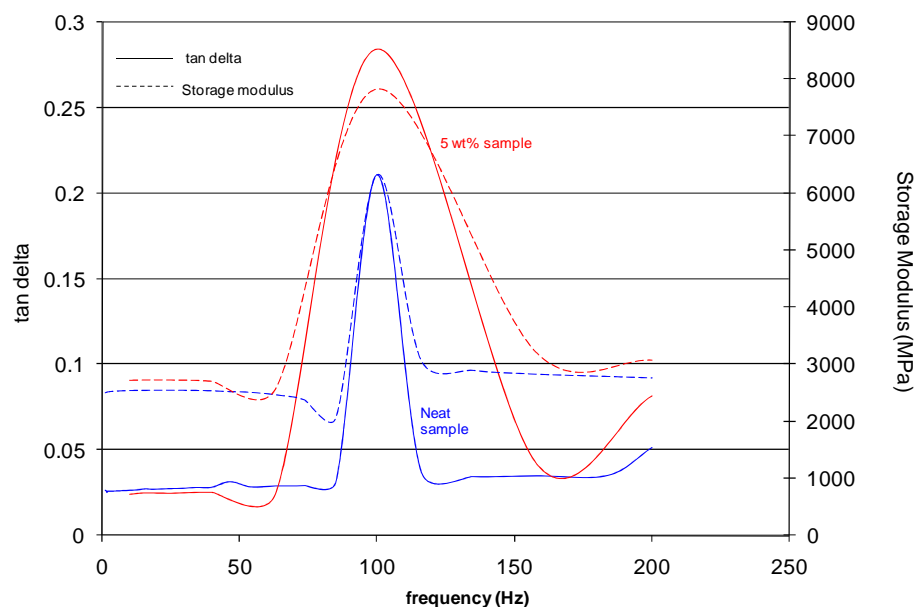


Figure 3.3. tan delta and storage modulus vs. frequency for neat PLA sample and 5wt% PLA sample

It is believed that the broader transition in tan delta for the nanocomposite samples is the result of the nanoparticles that interacted with the matrix and caused the strain in the samples to lag the stress for a larger frequency window than the neat samples. A similar result has been obtained by the authors in [125], where studies of the viscoelastic behavior of polylactide systems reinforced with organoclay nanoparticles has been

obtained. They confirmed results that showed that the $\tan \delta$ function increased as an increasing function of the nanoclay content for all frequencies. In the current study, for both the PLA neat sample and the PLA 5 wt% sample, the critical frequency at which the $\tan \delta$ function displayed its maximum peak was approximately 100 Hz (Figure 3.5). The results from the storage modulus vs. temperature showed a similar result (Figure 3.4), where the mechanical behavior of the films from room temperature up to 120°C was virtually identical. The results showed that for PLA 5 wt% samples, the glass transition temperature was slightly shifted to a lower temperature. The T_g of the neat PLA samples was 77.1°C while the T_g of the PLA 5 wt% samples was 74.7°C.

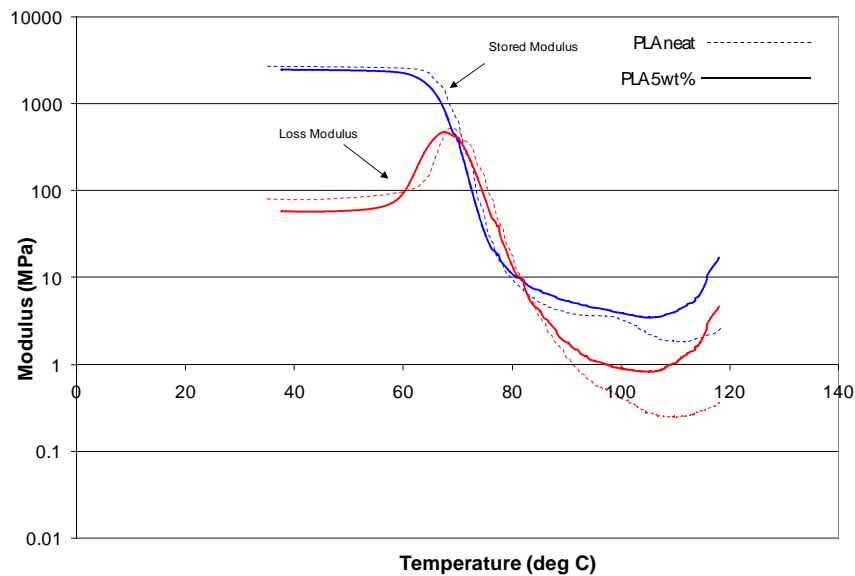


Figure 3.4. Stored and loss modulus vs. temperature for PLA neat and PLA 5wt% samples

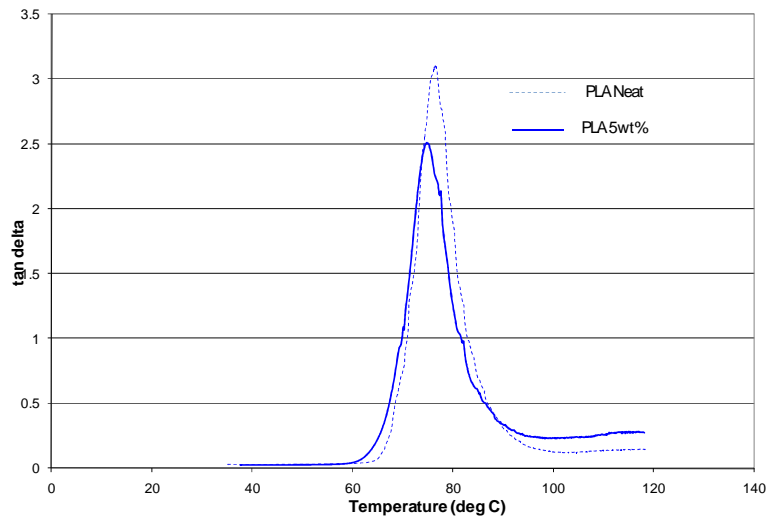


Figure 3.5. Tan delta vs. temperature for PLA neat and PLA 5wt% samples

3.4. Results from Light Transmission Experiments

The results from light transmission indicate that samples loaded in uniaxial tension displayed a great deal of transparency reduction due to the formation of a craze zone that surrounded the crack tip region and spread to a larger portion of the film. In these experiments, stress whitening was visually observed and Figure 3.6 depicts an example where light transmission data of a PLA 5 wt% film tested under uniaxial conditions is quantified. The results indicate that the light transmission behavior changed with loading condition and wavelength. At around 420 nm, the maximum difference between the undeformed PLA 5 wt% and the uniaxially loaded sample occurred. For the uniaxially tested samples, craze zones formed perpendicular to the loading direction. Craze zone formation with the creation of a nubilous film surface is highly established in the literature [12,126]. This crazing process is known to create microvoid sites and stress whitening in the vicinity of deformation for PLA samples with and without the reinforcement of clay nanoparticles [65]. From the light transmission experiments, it was

determined that the wavelength at which the largest deviation in light transmission between the undeformed and deformed samples was approximately 420 nm.

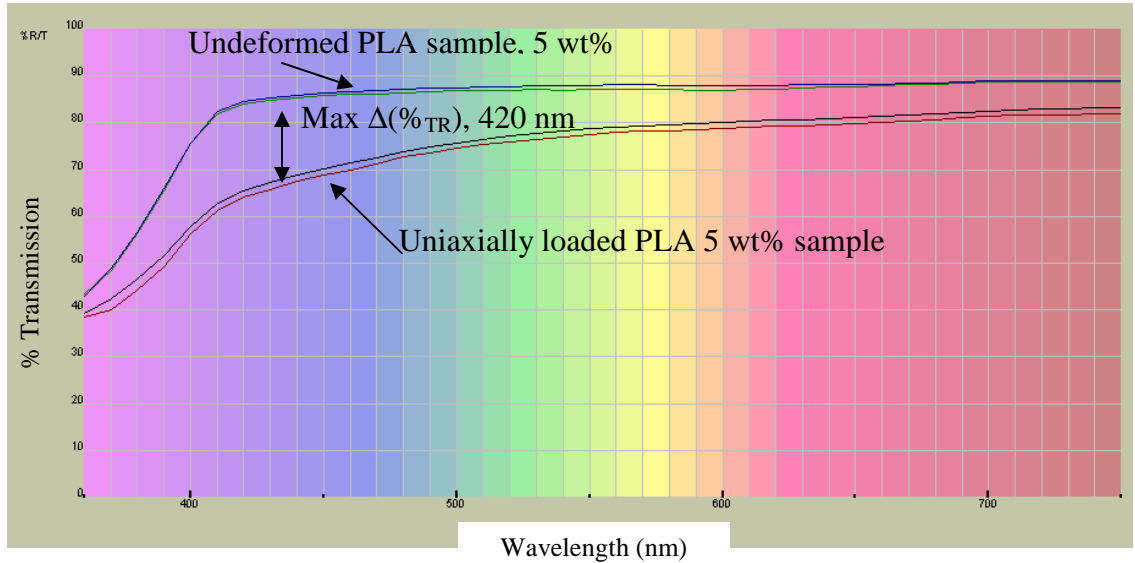


Figure 3.6. Uniaxial tensile test results: light transmission vs. wavelength in the visible spectrum (360 nm-750 nm) for PLA 5 wt% sample tested under uniaxial loading to failure

The light transmission results from the fatigue experiments are shown in Figure 3.7. These results indicated a similar pattern to that of the uniaxially tested samples. There was a critical wavelength around 420 nm that existed for the samples, where the largest deviation was observed between the undeformed sample and deformed samples. It should also be noted that the PLA 5 wt% samples displayed lower light transmission values in the visible spectrum than the PLA neat samples. This is expected, due to the fact that the platelet rigid particles were responsible for inhibiting light transmission through the film at all wavelengths.

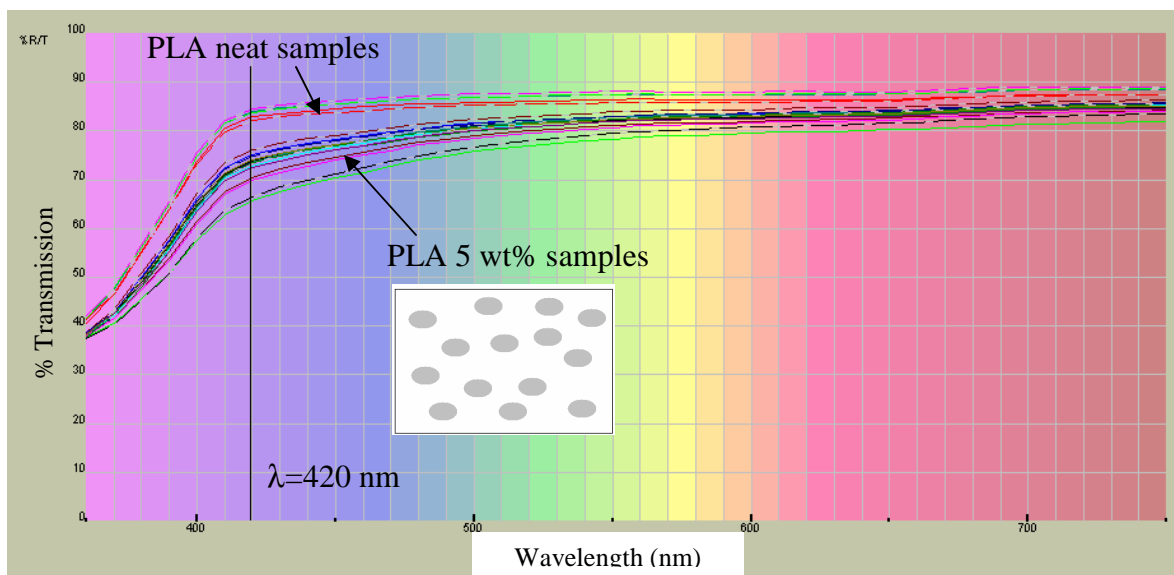


Figure 3.7. Fatigue results: light transmission vs. wavelength for PLA neat and PLA 5 wt% nanocomposite samples

The light transmission behavior of PLA 5 wt% vs. PLA neat samples can be seen more clearly from Figure 3.8, where the light transmission data at 420 nm (critical wavelength) of unfatigued and fatigued PLA neat and PLA 5 wt% samples has been plotted as a function of the maximum fatigue stress. The results showed that for unfatigued PLA, the percentage of light that was transmitted through the sample was approximately 83%, while the PLA 5 wt% unfatigued sample exhibited a light transmission value of 75%. In addition, the PLA 5 wt% samples exhibited a larger decrease in the light transmission as a function of maximum stress with respect to the neat PLA samples. Stress whitening due to crazing was observed visually on both PLA neat and PLA 5 wt% samples. However, based on the light transmission results from Figure 3.8, it is seen that the 5 wt% samples exhibited slightly more opaque film structures as a function of maximum fatigue stress than the PLA neat samples, indicating that the PLA 5 wt% samples were more sensitive to crazing than the PLA neat samples. This can be explained by considering results from the literature that explain that an

increase in the loading of nanoclay particles induces a phenomenon that promotes debonding and localized yielding, leading to significant crazing [65]. Jiang et al. [65] have noted that neat PLA tested under uniaxial tension showed fairly smooth fracture surfaces, when viewed using the scanning electron microscope (SEM). This was due to the lack of large scale plastic deformation in neat PLA. However, the fracture surfaces of PLA reinforced with nanosized-precipitated calcium carbonate (NPCC) showed more yielding features because of larger plastic deformation caused by more crazes. In addition, they observed that the fracture morphology of PLA reinforced with 2.5 wt% montmorillonite (MMT) clay exhibited stress whitening and necking during tension. The results from Figures 3.6-3.8 in this dissertation study are directly in sync with the results from the literature, where more opacity due to stress whitening was observed for the PLA 5 wt% nanoclay films.

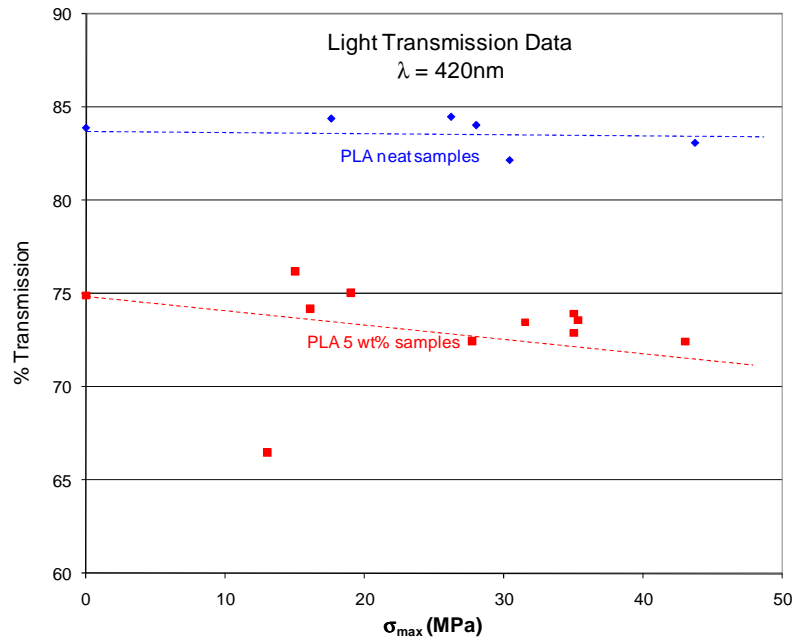


Figure 3.8. Percentage light transmission vs. maximum stress for PLA neat and PLA 5 wt% samples as a function of maximum fatigue stress

3.5. Results from Constant Stress Fatigue

Fatigue tests were conducted on the PLA and PLA 5 wt% samples at various levels of maximum stress to determine the fatigue resistance at frequencies of 3 Hz and 30 Hz. Maximum stress vs. number of cycles to failure (S-N) curves were generated for these samples to determine their resistance to a repeated cyclic loading for a fixed maximum stress. Maximum fatigue stress values in the range of approximately 25% to 75% of the maximum uniaxial stress were used to conduct the fatigue experiments. The results for the experiments conducted below the critical glass transition frequency (below 100Hz) at a frequency of 3 Hz indicated a result that is somewhat concomitant with the results from the uniaxial tensile tests. At 3 Hz, the unreinforced PLA samples exhibited a higher fatigue resistance than the PLA samples reinforced with 5 wt% nanoclay particles, as shown in Figure 3.9. However, at 30 Hz, the PLA neat and PLA 5 wt% samples exhibited almost the same fatigue behavior. This indicates that the nanoclay particles served to enhance the fatigue resistance of the samples at 30 Hz. Based on the regression results shown in Figure 3.9, it is known that both PLA neat and PLA 5 wt% samples displayed a linear semi-log behavior with a functional form that relates the maximum fatigue stress to the number of cycles to failure as:

$$\sigma_{\max} = -m \ln(N_f) + b \quad (3.5)$$

In (3.5), σ_{\max} represents the maximum fatigue stress, m represents the slope of the regression curve, N_f represents the number of cycles to failure, and b represents the y-intercept. Equation (3.5), which relates the maximum stress to the number of cycles to failure, can be rewritten in modified form expressing the maximum stress as a function of time to failure, t_f , and frequency, f , as:

$$\sigma_{\max} = -m \ln(t_f \cdot f) + b \quad (3.6)$$

Equation (3.6) was algebraically modified to derive an empirical relationship for the time to failure that was expected for the PLA neat and PLA 5 wt% samples, as a function of maximum stress and frequency, as:

$$t_f = \frac{e^{-\left(\frac{\sigma_{\max} - b}{m}\right)}}{f} \quad (3.7)$$

For the PLA neat and PLA 5 wt% samples conducted at 3 Hz and 30 Hz, one would expect a similar shift in the number of cycles that yields an equivalent time to failure shift, since 1) the results from DMA indicated that the storage modulus and $\tan \delta$ functions were virtually constant in this frequency range and 2) the uniaxial characterization results indicated that the PLA neat sample is superior to that of the PLA 5 wt% sample in terms of yield strength and fracture strength. However, the PLA neat and PLA 5 wt% nanocomposite samples behaved differently in terms of the time to failure due to fatigue loading as a function of maximum stress and frequency. In an effort to quantify the difference in behavior of the two samples (neat vs. 5 wt%) as a function of frequency, time to failure curves were generated based on the empirical expressions and are shown in Figure 3.10. The time to failure curves for the PLA neat samples at 3 Hz and 30 Hz show a very wide difference in time to failure with respect to the PLA 5 wt% samples. In terms of time, the PLA neat samples at 30 Hz failed much sooner than the PLA neat samples tested at 3 Hz. At 30 Hz, the PLA 5 wt% samples exhibited the same behavior as the PLA neat samples, where they failed sooner than the samples tested at 3 Hz. However, there is one noticeable difference between the fatigue behaviors of the two samples. In terms of time, it must be noted that the PLA 5 wt%

samples exhibited a much smaller time differential between 3 Hz and 30 Hz than the PLA neat samples. After all, based on the mechanical characterization results, one would expect that the fatigue resistance of the PLA 5 wt% samples at 30 Hz would be lower than the PLA neat samples; however, this was not the case. This observation is interesting, because it indicates that the nanoclay particles served to enhance the fatigue resistance of the PLA samples at 30 Hz, where it increased the time necessary to cause failure. In addition, the PLA neat samples fatigued at 30 Hz displayed a steeper decline slope in the semi-log maximum stress vs. number of cycles to failure behavior. Thus, from the results of the uniaxial experiments in Section 3.1 and the fatigue results of this section, it can be concluded that the nanoclay particles engendered two antithetical mechanical property attributes: 1) decreased maximum stress (yield stress) and fracture stress under uniaxial tension conditions and 2) increased time to failure between the lower frequency of 3 Hz and higher frequency of 30 Hz when compared to the PLA neat sample (lower time to failure differential between 5 wt% sample at 3 Hz and 30 Hz).

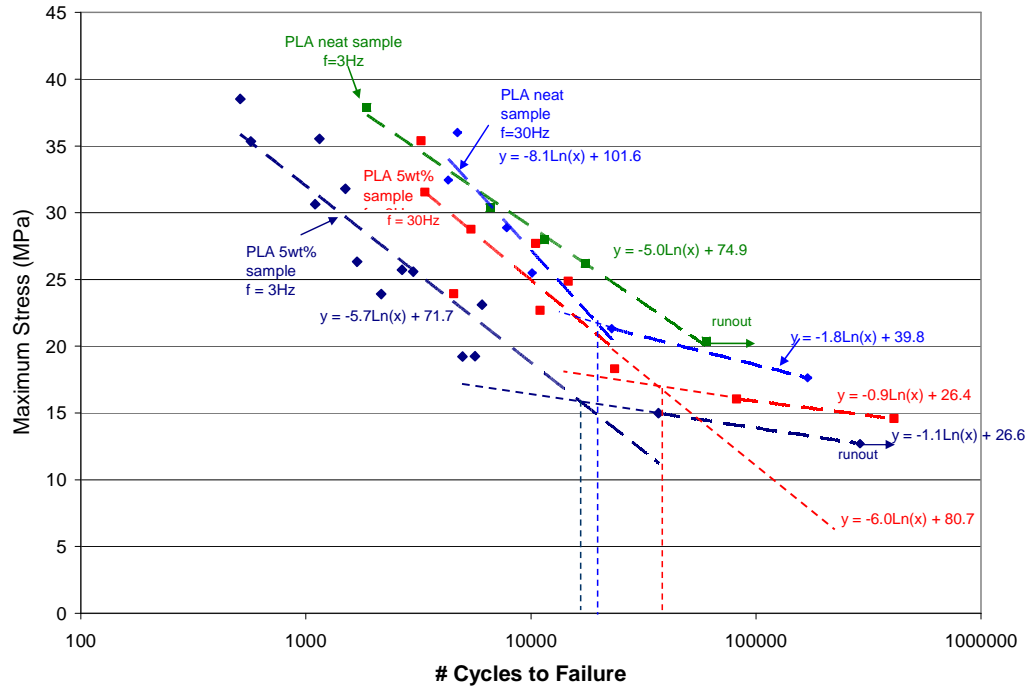


Figure 3.9. Maximum stress vs. number of cycles to failure (S-N curve) for PLA and PLA 5 wt% samples conducted at 3 Hz and 30 Hz

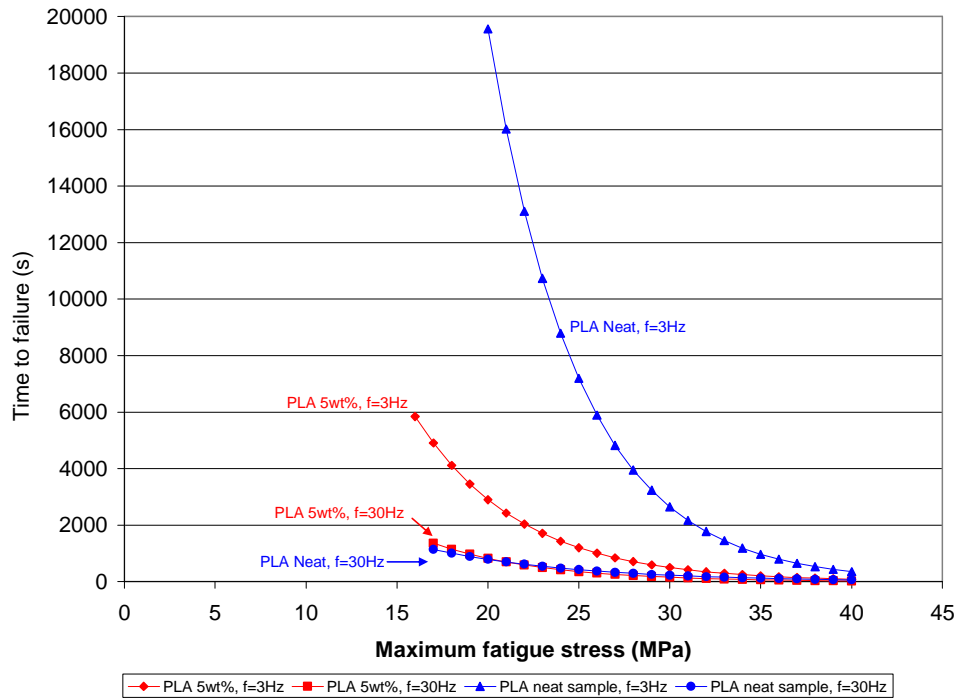


Figure 3.10. Empirical curves of time to failure vs. maximum fatigue stress for PLA neat and PLA 5 wt% samples

3.6. Further Discussion about Results from Fatigue of PLA and PLA Nanocomposite Samples

A study by Kim and Lu in [1] was conducted on polycarbonate samples at different frequencies to determine that cycling at lower frequencies caused a shorter fatigue life (number of cycles to failure) for a given stress amplitude. This same effect has been realized for the current study in PLA 5 wt% samples. Based on results of cycling polycarbonate samples at various frequencies, they noted two observations: Cycling at higher frequencies may cause 1) a change in the internal nature of viscous flow to create localized yield-like deformation and 2) it may cause a thermal effect due to viscoelastic hysteresis-induced heating.

Studies by researchers in [127] have investigated how the role of clay affects the fracture behavior of poly(propylene) (PP) reinforced with nanoclay particles. They conducted wide angle x-ray diffraction (WAXD), transmission electron microscopy (TEM), dynamic mechanical analysis (DMA), and scanning electron microscopy (SEM) in the investigation of the impact properties of PP to conclude that the role of nanoclay served to enhance the mechanical properties of the polymer and to change the deformation mode from matrix crazing and vein-type in neat PP to a microvoid-coalescence-fibrillation process in the PP nanocomposite. This phenomenon is illustrated in Figure 3.11, where the microvoid-coalescence-fibrillation process has been illustrated by the authors in [127].

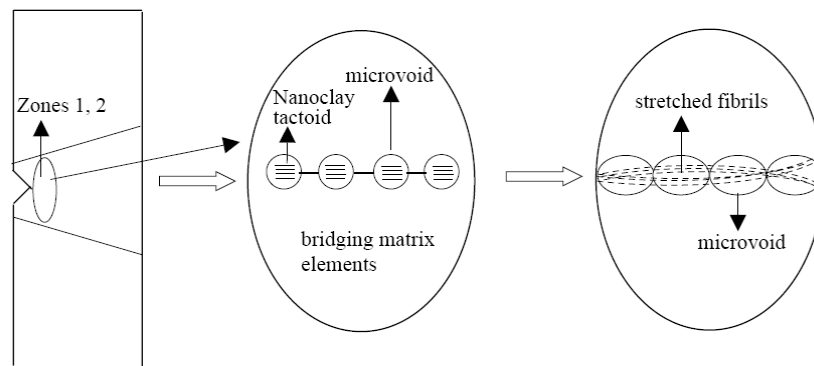


Figure 3.11. Envisioned process of microvoid coalescence-fibrillated fracture behavior in PP nanocomposite (picture from [127])

From the current results, it is seen that as the frequency of the test is increased, the PLA 5 wt% nanocomposite samples were less susceptible to fatigue damage than the PLA neat samples, where at the higher frequency, the nanoparticles served to toughen the material. In fact, it is known from the results in [65] that, although nanoclay particles debond from the surface, they serve to prevent coalescence from forming large cracks and leading to premature failure.

Conclusions from Chapter 3

The mechanical behavior of PLA neat and PLA 5 wt% samples has been evaluated to determine the effect of nanoclay particles on the fatigue resistance. The yield and fracture strength of the PLA neat samples was 18% and 22% higher than the PLA 5 wt% samples, respectively, when tested under uniaxial conditions. Uniaxially tested PLA 5 wt% samples exhibited stress whitening due to crazing and fatigued PLA 5 wt% samples exhibited more stress whitening and crazing than PLA neat samples as a function of maximum fatigue stress, as evidenced by results from light transmission studies. A fatigue study was conducted on the samples at 3 Hz and 30 Hz to ascertain

whether or not there was a difference in fatigue behavior between PLA neat and PLA 5 wt% samples. Based on the literature results and current results from uniaxial tension, it was expected that the fatigue resistance (number of cycles to failure) of the samples would increase with increasing frequency. This increase in fatigue life from 3 Hz to 30 Hz was observed for the PLA 5 wt% samples. However, the PLA neat samples did not exhibit this behavior, where they experienced almost the same number of cycles to failure at 3 Hz and 30 Hz. This phenomenon was further quantified using time to failure curves for the different samples at 3 Hz and 30 Hz, where it was shown that there was a much larger deviation in time to failure for the PLA neat samples than the PLA 5 wt% samples when tested at 3 Hz and 30 Hz cyclic frequencies. Perhaps the results at 3 Hz are concomitant with the results from the PLA neat and PLA 5 wt% uniaxial (quasistatic) experiments, where the lower rate of strain application at that frequency was highly similar to that of uniaxial tension. However, at the higher frequency of 30 Hz, the PLA neat samples may have experienced more damage, since the fatigue life was not increased. Based upon the results from the literature and the results from the PLA neat fatigue experiments, it is known that the nanoclay particles, although not intimately bonded to the PLA polymer chain architecture, served to bolster the fatigue resistance of the samples. The results of this study are important because they indicate that the mechanical behavior of PLA neat and PLA nanoclay samples tested under fatigue loading conditions is different for different frequencies. These results can be used as a quantitative and qualitative measure for studies such as accelerated life testing and mechanical performance. It would be interesting to ascertain how these results compare to a study in which the temperature of the samples is decreased (similar to increase in

frequency for this study), and fatigue experiments conducted to determine if the time-temperature superposition phenomenon is applicable to these polymer systems.

CHAPTER 4

MECHANICAL AND FATIGUE BEHAVIOR OF POLY(ETHYLENE TEREPHTHALATE) (PET) AND NANOCOMPOSITE FIBERS: EXPERIMENTAL RESULTS

Summary of Chapter 4

PET control fibers (diameter of $\sim 24 \pm 3 \mu\text{m}$) and polyethylene terephthalate (PET) fibers with embedded heat treated vapor grown carbon nanofibers (VGCNFs) (diameter of $\sim 25 \pm 2 \mu\text{m}$) were exposed to cyclic loading and monotonic tensile tests. The control fibers were processed through a typical melt-blending technique and the PET/VGCNF samples were processed with approximately 5 wt% carbon nanofibers present in the sample. Under uniaxial fatigue conditions, the fibers were subjected to a maximum stress that was approximately 60% of the fracture stress of the sample at an elongation rate of 10 mm/min in uniaxial tension. Subsequent to non-fracture fatigue conditions, the fibers were tested under uniaxial stress conditions for observation of the change in mechanical properties. The elastic modulus, hardening modulus, fracture strength, tensile energy, and yield strain of both PET control and PET/VGCNF samples in uniaxial tension subsequent to fatigue were shown to be dependent on the residual fatigue strains. Relative mechanical property values were used to analyze the difference in PET and PET/VGCNF samples as a function of residual strain. In most cases, the results indicated a strengthening mechanism (strain hardening effect) in the low residual strain limit for fatigued PET samples and not for fatigued PET/VGCNF samples. In comparison with the unreinforced PET sample, the PET/VGCNF fibers showed greater mechanical property degradation as a function of residual strain due to fatigue when cycled at 60% of

the fracture stress, as evidenced through analytical and SEM (scanning electron microscopy) results. The effects of the fatigue process on these mechanical properties have been hypothesized and supported through existing qualitative, quantitative, and SEM techniques.

4.1. Introduction

Poly(ethylene terephthalate) (PET) fibers have been employed as reinforcement agents in many engineering applications. They are especially known for their toughness and high strength-to-weight ratio. As engineers seek to develop stronger materials for advanced applications, the inclusion of reinforcing agents presents itself as a viable option for increased strength. The field of nanocomposites is particularly attractive for engineers and designers in the field nanotechnology and mechanics of materials. Nano-sized reinforcing agents such as single-walled carbon nanotubes (SWNTs), double-walled nanotubes (DWNTs), multi-walled nanotubes (MWNTs), and vapor-grown carbon nanofibers (VGCNFs) are all candidates for increasing the mechanical properties of various polymer matrices. In this investigation, the inclusion of VGCNFs into the PET fiber was employed to determine the effect of fatigue on the residual mechanical properties of the fibers in uniaxial tension. In essence, the mechanical properties of nanocomposite fibers were investigated from a residual standpoint: how the fatigue process engendered microstructural changes in the fibers and altered their mechanical properties. Limited research exists on the deformation mechanisms of fatigue in nanocomposite PET fibers. In fact, a quantitative study on this subject is needed to fully realize the benefits of reinforcing agents such as VGCNFs, which are in a class of

materials that are touted as the next-generation for lightweight applications. In a recent investigation, Ma et al. [128] utilized various compounding methods (ball milling, high shear mixing, and extrusion) and a traditional fiber spinning method to develop PET/VGCNF composite fibers. In the case of the nanocomposite fibers (PR-24-HT) tested under uniaxial tensile loading at a fixed strain rate, the elastic modulus was shown to be slightly higher than the PET control samples, and the fracture strength was slightly lower than the PET control sample. In the current investigation, the same fibers were tested in an effort to determine their mechanical resistance to cyclic loading under various loading conditions.

4.2. Sample Preparation

The PET/VGCNF specimens were prepared and processed at the Georgia Institute of Technology. The experimental procedure employed in the production of these nanocomposite fibers (PR-24-HT) as well as basic mechanical properties are given in [128]. Single PET/VGCNF filaments were cut to a length that yielded samples with a gage length of 1" (25.4 mm). The single fibers were bonded to a manila (paper) rectangular gasket (0.1 mm thickness) manufactured by the Miami Valley Gasket Co. (Dayton, OH, USA) via Scotch® Super Strength All Purpose adhesive (drying adhesive). The adhesive was allowed to cure for 24 hours for complete bonding. The diameter of the PET control filaments was $24 \pm 3 \mu\text{m}$ and the diameter of the PET/VGCNF filaments was $25 \pm 2 \mu\text{m}$. This was obtained using a standard laser diffraction instrument and test method as described in [128].

4.3. Fatigue & Uniaxial Tensile Tests

The BOSE® ELeCtroForce® (ELF®) 3200 tensile and fatigue testing machine (Enduratec)) was used to conduct the mechanical experiments in uniaxial cyclic loading and uniaxial tension. The load cell had a maximum load rating of 2.5 N (250 g) and resolution of ± 10 mg. The ELF 3200 measures displacements via a Capacitec 100 μm displacement transducer (Model HPC-40/4101) used as a feedback for the control loop. The resolution of this displacement transducer was ± 50 μm full-scale. All experiments were conducted at room temperature, laboratory air. The typical humidity of the laboratory air was approximately 50%.

Based on the terminology and depiction in Figure 2.1, the residual creep strain was measured by subtracting the oscilloscope displacement value at the initiation of the test from the displacement at the conclusion of the constant-stress amplitude fatigue phase, once the specimen was unloaded to zero stress and allowed to dwell for a short time.

Approximately 150 fibers were tested in this investigation. About 10% of the fibers broke at the grip interface at the conclusion of the uniaxial tensile loading phase, which indicated premature failure due to a stress concentration near the grip interface. For this reason, these experimental results were omitted from the results in this study. All fibers possessed the same frequency during cyclic loading (5 Hz), elongation rate during uniaxial tension (10 mm/min), and heat treated (HT) conditions during synthesis [128] of the nanocomposite fibers. A detailed description of the preparation of the samples for mechanical testing is provided in [129].

The dynamic stress-strain response of a viscoelastic polymer sample under fatigue conditions is given in Equation (2.1). One caveat that must be noted is that Equation (2.1) is only valid under equilibrium conditions, once the stress and strain have both attained fixed amplitude values for the duration of the fatigue test. At the initiation of the fatigue test, Equation (2.1) was not valid because the sinusoidal strain response of the material was changing nonlinearly with time (creeping), due to the application of an imposed constant stress. This phenomenon is very similar to the creep behavior in polymers exposed to a constant stress for a long period of time (Figure 2.1).

4.4. Uniaxial Tensile Tests (Specimens Without Prior Fatigue)

Results from the uniaxial characterization tests indicate that the PET-VGCNF samples with 5 wt% were more superior mechanically than the PET control samples. Shown in Table 4.1 are results from the uniaxial tensile tests. A 95% confidence interval was provided to determine the range of values within which the mean value was likely to fall within. Although the samples are identical to the samples tested in [128], the elongation rate in the current study was approximately 40% of the elongation rate in [128]. This validates the minor differences in the mechanical properties for the two studies in the case of the unfatigued samples.

Two methods were used to obtain the modulus of the samples: the 1% strain method according to [13] and the conventional secant modulus method for polymers. The response of the PET and PET/VGCNF fibers without prior fatigue was nonlinear elastic, strain hardening (see Figure 4.1). Subsequent to the yield point, the fiber began to strain harden nonlinearly, and finally reached the ultimate tensile strength or the

maximum stress within the stroke limitations of the machine. As shown in Table 4.1, the PET nanocomposite sample (PET/VGCNF) exhibited higher mechanical properties than the PET control sample in terms of elastic modulus (E), hardening modulus (H), yield strength (σ_y), and tensile energy. The unfatigued yield strains of the PET/VGCNF and PET control samples were similar. In terms of maximum strain within the stroke limitations of the machine (~ 12 mm), the PET control sample exhibited a maximum strain (ϵ_m) equivalent to 0.45 ± 0.017 . This is expected due to the more ductile nature of the PET samples vs. the PET/VGCNF samples.

Table 4.1. Properties of PET control and PET/VGCNF filaments at elongation rate of 10mm/min under uniaxial stress conditions without prior fatigue

PET Control	E (GPa) 1% strain	E (GPa) Secant	H (MPa)	σ_0 (MPa)	ϵ_0	σ_f (MPa)	ϵ_f	Energy (μJ)
Average	6.6	4.2	210	110	0.027	250	0.45	1.1E+03
Std. Dev.	1.1	1.1	46	22	0.0059	33	0.019	1.5E+02
95% Interval	1.1	1.0	43	21	0.0055	31	0.017	1.4E+02
PET-VGCNF	E (GPa) 1% strain	E (GPa) Secant	H (MPa)	σ_0 (MPa)	ϵ_0	σ_f (MPa)	ϵ_f	Energy (μJ)
Average	15.8	11.1	380	300	0.028	526	0.28	1.5E+03
Std. Dev.	0.38	0.47	36	15	0.0030	23	0.050	3.5E+02
95% Interval	0.47	0.58	44	19	0.0037	29	0.062	4.4E+02

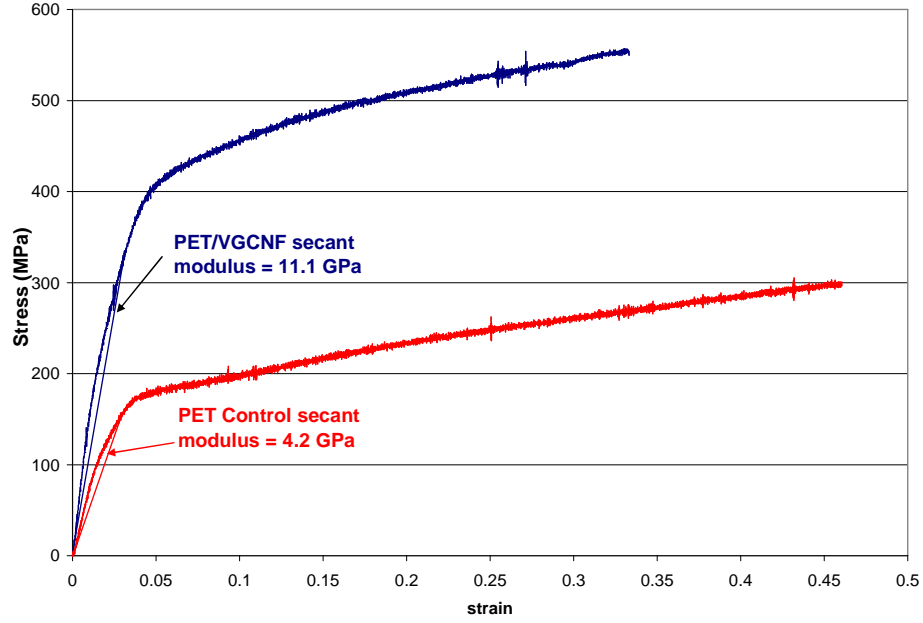


Figure 4.1. Stress-strain curve results from uniaxial tensile tests on PET control & PET-VGCNF samples

The results of the unfatigued samples indicate that the modulus of the PET-VGCNF samples was more than twice the value of the PET control samples. The fracture strength of the PET-VGCNF samples was also twice the value of the PET control samples. Similar results indicating a superiority in strength from the employment of VGCNFs into polymeric matrices have been obtained by the authors in [150]. These authors investigated the mechanical properties of VGCNFs employed in nylon and polypropylene composites and observed great improvements in tensile strength and elastic modulus. The results in the current research have been compared to the model by Cox [151]. The Cox model predicts the modulus value of the nanocomposite fiber for ideally oriented VGCNFs as:

$$E_c = V_m E_m + \left[1 - \frac{\tanh \beta}{\beta} \right] V_f E_f \quad (4.1)$$

Here, V_m represents the matrix volume fraction (96.4% in this case), E_m represents the matrix modulus (6.6 GPa from the experimental results), V_f represents the fiber volume fraction (which is 3.6% based on 5 wt% VGCNFs according to [128]), and E_f represents the VGCNF modulus (240 GPa according to [152]). The factor β is estimated according to the following expression:

$$\beta = \frac{l}{d} \sqrt{\frac{E_m}{(1 + \nu)E_f \times \ln(\pi / 4V_f)}} \quad (4.2)$$

Here, l represents the VGCNF length, d represents the VGCNF diameter, and ν represents Poisson's ratio of the matrix (taken as 0.37) [126]. According to the Cox model, the matrix modulus is highly dependent upon the aspect ratio (l/d). The authors in [128] have investigated the effect of nanocomposite fiber modulus on the aspect ratio and noticed that the modulus increases with increasing aspect ratio, and then plateaus off to a steady state value. Based on the values stated above and the results from the Cox model utilizing an aspect ratio greater than 50 (indicates approximate steady state value according to [128]), the nanocomposite fiber modulus was estimated and is shown in Figure 4.2. The results in Figure 4.2 show the prediction of the modulus as a function of VGCNF aspect ratio (l/d), as well as the average result of the experimental modulus calculated using the 1% strain calculation [13] and the secant modulus calculation. The graph in Figure 4.2 shows that the experimental results from the 1% strain modulus and secant modulus of the PET-VGCNF fibers were in the range of values for that predicted by the Cox model for fibers. Nanocomposite moduli predictions were computed for PET matrices containing VGCNF with moduli in the range $150 \leq E_f \leq 350$. This range of values was utilized, because in actuality, there was more than likely a statistical distribution of

aspect ratios (l/d) for VGCNFs that existed for the samples. The authors in [152] have reported that the modulus of VGCNFs is 240 GPa, and this modulus curve has been displayed as well. The objective of Figure 4.2 is to indicate that the experimental results obtained from this study are in accordance with results from the Cox model predictions when typical values for the modulus of the VGCNFs are implemented into the model.

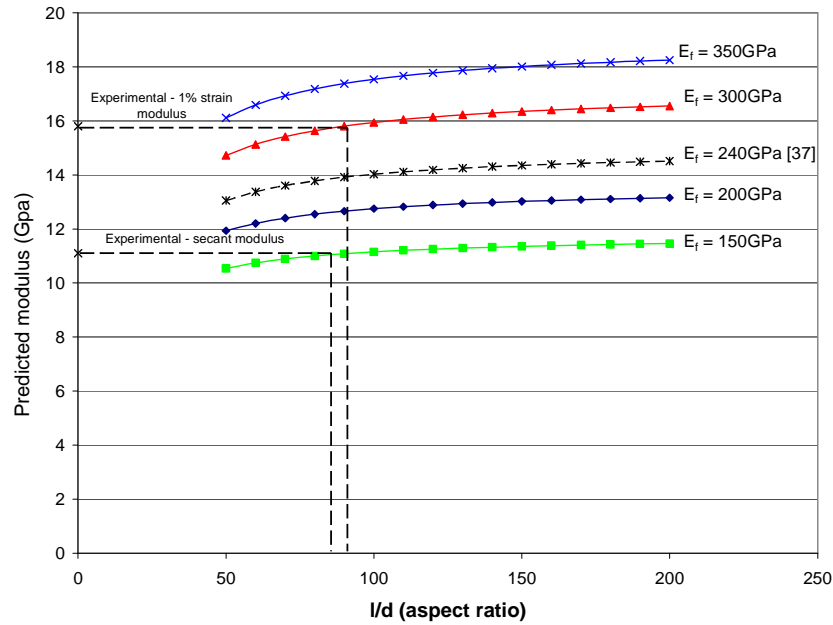


Figure 4.2. Cox model prediction of the elastic modulus as a function of aspect ratio

Determination of the yield point was an important parameter for characterizing the PET and PET/VGCNF samples under uniaxial tension. As described earlier, the nonlinearity of the stress-strain curve obscured the exact value of the yield point; however, the method as described in [130] was utilized to determine this value. Two intersecting lines based on the modulus value up to 1% strain and a hardening modulus in the later plastic stages (5% less than ε_m up to ε_m) were employed in the calculations for consistent determination of the yield stress based on the following set of equations:

From the elastic modulus:

$$\sigma_E = \left. \frac{d\sigma}{d\varepsilon} \right|_{\varepsilon=0}^{\varepsilon=0.01} \varepsilon + b_1 \quad (4.3)$$

From the hardening modulus:

$$\sigma_H = \left. \frac{d\sigma}{d\varepsilon} \right|_{\varepsilon=\varepsilon_{\max}-0.05}^{\varepsilon=\varepsilon_{\max}} \varepsilon + b_2 \quad (4.4)$$

In Equations (4.3) and (4.4), σ_E and σ_H represent the linearized form of the elastic stress and hardening stress evaluated between the given limits and b_1 and b_2 are arbitrary intercepts. These equations were set equivalent to one another and the yield stress and strain were defined by the vertical intersection line to the stress-strain curve (see Figure 4.3).

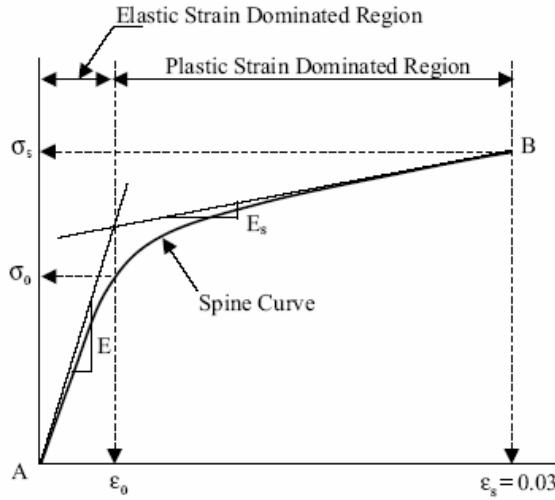


Figure 4.3. Stress-strain curve for material showing elastic and plastic regions depicting a method to determine the yield stress [130]

4.5. Fatigue Experimentation Phase

In this study, fatigue conditions were applied to the specimens, similar to the research in [129]. In essence, the fatigue tests performed in this experiment were not

totally destructive as in normal fatigue tests where the material is cycled to failure [131]. Rather, the fatigue cycles in these experiments were employed to make an assessment on the residual properties of the fiber subsequent to fatigue at a maximum load of approximately 60% of the fracture stress. The overall objective was to ultimately develop a correlation on the evolution of damage and change in mechanical properties of polymeric nanocomposite and pristine fibers subsequent to fatigue. In addition, a study was undertaken to determine if the load amplitude (load ratio) had an effect on the overall mechanical response of the fibers subsequent to fatigue. All fatigue tests were conducted at 5 Hz at load ratios of $R = 0$ and $R=0.333$ for the nanocomposite and control samples. Here, the load ratio R is defined as the ratio of the minimum to the maximum stress ($R = \sigma_{min}/\sigma_{max}$) during fatigue. The maximum fatigue load at which the samples were subjected to was 58% of the fracture stress for PET/VGCNF samples and 57% of the estimated fracture stress of PET control samples (approximately 60% of fracture stress in each case).

Figures 4.4 & 4.5 display a 1 s interval of the load vs. time and displacement vs. time response of the PET/VGCNF sample and the control sample under sinusoidal cyclic loading conditions between 0-15 g (PET/VGCNF) and 0-8 g (control PET) after equilibrium stress and strain values were reached. These samples were subjected to uniaxial fatigue loading conditions. From the graph, the phase lag components are clearly visible. Both the pristine sample and the nanocomposite specimen behaved similar to a viscoelastic solid, exhibiting small phase angle values between stress and strain for a fixed frequency of 5 Hz.

The dynamic viscoelastic behavior for both PET control and PET/VGCNF samples has been confirmed through DMA studies in [128], in which the authors have examined the effects of $\tan \delta$ vs. temperature for a frequency of 1 Hz and observed minute differences (Figure 4.6). Because it is known that $\tan \delta$ is a function of frequency in the elastic range [8], the observations in Figures 4.4 & 4.5 warrant a detailed DMA investigation at the 5 Hz frequency over a variation of temperatures for the PET and PET/VGCNF samples.

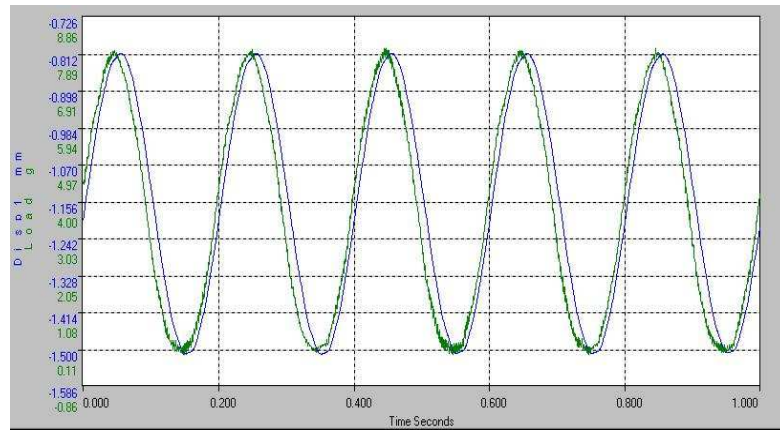


Figure 4.4. Oscilloscope output of load vs. time and displacement vs. time response of PET control sample undergoing uniaxial sinusoidal loading (Prescribed load values: 0-8 g-stress ratio=0 ($R=0$))

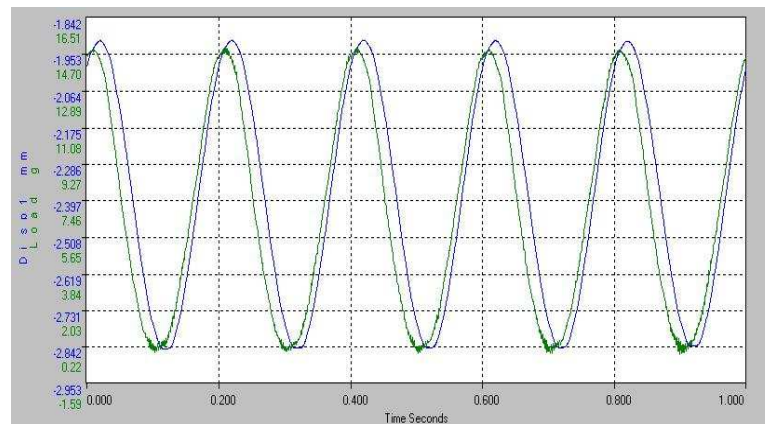


Figure 4.5. Oscilloscope output of load vs. time and displacement vs. time response of PET/VGCNF sample undergoing uniaxial sinusoidal loading (Prescribed load values: 0-15 g-stress ratio=0 ($R=0$))

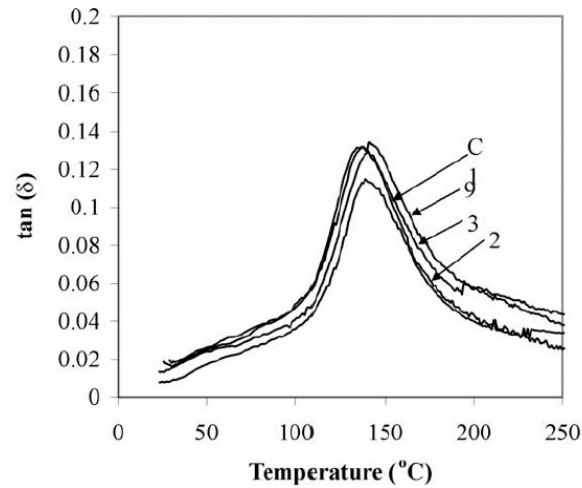


Figure 4.6. Dynamic mechanical analysis properties for PET control (C) and PET/VGCNF samples (9) [128]

4.6. Tensile Tests Subsequent to Load-Controlled Fatigue

A representation of the stress-strain response of fibers tested in uniaxial tension without prior fatigue and subsequent to fatigue is shown in Figure 4.7. The fibers that were exposed to fatigue were shifted according to the residual strain that remained as a result of the fatigue process.

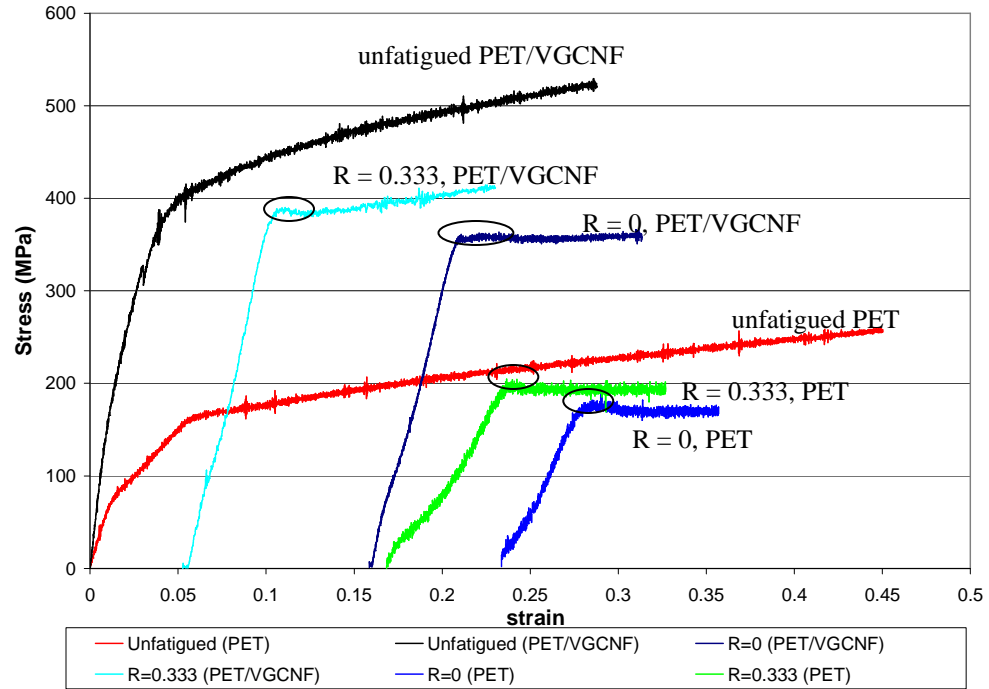


Figure 4.7. Residual stress-strain response of fibers in uniaxial tension subsequent to fatigue under various loading configurations. Note: Stress-strain curves have been shifted according to the residual strain due to the fatigue process. The circles highlight a dip in stress values.

For clarity, only one stress-strain curve is shown for each corresponding loading configuration in Figure 4.7. This figure is shown to elucidate the post-fatigue effects on the uniaxial stress-strain response of PET and PET/VGCNF filaments. From Figure 4.7, the following observations can be delineated regarding the unfatigued samples vs. the fatigued samples:

- 1) The constitutive stress-strain response changed from non linear elastic strain hardening with an ambiguous yield point to non-linear-elastic strain hardening with a more clearly defined yield point (piecewise non-linear elastic, strain hardening) and decreasing hardening modulus. This was true for both PET and PET/VGCNF samples tested subsequent to fatigue and will be quantified later.

- 2) In most samples tested subsequent to fatigue, there was a decrease in stress values which resembled a small “dip” in the stress-strain curve, similar to the behavior of some metals (see circled regions in Figure 4.7). This “dip” has been qualitatively explained in [132] for poly(ethylene terephthalate) samples tested in uniaxial tension and was attributed to an intrinsic yield process and/or a decrease in the cross-sectional area of the specimen (necking).
- 3) There was a reduction in hardening modulus for the fatigued samples vs. the unfatigued samples for PET and PET/VGCNF samples; this resembled a more perfectly plastic behavior subsequent to the static yield point, as seen in Figure 4.7. In essence, the hardening modulus gradually approached the horizontal condition as a function of residual strain. This will be elaborated upon in the discussion of the change in mechanical properties.

These observations clearly show the alterations in the uniaxial constitutive response as a result of fatigue for PET and PET nanocomposite samples. Effectively, there were changes in the overall constitutive response, the maximum stress, elastic modulus, hardening modulus, yield strain, and the amount of energy absorbed by the sample during the uniaxial tensile loading phase, which will be delineated in Figures 4.8-4.9 and Figures 4.11-4.18. In Figures 4.8-4.9 and Figures 4.11-4.18, the **bold** line at the relative value = 1 indicates the absolute value point for the unfatigued sample (refer to Table 4.1 for absolute values of the PET nanocomposite fiber and PET unreinforced fiber, respectively). Arrows pointing up (\uparrow) or down (\downarrow) depict the increase or decrease in the mechanical property value in the low residual strain limit, respectively. The

relative values in Figures 4.8-4.9 and Figures 4.11-4.18 were derived from the ratio of the fatigued mechanical property value to the unfatigued property value.

4.7. Mechanical Tests Subsequent to Fatigue

4.7.1. *Relative Tensile Stress Subsequent to Fatigue*

Figure 4.8 displays relative maximum stress values (within the stroke limitations of the fatigue machine) from the PET control and PET/VGCNF samples as a function of residual strain from the fatigue process. For both the PET control and PET/VGCNF samples, the results show a decreasing trend of fracture strength vs. accumulated strain. The results from Figure 4.8 show that the fatigue process conducted under $R=0$ conditions engendered irreparable damage to the sample with the accumulation of strain for PET/VGCNF samples. These results indicate that an accumulation of void sites may have been generated in the PET/VGCNF specimens as a result of the fatigue process. Interestingly, the results for the PET control samples in Figure 4.8 indicate a slight increase in the maximum stress for low residual strain values (less than approximately 5%). In fact, for the PET control samples in the low residual strain limit for the $R=0$ condition, five samples achieved a higher maximum stress with the retention of fatigue strain, indicating a strengthening mechanism from the fatigue process. After approximately 5% residual strain, the maximum stress values for the PET control samples showed a decaying behavior. From a comparative standpoint, the results in Figure 4.8 indicate that although the nanocomposite samples possessed an overall higher maximum stress value in the unfatigued state, the PET control sample possessed higher

relative maximum stress values subsequent to fatigue for all residual strain values in this study.

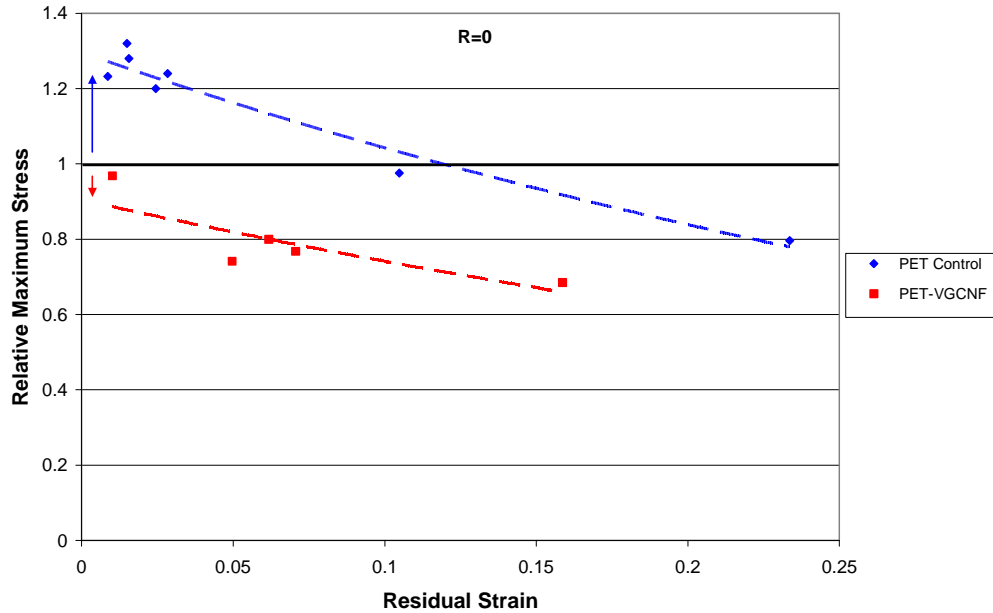


Figure 4.8. Relative maximum stress of PET/VGCNF and PET Control samples in uniaxial tension (subsequent to fatigue) vs. residual strain for the R=0 loading condition.

The data in Figure 4.9 are results of the relative maximum stress in uniaxial tension subsequent to fatigue for the condition R=0.333. These results indicate that the unreinforced PET relative maximum stress was higher in almost all cases for the same residual strain with reference to the nanocomposite sample. Similar to the results for the loading condition R=0, there was a spike in maximum stress values for low residual strains (up to approximately 7%) with an ensuing decay behavior. The results for the relative maximum stress for the PET/VGCNF sample were somewhat monotonic, with no sharp increases in relative maximum stress for low residual strain values. Combined, the results in Figures 4.8 and 4.9 indicate that the inclusion of VGCNFs into the PET matrix

adversely affected the maximum obtainable stress (fracture strength) in uniaxial tension subsequent to fatigue for $R=0$ and $R=0.333$ conditions. One explanation for the increase in maximum obtainable stress (in the low residual strain limit) for PET control samples could be that the fatigue process engendered an alignment of the polymer chains along the main axis, causing a shift from ductile to less ductile behavior in the sample. In fact, it will be later shown that for PET control samples tested subsequent to $R=0$ fatigue loading, there was an increase in the elastic modulus and hardening modulus in the low residual strain limit, supporting the claim that the PET samples were less ductile in the low residual strain limit.

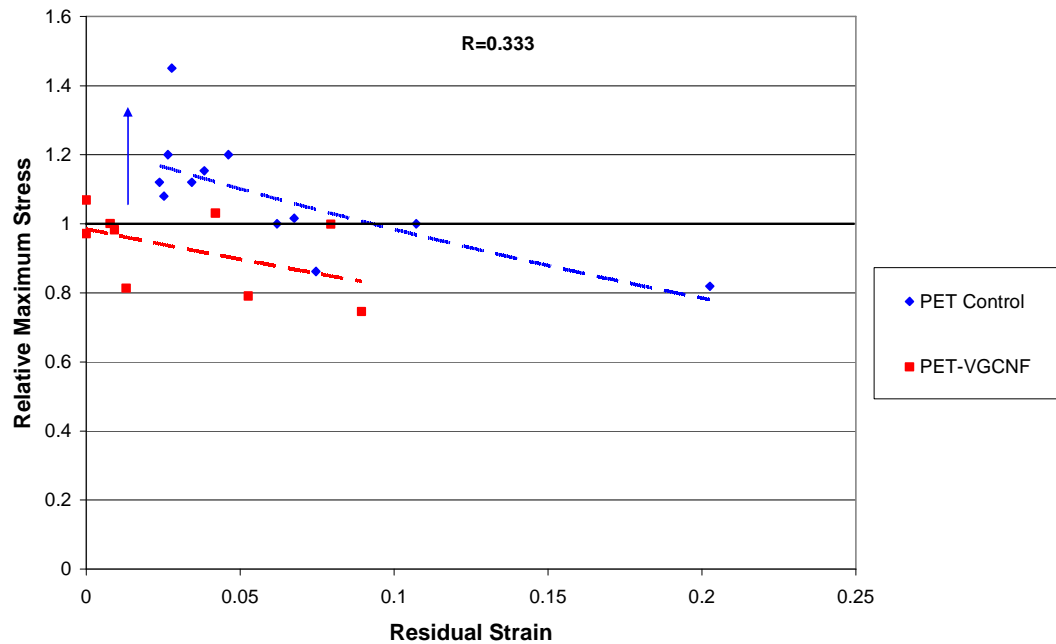


Figure 4.9. Relative maximum stress of PET/VGCNF and PET Control samples in uniaxial tension (subsequent to fatigue) vs. residual strain for the $R=0.333$ condition

4.7.2. Elastic Modulus Subsequent to Fatigue

There were obvious decreases in the elastic modulus (small strain limit modulus – up to 1%) for both PET and PET/VGCNF samples as a function of residual strain. A representative stress-strain curve of a PET/VGCNF sample that underwent 5,000 cycles under load-controlled conditions and 3.9% accompanying residual strain is shown in Figure 4.10.

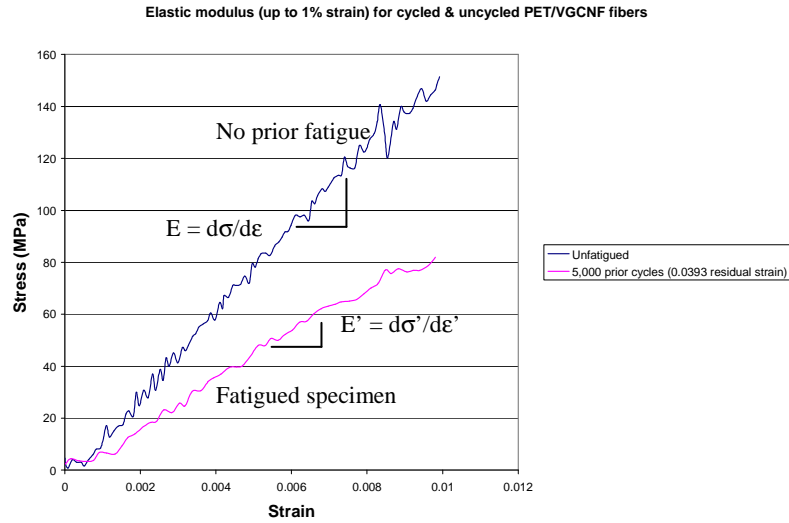


Figure 4.10. Representative elastic modulus of PET/VGCNF sample before and subsequent to fatigue (up to 1% strain)

This behavior is very similar to the Mullins effect observed by Mullins [133] in which a material is loaded to a defined strain value, and then subsequently reloaded to traverse a different stress-strain curve. The effect in Figure 4.10 exhibits the stress softening phenomenon as described by Mullins on the uniaxial loading of rubbers subsequent to fatigue.

Comparatively, in terms of the elastic modulus (which is an indication of the stiffness of the material), the nanocomposite showed greater signs of modulus

degradation with the retention of strain from the fatigue process. Figures 4.11 and 4.12 depict relative moduli of the PET and PET/VGCNF samples vs. residual strain for loading conditions $R=0$ and $R=0.333$, respectively. In Figure 4.11, the PET control sample showed a stiffening effect in the low residual strain limit, similar to the increased fracture strength behavior observed in Figures 4.8 and 4.9. The nanocomposite samples exhibited no signs of stiffening subsequent to fatigue; rather a severe reduction in modulus was observed for small residual strain values for both $R=0$ and $R=0.333$ loading conditions (Figures 4.11 and 4.12). Although the literature suggests a significant increase in modulus for nanocomposite materials [48-51, 59] and an overall stiffer material, these results suggest that stress-controlled fatigue conditions that result in an ensuing residual strain for PET-VGNF materials can cause severe reductions in the elastic modulus.

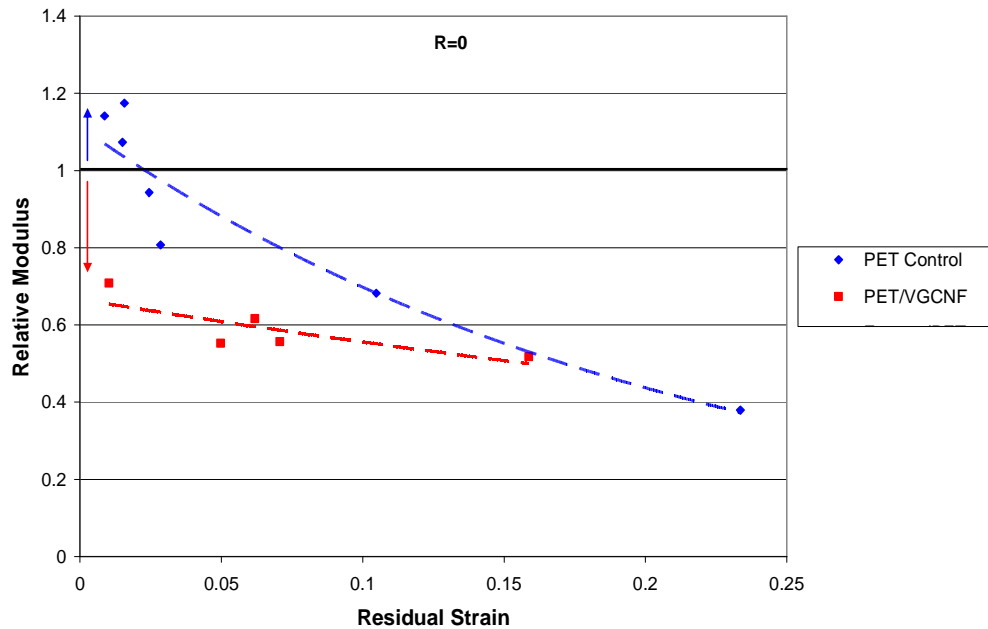


Figure 4.11. Relative elastic moduli of PET control and PET/VGCNF samples (subsequent to fatigue) vs. residual strain for the $R=0$ loading condition

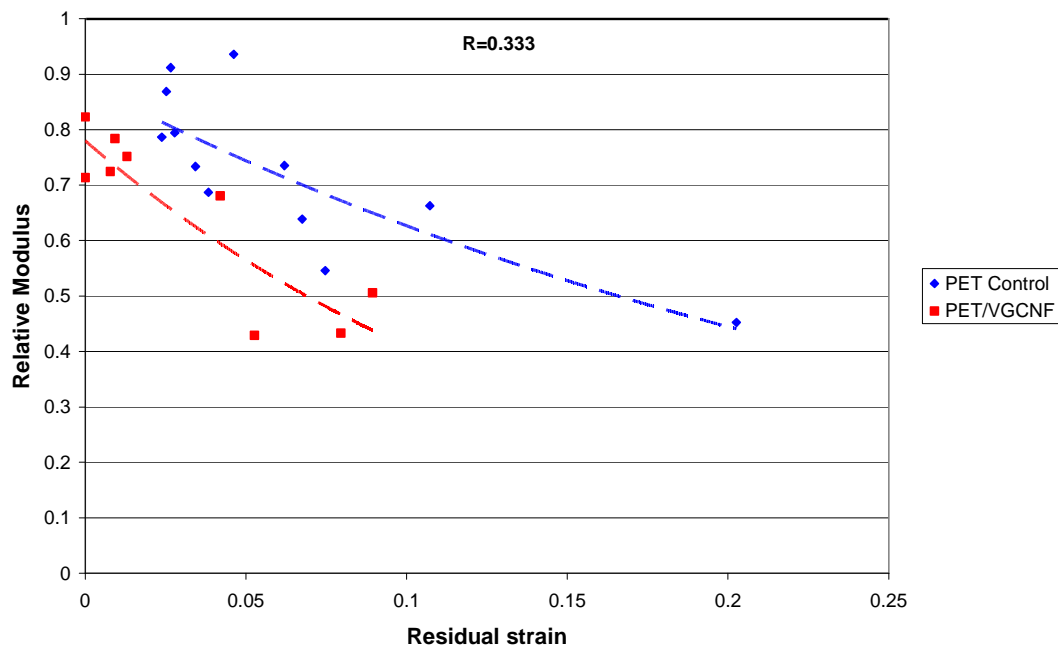


Figure 4.12. Relative elastic moduli of PET control and PET/VGCNF samples (subsequent to fatigue) vs. residual strain for the R=0.333 condition

4.7.3. Tensile Energy Analysis of Fibers in Uniaxial Tension Subsequent to Fatigue

Another primary indicator of the damage accumulation in materials due to the fatigue process is the measurement of total energy under the load-displacement curve in uniaxial tension. Measurements of the relative tensile energy were plotted vs. residual strain to determine the effects of fatigue on the energy absorption capabilities of the PET control and PET/VGCNF samples. Figures 4.13 and 4.14 display relative tensile energy results for the R=0 and R=0.333 condition, respectively. Although there is some scatter in the data, Figures 4.13 and 4.14 clearly illustrate the degenerative effects from the fatigue process. The lines that are provided on the graphs in Figures 4.13 and 4.14 are meant to guide the eye and are not actual trendlines of the decay behavior. These results are somewhat intuitive, as one expects less energy to be available to the sample to

perform useful work after the accumulation and retention of strain from the fatigue process. After all, some of the internal energy of the sample was converted to hysteresis heat during the fatigue process and some was utilized for changing the underlying microstructure of the pristine sample, inducing polymer chain alignment along the fiber axis. Similar to the results obtained for the maximum stress and the elastic modulus, the PET control samples displayed an increase in energy absorption in the low residual strain limit for the $R=0$ condition. In terms of tensile energy capabilities, the nanocomposite sample showed lower values with respect to the unreinforced sample for both $R=0$ and $R=0.333$ conditions. The results in Figure 4.14 indicate that some PET/VGCNF samples displayed higher energy absorption values in the low residual strain limit; however, the trend was not consistent for similar residual strain values. There is much more scatter in the data in Figure 4.14, which may have arisen from slight differences in sample structure, etc.

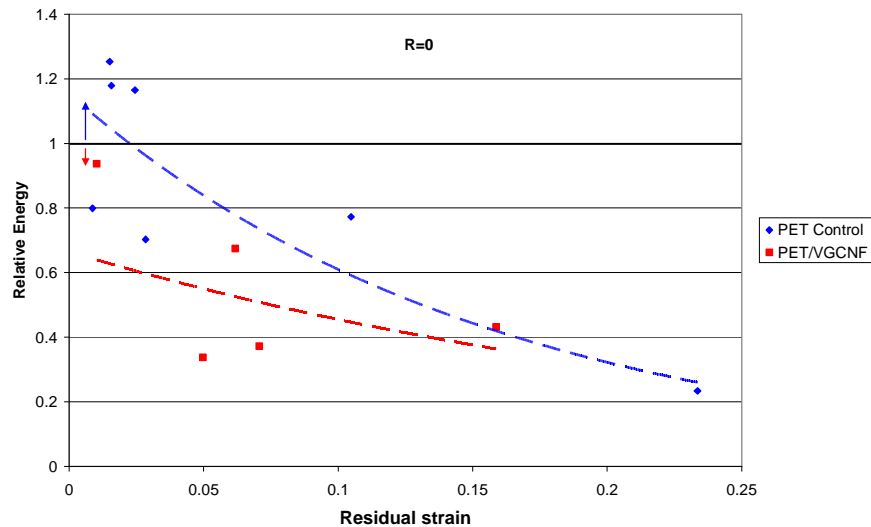


Figure 4.13. Relative total energy of PET control and PET/VGCNF samples (subsequent to fatigue) vs. residual strain for the $R=0$ loading condition (Trendline is not an actual representation of the decay behavior)

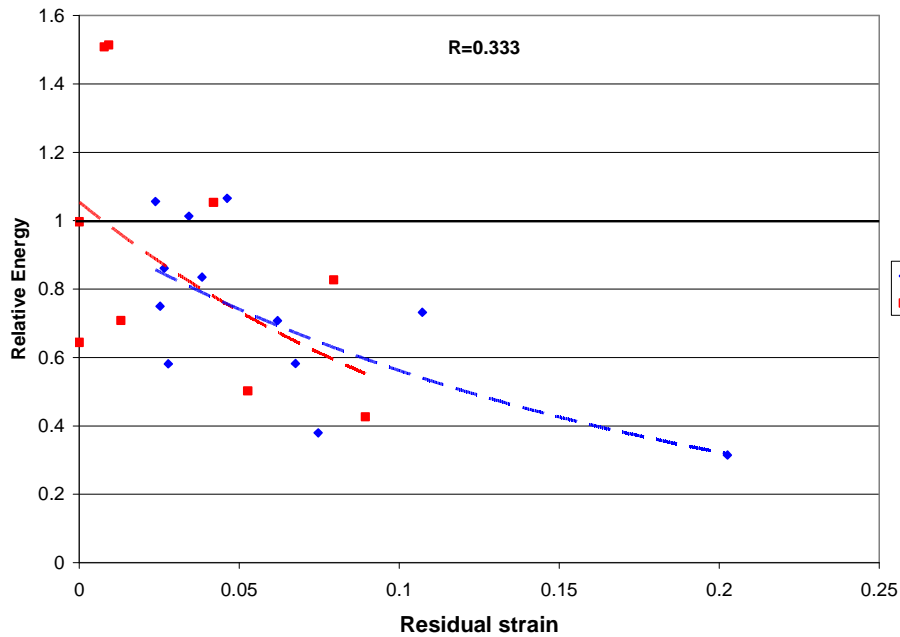


Figure 4.14. Relative total energy of PET control and PET/VGCNF samples (subsequent to fatigue) vs. residual strain for the $R=0.333$ condition (Trendline is not an actual representation of the decay behavior)

4.7.4. Hardening Modulus Subsequent to Fatigue

The hardening behavior of samples was also studied to obtain post-yield deformation information about the samples before and subsequent to fatigue. The hardening modulus provides an indication of the behavior of the sample in the plastic dominated region, as indicated in Figure 4.3. The hardening modulus indicates the resistance of the material after it has yielded, indicating a resistance to plastic flow behavior. The results in Figure 4.15 and 4.16 clearly indicate that the nanocomposite sample (PET/VGCNF) demonstrated a greater proclivity to plastic flow (less hardening) subsequent to fatigue loading at ratios of $R=0$ and $R=0.333$. In fact, for the PET/VGCNF sample, only one relative hardening modulus value fell above the threshold for the unfatigued sample in Figures 4.15 and 4.16 (bold line), indicating a reduction in the

modulus as the result of fatigue. The PET/VGCNF hardening behavior for the $R=0.333$ condition was fairly monotonic, with no significant increases or decreases observed as a function of residual strain. For comparison, the control PET sample showed slight increases in the hardening modulus in the low residual strain limit, further corroborating the possibility of a strengthening mechanism responsible for improved mechanical behavior in PET filaments with the retention of small strains from fatigue. This was consistent for both $R=0$ and $R=0.333$ loading conditions. Future studies need to be performed to further quantify the mechanism responsible for the decrease in mechanical properties and overall mechanical behavior of PET nanocomposites with the retention of strain from the fatigue process. Cho et al. [27] have already confirmed that strain hardening is a dominating effect in the early stages of cyclic extension, and defects are more dominating in the latter stages of fatigue. The results of the study from [27] are in accordance with the results in Figures 4.8-4.9 and Figures 4.11-4.18 presented in the current research.

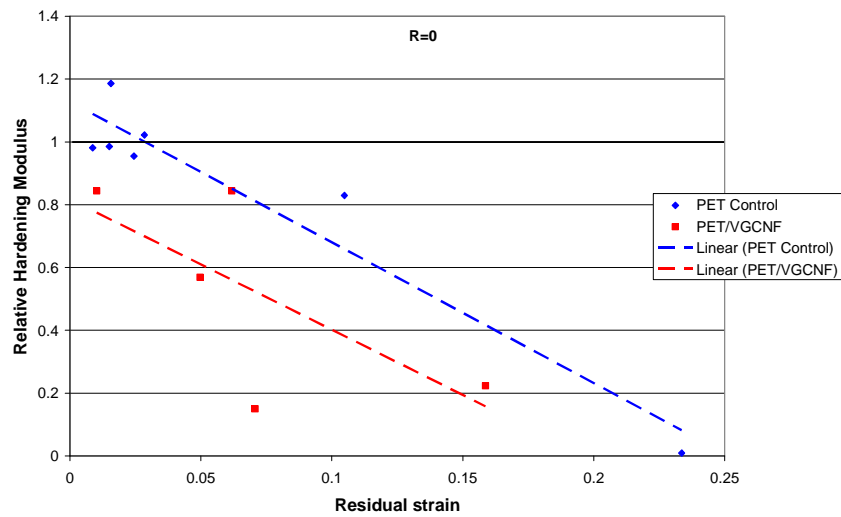


Figure 4.15. Relative hardening modulus of PET control and PET/VGCNF samples (subsequent to fatigue) vs. residual strain for the $R=0$ loading condition

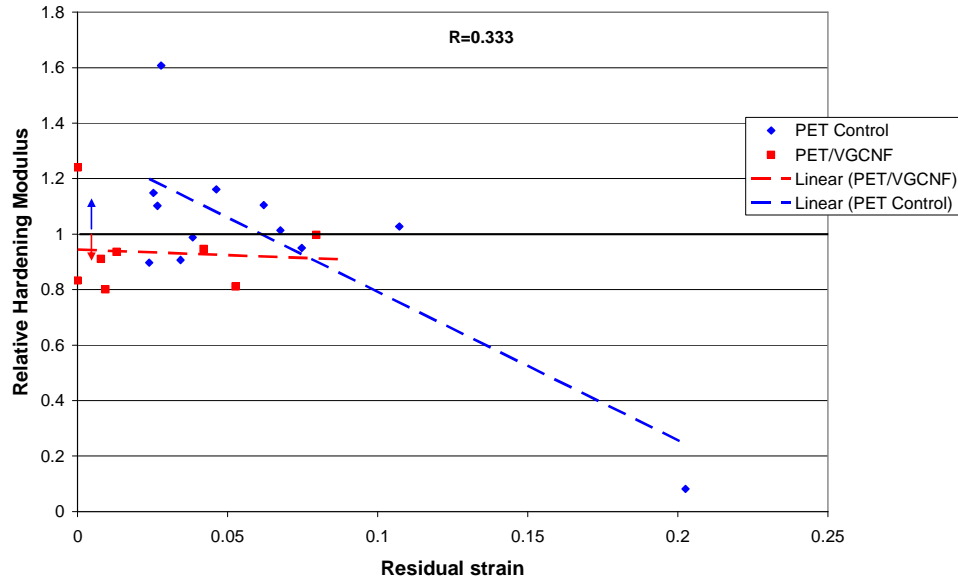


Figure 4.16. Relative hardening modulus of PET control and PET/VGCNF samples (subsequent to fatigue) vs. residual strain for the R=0.333 condition

4.7.5. Yield Strain Subsequent to Fatigue

The yield strain values of the single filaments subsequent to fatigue were also evaluated to determine the effects of residual strain. Figures 4.17 and 4.18 depict the relative yield strain as a function of residual strain for the PET control and nanocomposite sample. The results clearly show that residual strains in the material caused an increase in the yield strain of the deformed material. In essence, subsequent to fatigue, the material possessed a new length:

$$L' = L_0 + \Delta L \quad (4.5)$$

The post-fatigue engineering yield strain was defined in terms of the undeformed length as:

$$\varepsilon_y' = \frac{\delta_y}{L'} \quad (4.6)$$

In (4.5) and (4.6), δ_y represents the yield displacement, L' represents the new length of the sample, L_0 represents the undeformed length of the specimen, ΔL represents the residual length that remained as a result of fatigue, and ε_y' represents the yield strain of the fatigued (deformed) sample. The results in Figures 4.17 and 4.18 indicate that the yield strain in the fatigued PET control and PET/VGCNF (deformed) samples was inhibited as a result of creep strain retention. Also, from a relative standpoint, the results seem to indicate that the relative yield strain in the PET control samples showed a greater dependence on the residual strain for both R=0 and R=0.333 loading conditions.

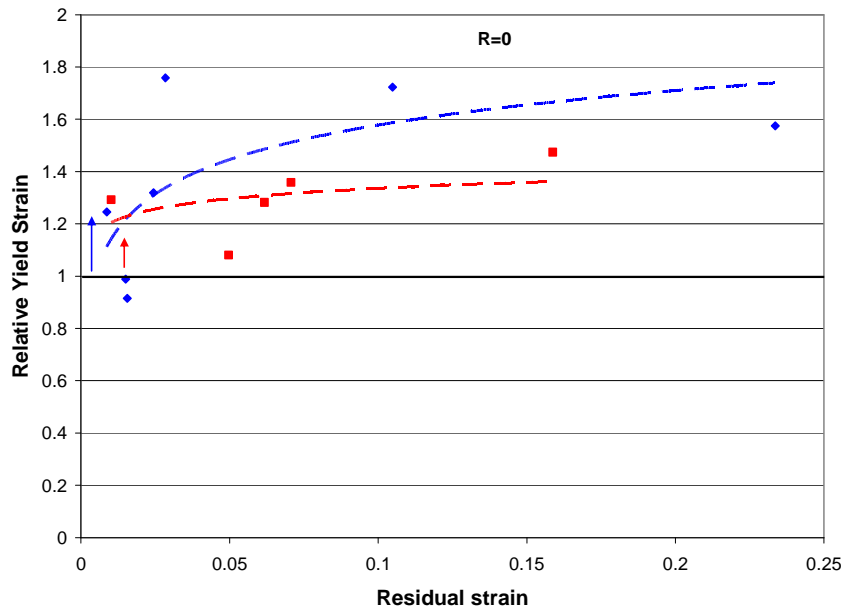


Figure 4.17. Relative yield strain of PET control and PET/VGCNF samples (subsequent to fatigue) vs. residual strain for the R=0 loading condition

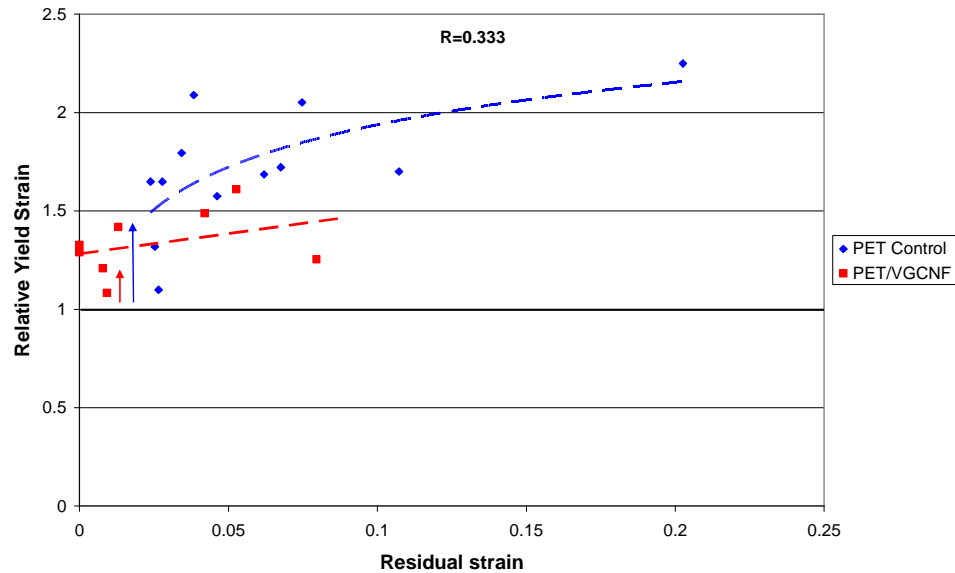


Figure 4.18. Relative yield strain of PET control and PET/VGCNF samples (subsequent to fatigue) vs. residual strain for the $R=0.333$ condition

4.8. SEM Fractography

Scanning electron microscopy (SEM) experiments were conducted to determine the effects of fatigue loading conditions on the fracture morphology of the PET unreinforced and PET/VGCNF single fibers. The results from the SEM study substantiate the quantitative results obtained from Sections 4.2-4.7, supporting the claim that the nanocomposite fibers degraded more significantly with the accumulation and retention of residual strains than its unreinforced counterpart (PET control). Figure 4.19 indicates that the fracture morphology of the unfatigued and fatigued PET samples was similar. The sample was fatigued at a stress ratio of $R = 1/3$ with a corresponding residual strain equivalent to 2.4%. The PET sample tested without prior fatigue displayed a fracture pattern similar to fracture of fibers seen in the literature [33]: 1) initiation of fracture point, 2) opening of a v-notch and 3) progression to unstable fracture

orthogonal to the fiber axis. The unfatigued unreinforced PET samples (Figure 4.19 (a)) showed a similar morphology and fracture behavior as the fatigued samples (Figure 4.19 (b)) (stable v-notch opening then progression to unstable fracture). However, there was a slight difference. From the fatigue process, several microfailure splits were created along the fiber axis, indicating a slight accumulation of damage in the material.

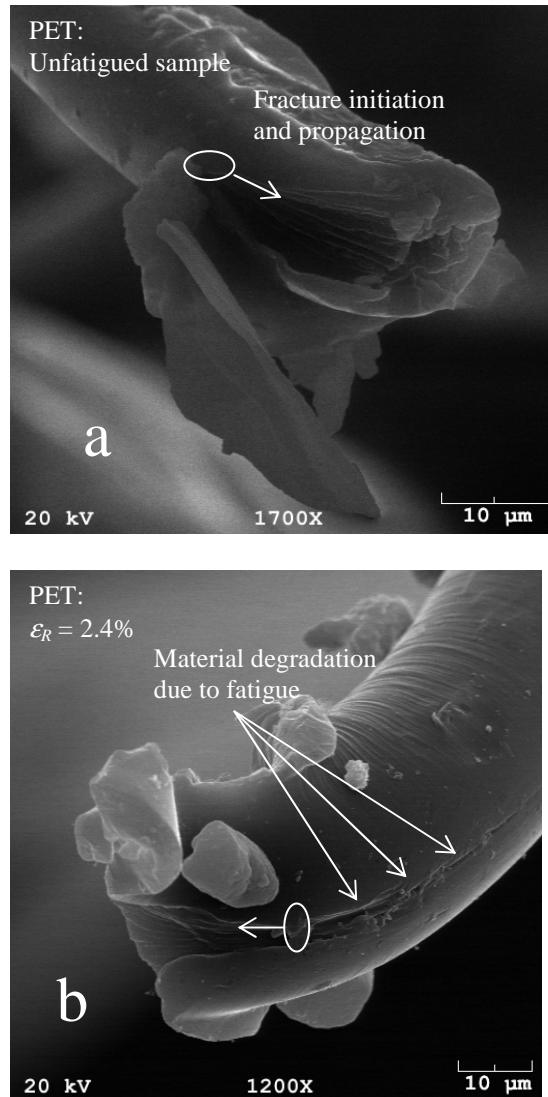


Figure 4.19. (a) SEM fractograph of a PET unreinforced specimen without prior fatigue (uniaxial tensile fracture) and (b) specimen with prior fatigue and 0.024 (2.4%) residual strain from fatigue process indicated slight material degradation due to tiny microfailures along fiber axis

In contrast to the PET unreinforced samples, the PET/VGCNF fatigued samples exhibited a distinct difference in fracture morphology from the unfatigued samples. Figure 4.20 (a) displays an unfatigued PET/VGCNF sample with no prior fatigue, demonstrating that the sample fractured in a manner similar to that of PET control samples. However, Figures 4.20 (b) and 4.20 (c) display images of PET/VGCNF samples that have been fatigued at stress ratios of $R=1/3$ with corresponding residual strains of $\epsilon_R = 0.78\%$ and $\epsilon_R = 0.93\%$, respectively. Defibrillation and decohesion mechanisms of the reinforcing agent from the PET matrix are clearly observed in Figures 4.18 (b) and 4.18 (c). Further, the results from Sections 4.2-4.7, which indicate that the nanocomposite fibers experienced greater degradation than their unreinforced counterparts, are supported by Figures 4.20 (b) and 4.20 (c). In comparison with the PET fatigued sample at a residual strain of 2.4% (Figure 4.19 (b)), the nanocomposite fibers in Figures 4.20 (b) and 4.20 (c) exhibited lower residual strain values of 0.78% and 0.93%, respectively. This indicates that the fatigue process in PET/VGCNF samples precipitated more fracture zones for lower residual strain values than their unreinforced counterparts, leading to lower relative residual strengths. In the next section, a discussion will be provided that seeks to further explain these changes in mechanical properties and fracture morphology as a result of fatigue loading.

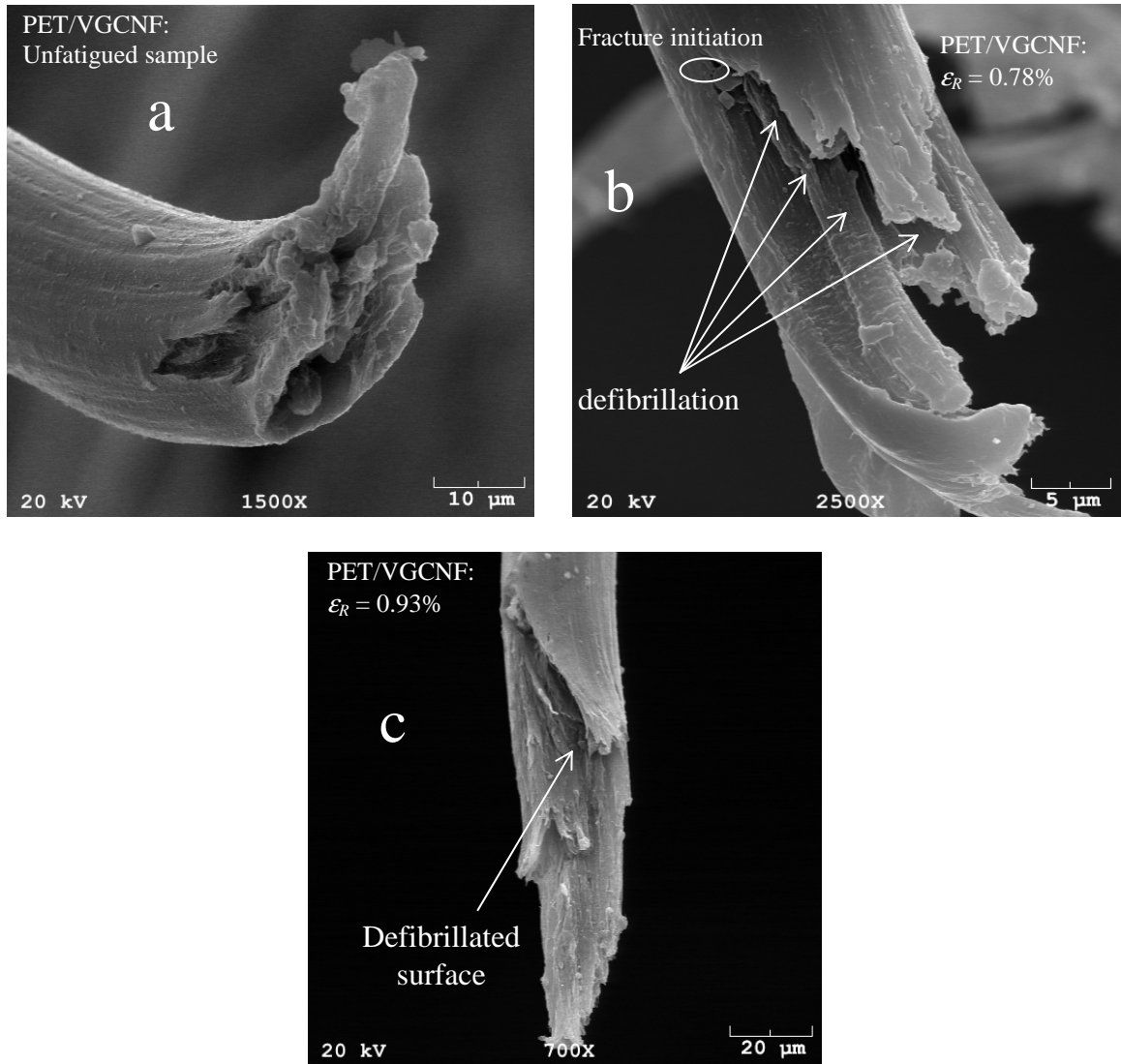


Figure 4.20. (a) SEM fractograph of a PET/VGCNF specimen without prior fatigue (uniaxial tensile fracture), (b) specimen with prior fatigue and 0.0078 (0.78%) residual strain from fatigue process indicated highly distorted and tortuous crack pattern and (c) PET/VGCNF specimen with prior fatigue and 0.0093 (0.93%) residual strain from fatigue process indicating defibrillation along the fiber axis

4.9. Further Discussion

All of the results in Figures 4.8-4.18 regarding mechanical property changes as a function of residual strain suggest that further investigation should be made into effects of maximum fatigue load levels with respect to plastic deformation. For this study, the maximum fatigue loads were similar with respect to the maximum load (stress) of the

sample in uniaxial tension without prior fatigue. As stated earlier, for both PET/VGCNF and PET control samples, maximum fatigue load levels corresponded to approximately 60% of the maximum stress of the material in uniaxial tension without prior fatigue ($\sigma_{\max}=0.58\sigma_f$ for PET/VGCNF and $\sigma_{\max}=0.57\sigma_f$ for PET control). However, from a comparison of the results in Table 4.1, the PET control sample was more ductile than the PET/VGCNF sample with 5 wt% nanofiller. This was indicated by comparing the fracture strains (ϵ_f) in Table 4.1. The results indicate that the fracture strain for the unfatigued PET control sample was approximately 0.46 based on the samples that fractured and the SD band in Table 4.2. The fracture strain for the unfatigued PET/VGCNF sample was 0.28 ± 0.050 . Thus in terms of testing parameters, the samples were subjected to similar maximum loads under fatigue conditions with respect to their fracture stress values; however, with respect to yield conditions, the samples experienced different types of stresses during fatigue and retained different types of residual strains. The results in Figures 4.8-4.18 indicate that the PET samples retained both creep and plastic strains from fatigue (viscoplastic), whereas the PET/VGCNF samples only retained mostly creep (viscous) strains (though localized yielded regions could have been created). This can be further analyzed by considering the maximum stress during fatigue for both samples in comparison to the calculated yield stress values. The PET control samples were cycled at maximum stress values equivalent to $1.5\sigma_0$, whereas the PET/VGCNF samples were cycled at maximum stress values equivalent to approximately $0.98\sigma_0$. The results are interesting because they elucidate that cycling at stress values for similar ratios of the maximum stress for unreinforced materials and composites engender different results for material property changes, due to the differences in the onset to

plastic deformation in the samples. In fact, the literature suggests that microstructural changes occur as the result of plastic deformation, which could partially explain the difference in material property changes as a function of residual strain for the PET control and PET/VGCNF samples. Achibat et al. [134] have performed low frequency Raman scattering measurements on shear yielded PMMA samples below the glass transition temperature (T_g) to conclude that microstructure is affected even in the case where load-unload specimens are unloaded to macroscopically identical zero stress conditions. The specimens were yielded under various conditions and the results showed that 1) anisotropy decreased in PMMA specimens cyclically loaded above the yield point with respect to undeformed specimens and 2) low-frequency Raman (LFR) data showed an excess scattered intensity in the 30-50 cm^{-1} range for plastically deformed specimens under simple shear conditions. In addition, Averett et al. [129] have shown that the yield stress subsequent to fatigue loading is clearly a function of the ratchet (accumulated) strain induced under load-controlled fatigue conditions for nylon 66 single filaments. Also, the plastic and elastic energies of filaments tested subsequent to fatigue were shown to be decreasing functions of accumulated fatigue strain. Conformational changes have also been confirmed to occur in polymers as a result of mechanical loading in the yield threshold range. Aoyama et al. [135] have observed conformational shifts from gauche-to-trans as a function of strain for neat PBT and PBT/rubber blends utilizing Raman spectroscopy measurements. The neat (unreinforced) PBT specimens displayed a rapid increase of gauche-to-trans conformations at approximately 10% strain, which was associated with the onset of plastic deformation (yielding) in the specimen. The reinforced samples displayed almost 100% degree of transformation from gauche to trans

at a maximum strain of 50% while the unreinforced samples underwent diminutive changes of 20% degree of transformation at 50% strain. These results are similar to increases in trans content as a function of strain for poly(ethylene terephthalate) sheets that were observed from infrared (i.r.) spectroscopy studies by Cunningham and Ward [136] and Hutchinson et al. [137].

With the aforementioned observations in mind, the following relationship is presented for residual strains in PET and PET/VGCNF samples as result of fatigue at similar maximum load levels:

For PET control samples,

$$\varepsilon_{R,cont} = \frac{\delta_R}{L_0} = \frac{\delta_c + \delta_{pl}}{L_0} \quad (4.7)$$

and for PET/VGCNF samples,

$$\varepsilon_{R,VG} = \frac{\delta_R}{L_0} = \frac{\delta_c}{L_0} \quad (4.8)$$

In (4.7) and (4.8), $\varepsilon_{R,cont}$ and $\varepsilon_{R,VG}$ represent the residual strain for the PET control and PET/VGCNF sample, respectively, δ_c represents the elongation that remained in the sample as a result of creep (viscous) deformation during constant-loading fatigue, and δ_{pl} represents the plastic deformation that was engendered in the PET control sample. For a further comparison of the results in Figures 4.8-4.18, an interesting study would be for one to decouple the creep and plastic strains as denoted in (4.7) for the PET sample, and investigate the change in material properties as a function of residual creep strains. What is clear from this study is that PET/VGCNF fibers loaded under viscoelastic fatigue conditions suffer defibrillation and decohesion for low residual creep strains (as low as

0.78%), while the PET unreinforced samples show a similar fracture morphology even for creep strains as high as 2.4%.

Conclusions from Chapter 4

Mechanical property characterization and fatigue tests have been performed on PET control and PET/VGCNF samples. In terms of uniaxial tension, for the unfatigued samples the PET nanocomposite (PET/VGCNF) sample exhibited superior mechanical properties. To determine the influence of cyclic loading on material property changes, fatigue loading at ratios $R=0$ and $R=0.333$ was conducted on the PET/VGCNF and PET control samples at ratios of approximately 60% of the fracture stress. Subsequent to fatigue loading, uniaxial tensile tests were conducted on the deformed samples to ascertain residual strength behavior. From a relative standpoint, the residual material properties of the PET control sample and PET/VGCNF samples were shown to be closely correlated with the residual fatigue strains. In addition, a tendency for necking was indicated by a drop in stress values for fatigued PET control and PET/VGCNF specimens, based on results from the literature.

From a relative standpoint, the PET/VGCNF samples showed greater deterioration in mechanical properties as a result of fatigue. This was supported through analysis of residual strength mechanical response and SEM fractography. From the SEM study, defibrillation and decohesion mechanisms were noticed for the fatigued PET/VGCNF samples. From the residual strength analysis, the PET control samples showed an increase in maximum stress, elastic modulus, hardening modulus, and tensile energy for small residual fatigue strains, supporting the claim in the literature that strain

hardening occurs in early stages of cyclic extension. In addition, for both PET control and PET/VGCNF samples, the onset of yield under uniaxial tension was modified as a result of the fatigue process, as indicated by the increase in yield strain as a function residual strain. The difference in ductility and maximum fatigue stress in relation to the yield stress of the PET control and PET/VGCNF samples may indicate that the difference in mechanical property changes as a function of residual strain from a relative standpoint can be explained by the fact that the PET control sample was more susceptible to yield. When subjected to maximum fatigue loads corresponding to 60% of the fracture stress, both creep and plastic strains were engendered in the PET control samples, whereas only creep strains were engendered in the PET nanocomposite (PET/VGCNF) sample. In sum, the results from this study indicate that PET unreinforced samples can withstand a larger accumulation of strain from the fatigue process conducted at 60% of the maximum fatigue stress as compared with PET/VGCNF 5 wt% nanocomposite samples.

CHAPTER 5

RESIDUAL PROPERTY PREDICTIONS OF PET AND PET-VGCNF FIBERS: MODELING AND PREDICTION USING ARTIFICIAL NEURAL NETWORKS

Summary of Chapter 5

A set of experiments has been performed on poly(ethylene terephthalate) (PET control) and PET fibers with vapor grown carbon nanofibers (PET-VGCNF) to assess the mechanical integrity of the materials due to a repeated cyclic loading. Artificial neural networks (ANNs) have been used to examine the residual strength and elastic modulus degradation behavior of the filaments as a function of the input mechanical testing variables (maximum fatigue stress- σ_{max} , stress ratio- R , # cycles- N , undeformed modulus- E) and a damage variable that has been identified as the residual strain from fatigue, ϵ_R . The exact relationship of how these input variables relate to the degradation of the elastic modulus, E , and the fracture strength, σ_f , has been determined. The results of this study are two-fold. First, the results indicate that ANNs can be used to predict the residual strength and modulus degradation behavior of PET and PET/VGCNF single filaments under various loading conditions. Backpropagation (BP) with momentum and conjugate gradient algorithms have been utilized to successfully train a multilayer perceptron (MLP) network for modeling the mechanical behavior of single polymeric filaments subsequent to fatigue loading. Second, the results indicate that the mechanical behavior of the PET control and PET-VGCNF differs as a function of the input fatigue conditions that are prescribed. The main difference was that the PET control samples exhibited a distinct hardening effect in the low residual strain limit and this was not observed for the PET-VGCNF samples (This has been previously discussed in Chapter 4). The employed

neural networks were successful at replicating the hardening behavior for the PET control samples and the mechanical behavior changes for the PET-VGCNF samples as a function of σ_{max} , R , and ε_R .

5.1. Introduction

The scientific and engineering community has experienced great research and commercial success of nanocomposite materials over the past decade. In particular, the polymer science community has realized great enhancements in mechanical behavior, with regards to the nano-sized agents that are infused into a polymeric matrix. A critical area of nanocomposite materials that must be addressed is damage induced from fatigue loading conditions. In conventional materials, damage is typically characterized in terms of dislocation density or microcrack density used in boundary value continuum mechanics problems due to the fact that elasticity is directly correlated with damage. This elasticity to damage correlation is confirmed because the number of atomic bonds decreases with damage [118]. In our current state of engineering, it is arduous to develop a prognostic model based solely on dislocation or crack density considerations [108,119]. Thus one has to measure degradation of the global mechanical properties, such as elastic modulus and fracture strength, to represent the evolution of dislocation density or microcrack density. Inelastic strain is also considered to be related to fatigue damage evolution [108].

There have been few studies that implement a damage parameter into an ANN structure for determination of material degradation due to fatigue loading in polymer fibers and their nanocomposites. In the current research, the damage parameter that has

been implemented is a fraction of the viscous portion of the creep strain that remained as a result of fatigue loading conditions. This type of analysis differs from that of traditional fatigue analysis and S-N curve analysis because of the incorporation of a material tracking parameter as well as mechanical testing parameters that are related to the overall residual mechanical properties of the material. In essence, the current analysis extends the traditional fatigue analyses from a history and time-based approach to a hybrid history and material state-based approach. The results of this research seek to complement and expand the traditional analyses of fatigue where a prior history and number of cycles must be prescribed for prediction of failure. The research in this analysis was “state-based” in the sense that the “state” of material properties was evaluated at discrete intervals during the fatigue test. ANN models were implemented to transform the discrete model into a continuous model that was capable of tracking the degradation in material behavior over the length of the test. The results from this research could be used in applications where imminent failure detection due to fatigue in materials or structures is necessary.

5.2. Damage Parameters

In the context of the current research, damage was defined as the gradual degradation of the material and was an intrinsic material property dictated as a damage variable [108]. As stated in the literature review, elastic modulus degradation and residual strength degradation can both be used as damage metrics. For the residual property predictions, the behavior of both residual strength and residual modulus were measured as a function of an input vector set that was supplied to the neural network

5.3. Experimental Methods

5.3.1. *Sample Preparation and Mechanical Testing*

The PET and PET/VGCNF specimens were prepared and processed at the Georgia Institute of Technology according to [128]. The details of the specimen preparation and the mechanical testing paradigm are provided in [129]. The BOSE® ELectroForce® (ELF®) 3200 tensile and fatigue testing machine (Enduratec)) was used to conduct the mechanical experiments in uniaxial tension and uniaxial cyclic loading. All experiments were conducted at room temperature, laboratory air. The typical humidity of the laboratory air was approximately 50% (see [129] for more testing details).

5.3.2. *Application of Artificial Neural Networks (ANNs) - Introduction to ANNs*

In the current research study, ANNs were utilized for the prediction of the residual mechanical properties of both unreinforced and nanocomposite PET fibers. The Neurosolutions 5 software package [99] was utilized to perform the neural network training and simulations. Neurosolutions 5 is equipped with a variety of neural network architectures and training algorithms that can be used for analysis. Specifically, in this research, multilayer perceptron (MLP) networks were used with various learning algorithms for proper training of the network.

The MLP is a simple feedforward ANN architecture that was utilized to relate a specific set of input variables to a singular output variable. In this manuscript, the input variables consisted of the mechanical testing conditions and one damage parameter, and the output variables consisted of the residual strength or the residual elastic modulus, as

will be described in Sections 5.5.3 and 5.5.4. MLPs were trained with the following learning algorithms to minimize the cost function (MSE):

- static backpropagation with momentum
- conjugate gradient

The most popular of these methods is the backpropagation scheme, which literally refers to a backwards propagation of errors throughout the network.

5.4. Learning Paradigms Used for Computation

5.4.1. *Standard backpropagation and backpropagation with momentum learning*

Backpropagation is the most widely used and universal learning algorithm for optimization in neural network schemes [85]. The backpropagation scheme implements the steepest descent method (gradient descent method) [86]. The researchers in [84] have provided a very thorough and detailed explanation of backpropagation and other learning algorithms for applications to polymeric materials. During each iteration of computation, the weights were continually adjusted in the direction of which the error function decreased the most. To visualize the anatomy of the backpropagation network in more detail, consider Figure 5.1, where three layers exist for the computational procedure: an input layer, a hidden layer, and an output layer. A network structure similar to that in Figure 5.1 was used for the residual property evaluations in the current chapter.

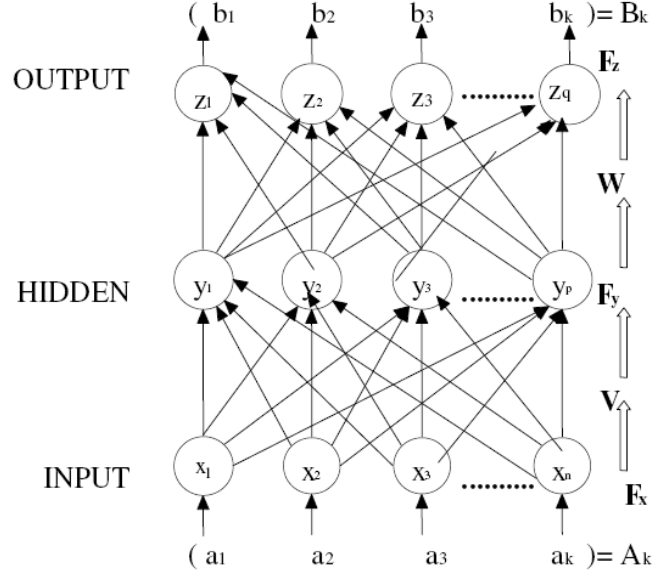


Figure 5.1. Topology of a three-layer feedforward backpropagation network [84]

The output of the F_z processing elements (PEs), z , was computed as:

$$z_j = \sum_{i=1}^p y_i w_{ij} \quad (5.1)$$

Here, w_{ij} represents the weight of the connection between the i_{th} and j_{th} PEs. Because most complex problems necessitate the usage of nonlinear analysis, hidden layers were employed, in which an activation function, f , was introduced as:

$$y_i = f\left(\sum_{h=1}^n a_h v_{hi}\right) = f(r_i) \quad (5.2)$$

In the current research, the activation function utilized was the hyperbolic tangent function (TanhAxon in Neurosolutions).

The error between the HIDDEN and OUTPUT layers (see Figure 5.1) was adjusted utilizing the following relationship:

$$\frac{\partial E}{\partial w_{ij}} = \frac{\partial}{\partial w_{ij}} \left[\frac{1}{2} \sum_{j=1}^q (b_j - z_j)^2 \right] = (b_j - z_j) y_i = \delta_j y_i \quad (5.3)$$

Here, δ_j represents the error term for each OUTPUT PE. The weight adjustments for the INPUT and HIDDEN layers were realized by employing the chain rule and partial differential equations, where the weight change for an arbitrary number of layers was:

$$\frac{\partial E}{\partial v_{hi}} = \frac{\partial E}{\partial y_i} \frac{\partial y_i}{\partial r_i} \frac{\partial r_i}{\partial x_h} \frac{\partial x_h}{\partial v_i} = \sum_{l=1}^p (b_l - y_l) y_l w_{hl} f'(r_i) a_h \quad (5.4)$$

With these gradients established for the INPUT to HIDDEN and the HIDDEN to OUTPUT layers, in the backpropagation with momentum method, the adjustments of the weight connections were computed as:

$$w_{ij}^{new} = w_{ij}^{old} - \alpha \frac{\partial E}{\partial w_{ij}} + \lambda \Delta w_{ij}^{old} \quad (\text{between HIDDEN and OUTPUT layers}) \quad (5.5)$$

$$v_{hi}^{new} = v_{hi}^{old} - \beta \frac{\partial E}{\partial v_{hi}} + \lambda \Delta v_{hi}^{old} \quad (\text{between INPUT and HIDDEN layers}) \quad (5.6)$$

In the preceding equations, α , β are positive terms that were used to standardize the weight adjustments. These terms (α , β) are called the learning rates of the neural network and standard backpropagation assumes constant α , β terms. In this study, $\alpha=0.100$ and $\beta=0.100$. In the preceding equation, λ represents the momentum term in the backpropagation with momentum learning procedure. For this study, $\lambda=0.700$ for all simulations. The momentum learning was used to reduce the sensitivity of the network to small features in the error surface.

5.4.2. Conjugate Gradient algorithm

The conjugate gradient algorithm was also used for minimizing the cost function in neural network training. In contrast to the aforementioned backpropagation and Levenberg-Marquardt learning algorithms, the conjugate gradient method utilized a variable learning rate. From a mathematical standpoint, it is closely associated with the backpropagation method that utilizes the method of steepest descent. The authors in [84] have given a thorough explanation of the method and it will be provided here for reference. To succinctly describe the method, one can envision that there is an initial guess for the minimum value w_0 through a search direction:

$$s_o = -\frac{\partial E}{\partial w_0} = -g_0 \quad (5.7)$$

Approximations of w_k were generated in an effort to minimize the error function, E , as follows:

- 1) For $k=0$ to 1, computation was initiated at point w_k and a line minimization of E was performed in the direction s_k
- 2) The scalar function α_k was determined such that the function $J(\alpha) = E(w_k + \alpha s_k)$ was minimized (J was expressed as a function of the learning rate α for fixed values of w and s).

The updated estimate of w is given as:

$$w_{k+1} = w_k + \alpha_k s_k \quad (5.8)$$

The next step in this algorithm was the selection of a new conjugate search direction. In terms of numerical stability, the Polak and Ribiere method proven by Haykin in [90] has been suggested for updating the search direction according to:

$$s_{k+1} = -\nabla E(w_{k+1}) + \beta_{k+1} s_k$$

In the preceding equation, $\beta_{k+1} = -\frac{s_{k+1}^T (s_{k+1} - s_k)}{s_k^T s_k}$.

Utilizing the expressions for w_{k+1} and s_{k+1} from above led to an expression for the variable learning rate α_k .

5.5. Material Degradation due to Fatigue

5.5.1. Elastic Modulus Degradation

The elastic modulus was measured on samples as a function of strain up to 1% strain. This was considered the extent of the elastic region [13]. Changes in elastic modulus due to thermal and/or mechanical cycling served to illuminate the accumulation of damage in a material, as described in Basaran et al. [108]. Using elastic modulus degradation as a damage metric is very established in the mechanics community [119-120]. The elastic modulus degradation metric was quantified as:

$$D = 1 - \frac{E_i}{E_0} \quad (5.9)$$

In this equation, D is the damage state variable, E_0 is the initial elastic modulus, and E_i is the elastic modulus at any point. At the initiation of the test $D=0$ and for ultimate failure $D=1$.

5.5.2. Inelastic strain

Inelastic strain can be considered as any component of strain that is not recoverable as a result of the fatigue loading process. In effect, inelastic strains occurred due to irreversible processes from the standpoint of thermodynamics. This has been

established from the Clausius-Duhem inequality of thermodynamics, in which creep processes and plastic strains engendered irreversible changes to the material microstructure. Inelastic strains occurred as a result of the creep process due to constant amplitude fatigue loading or as a result of plastic strains that were engendered due to loading above the yield point of the material. There have been several researchers that consider inelastic strains as a damage evolution criterion [118-120]. In this manuscript, the inelastic strains occurred primarily due to the creep process from constant stress fatigue loading. In terms of creep that evolved during the fatigue process, the residual strain that remained in the sample was a component of the strain parameter represented through a Volterra equation. The total creep strain evolution was given as:

$$\varepsilon(t) = \frac{\sigma(t)}{E} + \int_0^t K(t-t') \dot{\sigma}(t') dt' \quad (5.10)$$

\downarrow
 Instantaneous
creep

\downarrow
 Creep evolution
over time

In this equation, $\varepsilon(t)$ represents the strain evolution as a function of time, $\dot{\sigma}(t)$ is the stress rate function (which possesses constant amplitude in the case of constant stress fatigue loading), E is the instantaneous elastic modulus, and K is the compliance function. In the case of fatigue loading conditions, the Volterra relationship had to be expanded to account for the sinusoidal response of the stress and strain functions. A generalized parameter denoted for the time varying functions in the preceding equation to account for sinusoidal loading conditions is:

$$X(t) \Rightarrow X(t) \sin \omega t \quad (5.11)$$

Here, the generalized $X(t)$ function is used to represent the sinusoidal time varying behavior of the stress, strain, and compliance functions. Since the problem prescribed in this manuscript relates to constant stress fatigue loading, the stress function was given as:

$$\sigma(t) \Rightarrow \sigma_A \sin \omega t \quad (5.12)$$

Here, σ_A represents the amplitude of the stress function during fatigue loading.

Most of the samples tested in this study experienced nonlinear viscoelastic fatigue conditions, as evidenced by the fact that more than the elastic portion of strain remained in the sample subsequent to fatigue loading. Because of this, the Volterra creep function could not be decoupled into instantaneous and evolution strains. In this case, the residual strain was measured as a fraction of the entire strain evolution parameter, as:

$$\varepsilon_R = \xi \left\{ \frac{\sigma_0}{E} + \int_0^t K(t-\tau) \dot{\sigma}(\tau) d\tau \right\} \quad (5.13)$$

Here, ξ is a parameter that was defined in the interval $0 \leq \xi < 1$, and was a representative fraction of the creep strain that remained in the sample subsequent to unloading. The form of equation (5.13) is that of a Volterra function, which is normally used to describe the creep behavior of polymeric materials subjected to constant stress loading conditions [21]. In (5.13), $\dot{\sigma}(\tau)$ actually represents the sinusoidal stress (which varies between the minimum and maximum stress for this problem and leads the strain by an angle δ), E represents the initial elastic modulus, $K(t-\tau)$ represents the creep compliance function that evolved over time, and ξ is a factor that denotes the portion of the creep strain evolution that was retained subsequent to fatigue loading.

The residual strain parameter was implemented into the neural network architecture as an input for prediction of the residual strength mechanical properties of

the PET and PET-VGCNF fibers subsequent to fatigue loading. An example schematic of the creep process that occurred during fatigue is shown in Figure 5.2, where actual data is displayed for the strain amplitude and corresponding residual strain for a test specimen that underwent 5,000 prior cycles. In Figure 5.2, there was an instantaneous creep $\varepsilon(t_0)$ followed by a steady creep evolution up to $(\varepsilon(t_f))$, then strain unloading to zero stress with an ensuing residual strain (ε_R).

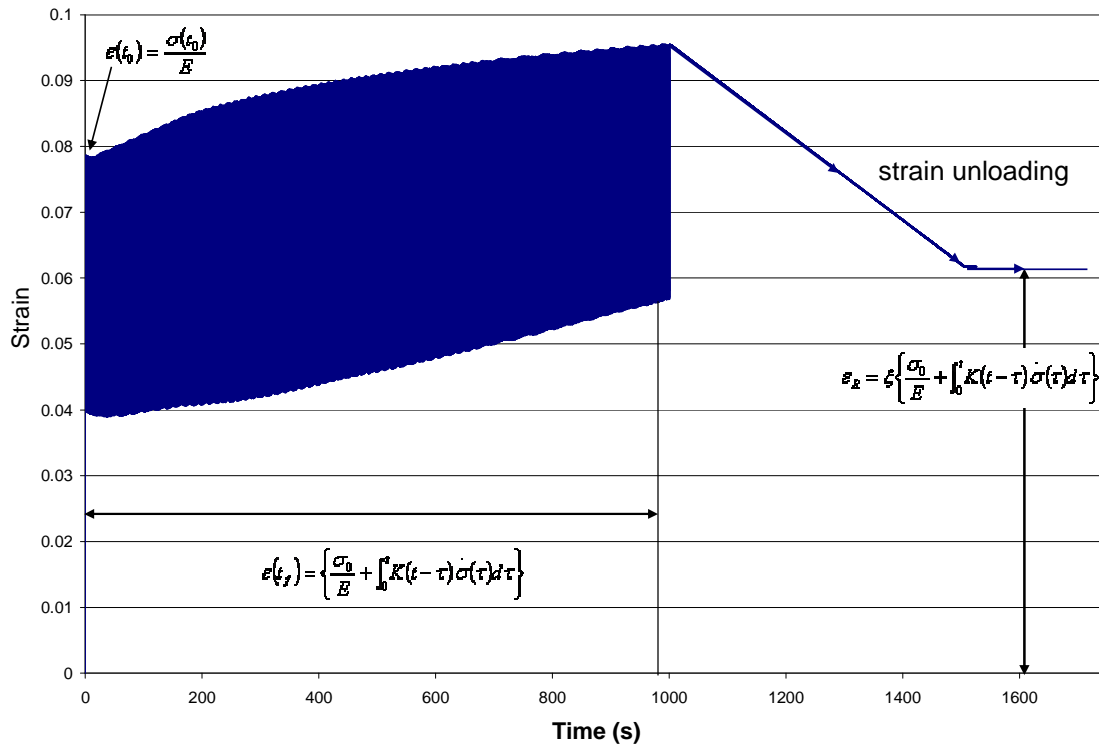


Figure 5.2. Example strain amplitude vs. time for specimen that underwent 5,000 cycles illustrating the creep evolution and retention of strain

5.5.3. Neural Network Architecture for Prediction of Residual Mechanical Properties - PET Control Samples

For the PET unreinforced samples, the input vector for the ANN was defined considering the following:

$$X = \{R \ \sigma_{\max} \ E \ \varepsilon_R\}^T \quad (5.14)$$

Here, R , σ_{\max} , E , and ε_R are all scalar variables that represent the stress ratio, the maximum stress during fatigue cycling, the undeformed elastic modulus, and the residual viscoelastic creep strain, respectively. Notice from this input vector that the number of cycles, N , was omitted from the choice of variables for PET unreinforced samples. In the experimental tests, N was defined in the range $1000 \leq N \leq 389,000$, although the variable was omitted from the computational simulations. The reason that N was omitted from the input vector for residual property predictions for PET unreinforced samples was because there was a huge amount of scatter observed in the data for prediction of the residual strength and elastic modulus degradation. Thus when the ANN computations were performed with the inclusion of the number of cycles, the network synaptic weights were adjusted and virtually assigned zero contribution to the input variable N . The fatigue tests were conducted at various minimum and maximum stress levels and load ratios for both PET control and PET-VGCNF samples. Stress ratios of $R=0$ and $R=1/3$ were used to conduct the fatigue tests on the PET control samples and values corresponding to the interval $0.25\sigma_f \leq \sigma_{\max} \leq 0.60\sigma_f$ were used for the maximum stress variations. The elastic modulus, E , was a value that corresponded to either the PET control or PET-VGCNF undeformed modulus. Residual viscoelastic creep strain values, as determined by the method shown in Figure 5.2, were in the range $0 \leq \varepsilon_R \leq 0.23$. An example schematic of the network used to predict the residual strength ($\sigma_f'(X)$) and the elastic modulus degradation ($D(X)$) of the PET control sample is shown in Figure 5.3.

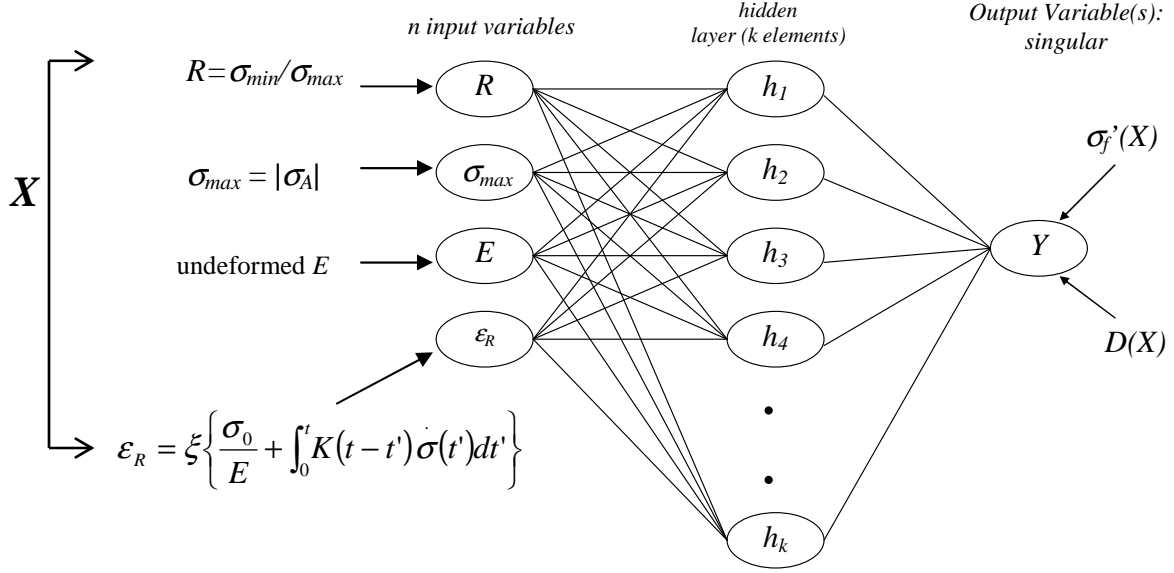


Figure 5.3. Schematic of ANN architecture used for prediction of residual mechanical properties in PET control samples

5.5.4. Neural Network Architecture for Prediction of Residual Mechanical Properties – PET-VGCNF Samples

For the PET-VGCNF samples, the input vector for the ANN was defined considering the following:

$$X = \{R \ \sigma_{max} \ N \ E \ \varepsilon_R\}^T \quad (5.15)$$

In this vector, the other variables have been prescribed in 5.5.3, with the exception of N , which represents the number of fatigue cycles. Stress ratios of $R=0$, $R=1/3$, and $R=2/3$ were used to conduct the fatigue tests on the PET-VGCNF samples and values corresponding to the interval $0.34\sigma_f \leq \sigma_{max} \leq 0.60\sigma_f$ were used for the maximum stress variations. The number of fatigue cycles performed on the PET-VGCNF samples was $1000 \leq N \leq 1.25E6$. As with the PET control samples, residual viscoelastic creep strain values, as determined by the method shown in Figure 5.2, were in the range $0 \leq \varepsilon_R \leq 0.16$.

5.6. Results and Discussion

5.6.1. *Results From Training and Testing Procedures*

The results of the neural network performance indicate that both the backpropagation with momentum and conjugate gradient training algorithms were successful at depicting the residual strength degradation as a function of the mechanical testing conditions and the residual strain parameter. Shown in Tables 5.1 and 5.2 are the numerical results from the training results and testing of networks for PET and PET-VGCNF samples that underwent fatigue conditions for $R=0$ at a maximum stress of 60% of the failure stress. The mean-squared error (MSE) cost function was utilized to evaluate the efficiency of the network. The datasets were randomized and three trials were run to evaluate the network performance. For the PET control samples, implementation of the BP with momentum algorithm engendered an average final MSE of 0.01309, an average number of processing elements (PE) in the hidden layer equal to 5, and an average linear correlation coefficient, r , equal to 0.8663. Implementation of the conjugate gradient method to train the network resulted in a lower average MSE of 0.007187, an average number of PEs equal to 5, and an average linear correlation coefficient equal to 0.7617. These data show that while the conjugate gradient algorithm was more efficient at driving out the error between the computed and actual signals, it was not as efficient at representing the data from a new testing data set. The results from the training and testing of the ANN for the residual property prediction of PET-VGCNF samples fatigued at 60% of the failure stress indicated a similar pattern to the PET control samples. The main difference is that, on average, for both the BP with momentum and

the conjugate gradient algorithms, the number of hidden PEs necessary for computation was 6.

The results from the experimental and ANN prediction of the modulus degradation metric subsequent to fatigue are given in Tables 5.3-5.4. As with the fracture strength data, the modulus degradation results indicate a strengthening effect in the low residual strain limit for the PET samples and increases in the modulus degradation thereafter. For the PET-VGCNF samples, the elastic modulus degradation increased with increasing residual strains. The performance results from the training and testing experiments are shown in Tables 5.3 and 5.4. From the performance results in Tables 5.3 and 5.4, the conjugate gradient algorithm was more efficient than the BP algorithm in reducing final MSE for a time series of 1000 epochs. The average final MSE was 0.008751 and 0.008691 for the PET control and PET-VGCNF samples conducted at 60% of the fracture stress under $R=0$ conditions, respectively. In addition, the average correlation coefficient, r , was greater for data replication utilizing the conjugate gradient method for both the PET control and PET-VGCNF samples. The synaptic weights obtained from the training and testing results provided in Tables 5.1-5.4 were stored in a database file and later used to determine the mechanical properties subsequent to fatigue based on other loading conditions, as will be described later.

Table 5.1. Nondimensional residual strength ANN performance data for PET Control samples, $R=0$, $\sigma_{max}=0.6\sigma_f$

<i>MLP-Backpropagation with momentum</i>				<i>MLP-Conjugate gradient</i>			
	Training results		Testing results		Training results		Testing results
Randomized trials	Final MSE	Best network # PEs	r	Randomized trials	Final MSE	Best network # PEs	r
Trial 1	0.01543	6	0.8725	Trial 1	0.007922	5	0.8469
Trial 2	0.01080	4	0.8739	Trial 2	0.008050	5	0.6709
Trial 3	0.01304	6	0.8525	Trial 3	0.005590	5	0.7671
Average	0.01309	5	0.8663	Average	0.007187	5	0.7616
Std. Dev.	0.002312	1	0.01197	Std. Dev.	0.001385	0	0.08814

Table 5.2. Nondimensional residual strength ANN performance data for PET-VGCNF samples, $R=0$, $\sigma_{max}=0.6\sigma_f$

<i>MLP-Backpropagation with momentum</i>				<i>MLP-Conjugate gradient</i>			
	Training results		Testing results		Training results		Testing results
Randomized trials	Final MSE	Best network # PEs	r	Randomized trials	Final MSE	Best network # PEs	r
Trial 1	0.01200	6	0.8401	Trial 1	0.006043	6	0.8136
Trial 2	0.01451	5	0.8774	Trial 2	0.009026	6	0.7339
Trial 3	0.01070	6	0.8735	Trial 3	0.008422	5	0.8739
Average	0.012403	6	0.8637	Average	0.007831	6	0.8071
Std. Dev.	0.001936	0.6	0.02050	Std. Dev.	0.001577	0.6	0.07021

Table 5.3. Elastic modulus degradation ANN performance data for PET control samples,
 $R=0, \sigma_{max}=0.6\sigma_f$

<i>MLP-Backpropagation with momentum</i>				<i>MLP-Conjugate gradient</i>			
	Training results		Testing results		Training results		Testing results
Randomized trials	Final MSE	Best network # PEs	r	Randomized trials	Final MSE	Best network # PEs	r
Trial 1	0.01209	6	0.9057	Trial 1	0.009215	5	0.8401
Trial 2	0.01053	6	0.6891	Trial 2	0.009012	4	0.7883
Trial 3	0.01030	5	0.6496	Trial 3	0.008025	6	0.7155
Average	0.01097	6	0.7481	Average	0.008751	5	0.7813
Std. Dev.	0.0009745	0.6	0.1379	Std. Dev.	0.0006366	1	0.06258

Table 5.4. Elastic modulus degradation ANN performance data for PET-VGCNF samples, $R=0, \sigma_{max}=0.6\sigma_f$

<i>MLP-Backpropagation with momentum</i>				<i>MLP-Conjugate gradient</i>			
	Training results		Testing results		Training results		Testing results
Randomized trials	Final MSE	Best network # PEs	r	Randomized trials	Final MSE	Best network # PEs	r
Trial 1	0.01178	4	0.7890	Trial 1	0.009045	5	0.8464
Trial 2	0.01417	5	0.8565	Trial 2	0.007979	6	0.7576
Trial 3	0.01008	5	0.6440	Trial 3	0.009404	5	0.8649
Average	0.01201	6	0.7632	Average	0.008691	6	0.8113
Std. Dev.	0.002055	0.6	0.1086	Std. Dev.	0.001007	0.7	0.07591

5.6.2. Residual Strength as a Function of Number of Cycles and residual strain – PET Control

Figure 5.4 displays some graphical results of the ANN simulations for unreinforced and nanocomposite fiber samples tested under $R=0$ loading conditions at a maximum stress equal to 60% of the fracture stress. Nondimensional residual fracture strength is represented as a function of residual strain and # of cycles in Figure 5.4 for the

PET control sample. This 3-D visualization delineates how the number of fatigue cycles did not have a significant effect on the residual strength of the PET control samples.

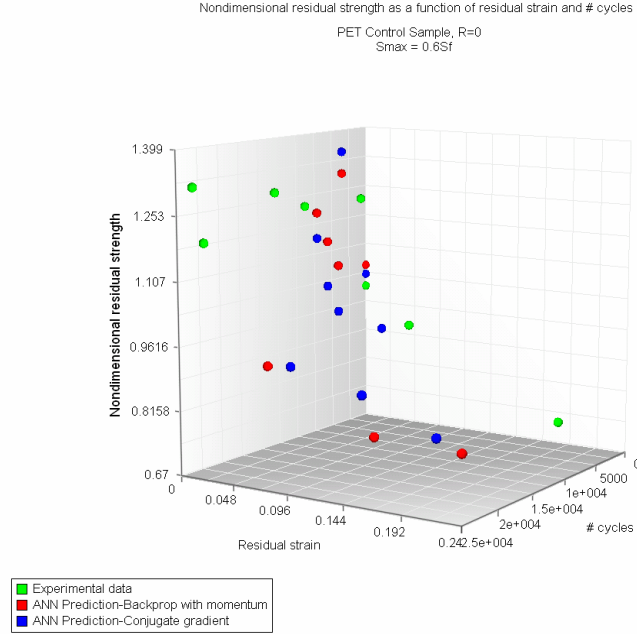


Figure 5.4. PET control sample under R=0 conditions: 3-D schematic illustrating the nondimensional residual strength as a function of the number of cycles (N), and the residual strain (ϵ_R)

For the PET control sample, the results in Figure 5.4 indicate that the residual strength was increased in the low residual strain limit and then degraded with the residual strain strongly, while there was no dependency on the number of prior fatigue cycles. This is seen by the scatter in the residual strength with the number of cycles on Figure 5.4. A curve fit from the MLP network trained via BP with momentum and conjugate gradient algorithms is also provided to indicate how the modeling procedures were not able to correctly identify the relationship of the residual strength with the number of cycles. As mentioned previously, the number of cycles was omitted from the training and testing procedure to enhance the predictability of the network. To further corroborate this finding, a sensitivity analysis was performed on the data and the results shown in Figure

5.5 indicate that N was the parameter that least affected the residual strength when all the other input variables remained constant. For the PET control samples tested under fatigue conditions, the reason for the weak dependence on the number of fatigue cycles can be likely explained by considering that flaws of various and random sizes existed in the samples prior to fatigue testing. The randomness and scatter of the residual strength has been heavily investigated by researchers utilizing Weibull statistics to study how the fracture strength is strongly affected by the “weakest link” (largest flaw) [138-141].

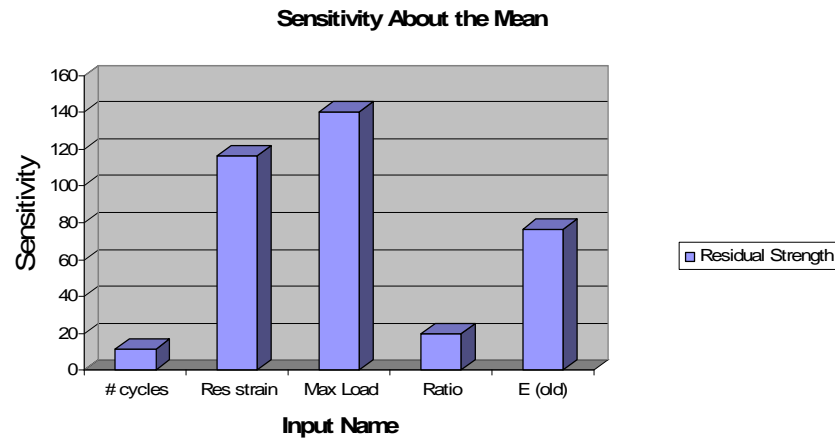


Figure 5.5. Sensitivity analysis indicating the weak dependence of the residual strength on the number of cycles

5.6.3. Residual Strength as a Function of Number of Cycles and residual strain – PET-VGCNF

There was a difference in mechanical behavior for the PET-VGCNF with comparison to the PET control samples subsequent to fatigue loading. Figure 5.6 shows the nondimensional residual strength as a function of the residual strain and the number of prior fatigue cycles for a PET-VGCNF sample under $R=0$ conditions. The results do not indicate a strengthening effect in the low cycle and low residual strain limit, in contrast to the PET samples. In addition, the PET-VGCNF samples exhibited a stronger

residual strength degradation dependency on the number of cycles than the PET samples, indicating that further cycling causes more microdefects and failure sites to occur. This has been corroborated with SEM fractographs of the samples tested under fatigue conditions, where defibrillation and decohesion were noticed in the nanocomposite PET-VGCNF samples for small residual strains and a small number of cycles (Chapter 4). Figure 5.6 displays the nondimensional residual strength as a function of the residual strain and includes the results from the ANN simulation procedure. Both the BP with momentum and the conjugate gradient based algorithms were successful at reproducing the experimental results from the fatigue tests. As can be seen from Figure 5.6, for the PET-VGCNF samples there was an “s-shaped” dependency of the residual strength on the number of cycles and residual strain parameters, where the residual strength degraded with residual strain and on the number of fatigue cycles, N .

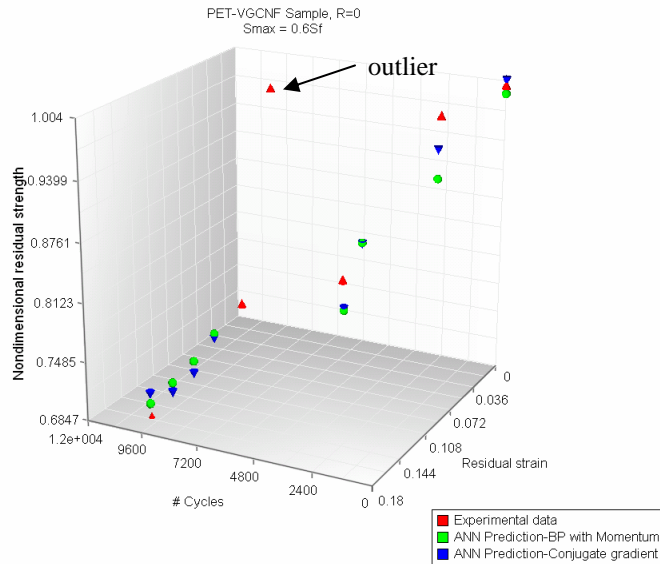


Figure 5.6. PET-VGCNF sample, R=0 conditions: 3-D schematic illustrating the nondimensional residual strength as a function of the number of cycles (N), and the residual strain (ϵ_R)

5.6.4. *Mechanical Property Predictions of PET and PET-VGCNF Fibers Subsequent to Fatigue Loading as a Function of Residual Strain*

Plots were generated to illustrate the effectiveness of the ANN computations at capturing the dependency of the residual mechanical properties on the residual strain parameter. Production data were generated using the model obtained from the training and testing procedures, provided in Tables 5.1-5.4. Figures 5.7-5.8 indicate both experimental and production data results for PET control and PET-VGCNF samples at a stress ratio of $R=0$ and a maximum stress equal to 60% of the fracture stress. For the PET control sample, Figure 5.7 shows that both the BP with momentum and conjugate gradient algorithms were both successful at replicating the experimental trends of the residual strength and elastic modulus degradation and capturing the strain hardening effects in the lower residual strain limits. In the case of elastic modulus degradation, the BP with momentum algorithm was slightly better at representing the strain hardening effect from the actual data, since the conjugate gradient network slightly underestimated the data at low residual strains. For this loading condition, both ANN algorithms slightly overestimated the elastic modulus degradation between the interval $0.025 < \epsilon_R < 0.24$.

Figure 5.8 shows experimental and ANN production data results for the residual strength and elastic modulus degradation as a function of residual strain for $R=0$ and $\sigma_{max}=0.6\sigma_f$ for PET-VGCNF samples. The residual strength degradation was represented well by both training algorithms. However, for the elastic modulus degradation, the conjugate gradient based procedure was slightly better at replicating the data. The BP with momentum based algorithm exhibited a similar trend to that of the conjugate gradient; however, there was a slight overestimation of the elastic modulus degradation using this procedure (as shown in Figure 5.8).

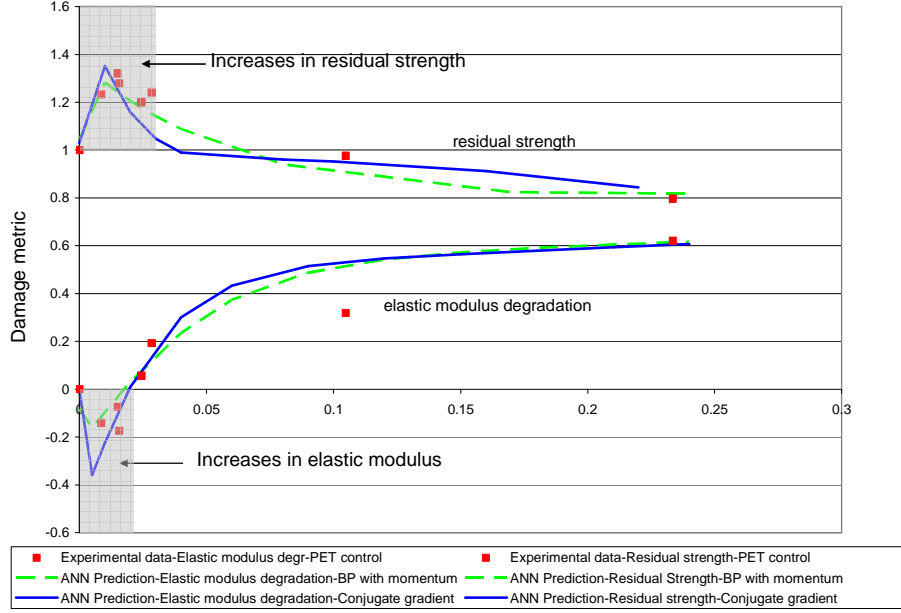


Figure 5.7. PET control sample ($R=0$, $\sigma_{max}=0.6\sigma_f$): Actual experimental results and ANN production data sets (BP with momentum and conjugate gradient) of nondimensional residual modulus vs. the residual strain

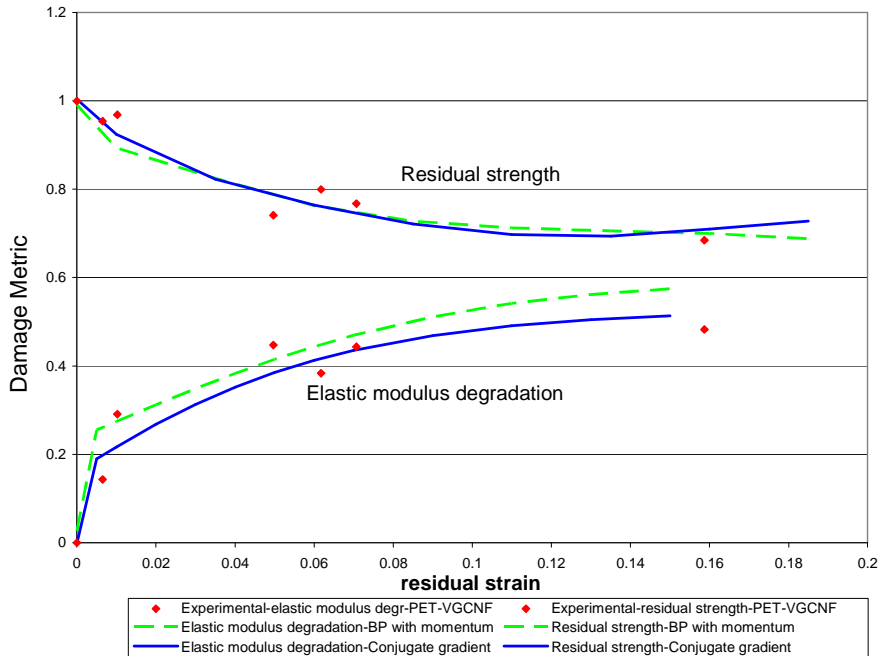


Figure 5.8. PET-VGCNF sample ($R=0$, $\sigma_{max}=0.6\sigma_f$): Actual experimental results and ANN production data sets (BP with momentum and conjugate gradient) of nondimensional residual modulus vs. the residual strain

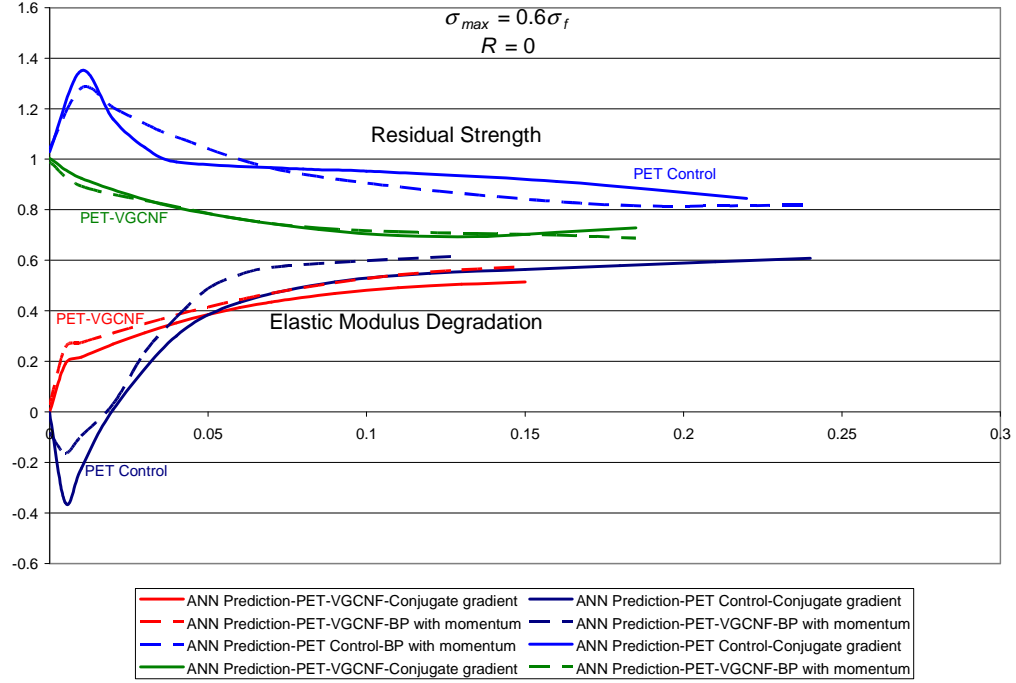


Figure 5.9. Comparison of the mechanical behavior of PET control and PET-VGCNF samples subsequent to fatigue loading utilizing ANN predictions based on BP with momentum and conjugate gradient algorithms

To better assess the differences in mechanical behavior as a function of the residual strain, the results from the ANN computations at $R=0$ and $\sigma_{max}=0.6\sigma_f$ were plotted on the same graph. The results from the simulations indicate that the PET control samples retain strength slightly better than the 5 wt% nanocomposite counterparts when subjected to fatigue stresses with the retention of creep strains. Further, as stated earlier, the results show that the nanocomposite samples exhibited residual strength and elastic modulus degradation readily with the retention of creep strains. The results also show that although the PET control samples exhibit strain hardening in the form of modulus increases in the low residual strain limit, the rate of degradation is noticeably higher than that for PET control samples subsequent to this hardening, indicating that the aligned chains experienced a greater loss in stiffness immediately after the low residual strain

limit. These results are in sync with results from the literature, where PET control samples have been shown to exhibit distinct hardening effects in the early stages of fatigue at room temperature [27]. The authors in [27] have conducted thermoluminescence studies on PET filaments and concluded that the cyclic extensions in the early stages of fatigue engender distinct hardening effects and that the strain hardening decreases with the increasing number of repeat extensions. The effect of defects was shown to be present at later stages during the fatigue process, where further cycling increased the possibility of the introduction of defects. Although many studies have not been conducted on the mechanical behavior of nanocomposite materials subjected to fatigue, results from the literature on composite materials support the claim that the nanocomposite fibers suffered mechanical strength and residual strength degradations due to repeated cycling [142-143]. Decreases in residual strength for composite materials under fatigue loading, as seen in Figures 5.8 and 5.9 for the PET-VGCNF samples tested in this study, can be also explained by the poor adhesion between the matrix and reinforcing agent. In the literature, this is evidenced through computational calculations of the critical shear stress required for debonding [144-145] and SEM fractography where pull-out and debond sites are seen at high magnifications [146-147]. In the case of this study, a separate and detailed SEM study was conducted to determine the primary mode of failure in PET-VGCNF samples loaded under fatigue conditions (see Chapter 4). The primary mode of failure was defibrillation and debonding of the VGCNF from the PET matrix after cycling and accumulation of strains. Results from the literature also support the losses in modulus degradation of the PET-VGCNF samples subjected to fatigue loading [148].

5.7. Comparison of the Residual Mechanical Properties of PET Control and PET-VGCNF Fibers Under Various Loading Configurations

From the results of the BP with momentum and conjugate gradient based training procedures, the best networks were used to model the residual strength degradation and elastic modulus degradation under other various loading configurations so that comparisons could be made between the mechanical behavior of PET control and PET-VGCNF samples. Shown in Figure 5.10 is a comparison of the residual strength and elastic modulus degradation between PET control and PET-VGCNF samples as a function of the residual creep strain for stress ratios $R=0$ and $R=0.333$ at a maximum stress equal to 60% of σ_f . These results indicate that, in most cases, both the residual strength and elastic modulus degradation were highly dependent upon the maximum fatigue stress amplitude. For PET control samples, the results for the $R=0$ configuration demonstrate the aforementioned residual strength and elastic modulus hardening in the low residual strain limit (up to 1% for the residual strength and up to 0.5% for the elastic modulus degradation). For the $R=0.333$ loading configuration, the results varied. The results in Figure 5.10 also indicate an increase of the residual strength in the low residual strain limit in excess of that for the $R=0$ configuration for the PET control samples; however, the elastic modulus experienced no hardening in the low residual strain limit. This is likely due to the lower strain amplitude that the samples were exposed to during cycling (with respect to the $R=0$ configuration), which engendered little or no orientation of the polymer chains along the fiber axis. The average strain amplitude of the PET control samples at the $R=0$ configurations was approximately 0.038, while the strain amplitude was 0.016 for the $R=0$ loading configuration.

For the PET-VGCNF samples, the results varied as well. For the residual strength, the results in Figure 5.10 indicate the aforementioned dependency of the residual strength on the residual strain for the R=0 loading configuration (maximum stress equal to 60% of σ_f). However, when the stress ratio was increased to R=0.333, the model results indicated little to no dependency of the residual strength on the residual strain. As with the results from the PET samples, this low decline in residual strength up to 10% strain is likely due to the lower strain amplitude that the samples were exposed to during cycling. For the R=0 loading configuration, the PET-VGCNF samples were exposed to average strains with an amplitude of 0.030 in comparison to average strain amplitudes of 0.013 for the R=0.333 loading configuration.

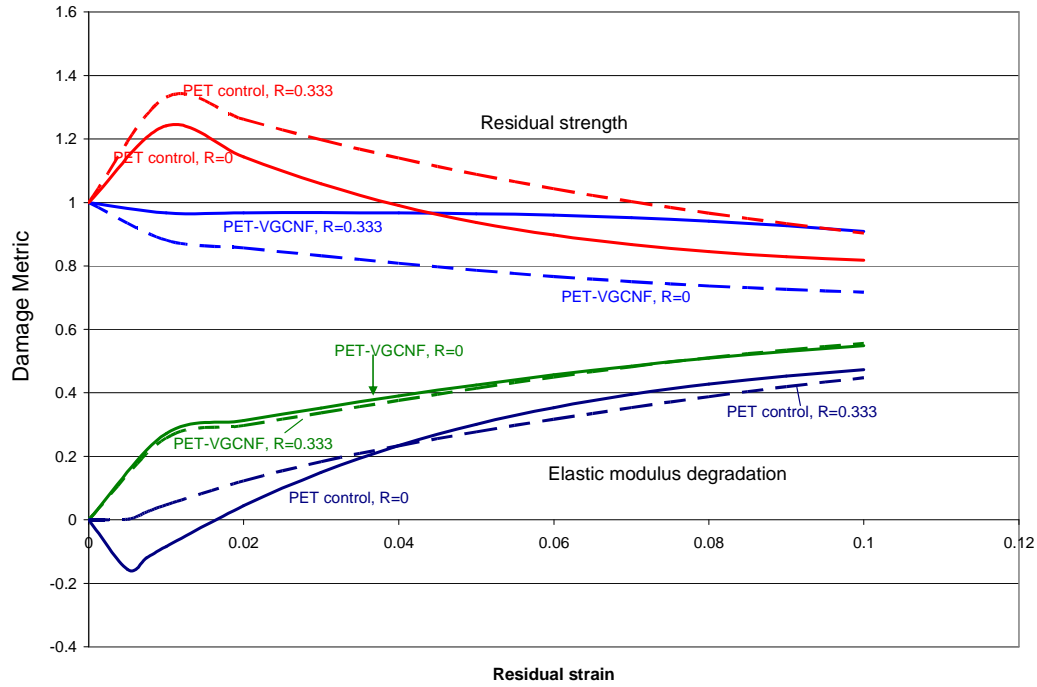


Figure 5.10. Residual strength and elastic modulus degradation predictions of PET control and PET-VGCNF as a function of residual strain for R=0 and R=0.333 stress ratios ($\sigma_{max} = 0.6\sigma_f$) utilizing MLP ANN architecture and BP with momentum training algorithm

The MLP with BP based scheme was also utilized to model the effects of maximum fatigue stress on the residual mechanical properties. The results are provided in Figures 5.11 and 5.12. The results show that the elastic modulus and residual strength of both PET control and PET-VGCNF samples both depend on the maximum fatigue stress during fatigue loading. A family of curves was generated for elastic modulus degradation and residual strength as a function of maximum fatigue stress for residual strains in the low limit ($\epsilon_R=0.01$), median residual strain limit ($\epsilon_R=0.05$ and $\epsilon_R=0.10$) and upper residual strain limit ($\epsilon_R=0.15$). For the PET control samples in the low residual strain limit ($\epsilon_R=0.01$), the results indicate that both the residual strength and elastic modulus were not strongly affected by increasing the maximum stress up to approximately 30% of the fracture stress; in actuality, both the residual strength and elastic modulus values increased after 30% of the maximum fatigue stress (hardening effect). For the other residual strain configurations ($\epsilon_R=0.05$, $\epsilon_R=0.10$, and $\epsilon_R=0.15$), the results indicate a degradation of both the residual strength and elastic modulus up to approximately 30% of the fracture stress, then a change in slope for both properties as function of maximum fatigue stress (increasing slope for residual strength and decreasing slope for elastic modulus). These results are consistent with the results from the experimental regimen.

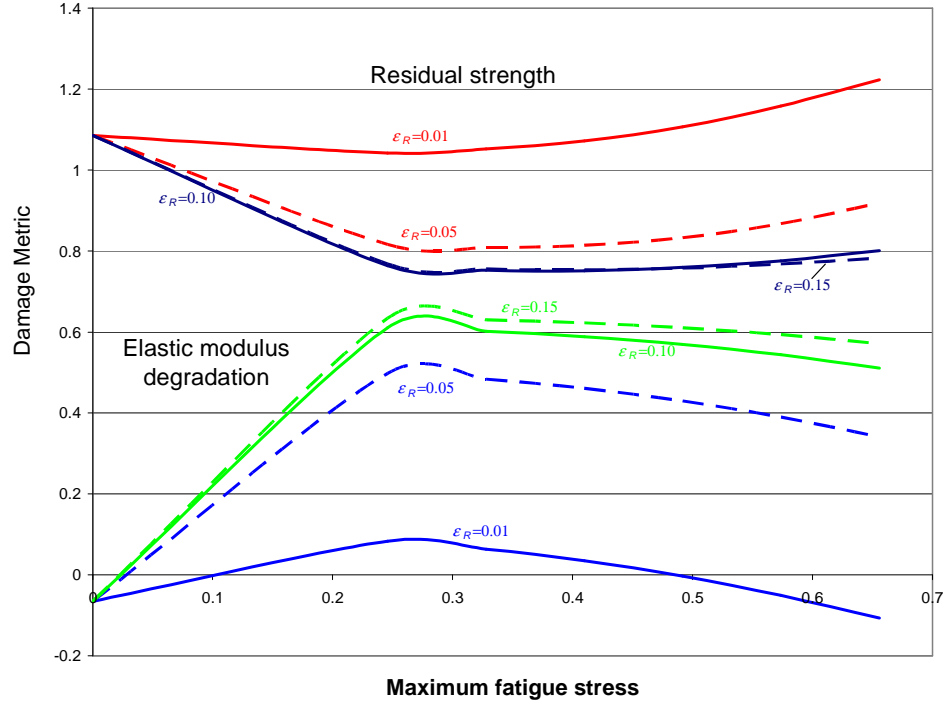


Figure 5.11. Residual strength and elastic modulus degradation predictions of PET control samples at various residual strains ($\epsilon_R = 0.01$, $\epsilon_R = 0.05$, $\epsilon_R = 0.10$, $\epsilon_R = 0.15$) utilizing ANNs with BP with momentum training scheme

The residual properties of PET-VGCNF samples at residual strains $\epsilon_R = 0.01$, $\epsilon_R = 0.05$, $\epsilon_R = 0.10$, $\epsilon_R = 0.15$ displayed a similar trend to those of the PET control sample (Figure 5.12). The results indicate a declining residual strength and elastic modulus up to a certain percentage of the maximum fatigue stress, then a change in slope. The results of Figure 5.12 indicate an exacerbation effect of the maximum fatigue stress on the residual mechanical properties for increasing residual strains. As shown in Figure 5.12, higher residual strains ($\epsilon_R = 0.10$ and $\epsilon_R = 0.15$) induced by the same maximum fatigue stress engendered greater losses in residual strength and elastic modulus. In comparison to the PET control samples, the residual strength behavior was the same as a function of maximum fatigue stress and residual strain; however, the elastic modulus displayed a

plateau behavior at a certain maximum fatigue stress value, as indicated by the “plateau spine” in Figure 5.12.

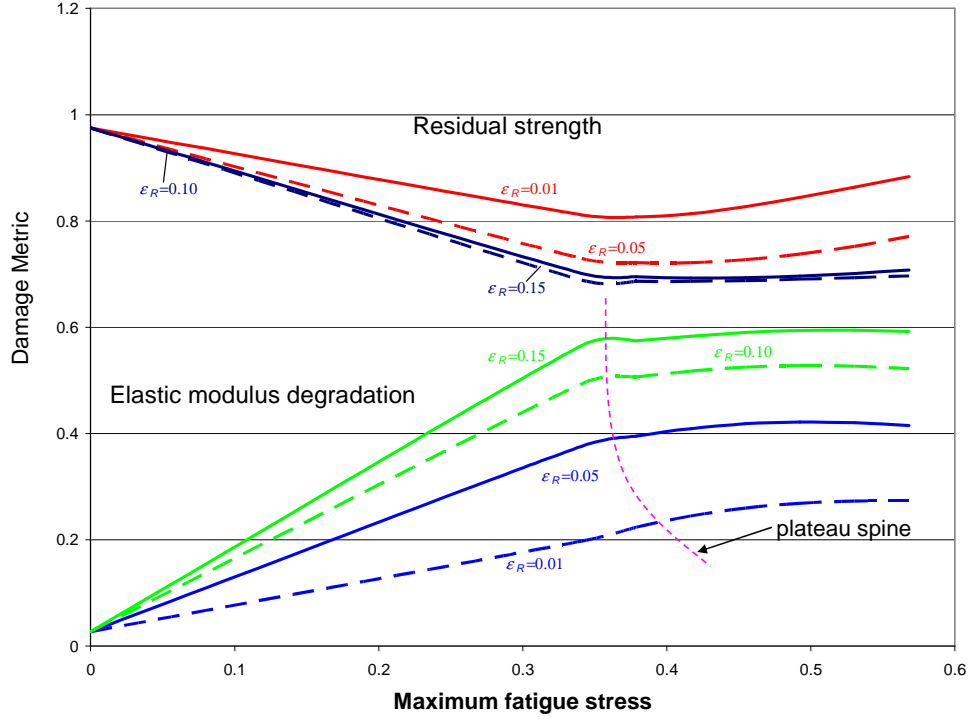


Figure 5.12. Residual strength and elastic modulus degradation predictions of PET-VGCNF fibers at various residual strains ($\epsilon_R = 0.01$, $\epsilon_R = 0.05$, $\epsilon_R = 0.10$, $\epsilon_R = 0.15$) utilizing ANNs with BP with momentum training scheme

Conclusions for Chapter 5

The results from this chapter indicate that artificial neural networks (ANNs) utilizing backpropagation with momentum and conjugate gradient learning algorithms can be used to predict the residual mechanical properties of PET and PET-VGCNF fibers subsequent to fatigue loading. The ANNs were successfully trained to replicate experimental data and the models were used to determine the dependence of the residual fracture strength on number of cycles (N), residual creep strain (ϵ_R), maximum fatigue stress (σ_{max}), and stress ratio (R). The experimental and computational results showed

that the residual mechanical properties of PET control samples exhibited a scattered and weak dependence on N . This was observed in the experimental data and computational sensitivity analysis, which indicated that N was not a strong factor in determining the residual mechanical properties of PET samples. The PET-VGCNF samples exhibited a stronger dependence on the number of cycles, and were thus included as an input variable into the ANN input vector set. The experimental and computational results also showed that the residual creep strain parameter (obtained as a fraction of the viscoelastic creep strain) strongly affected both the residual fracture strength and the elastic modulus. From a comparative standpoint, the experimental results showed that the PET control samples exhibited hardening effects in the low residual strain limit while the PET-VGCNF samples did not. These behaviors were captured well with the ANN computations. Increasing the stress ratio from $R=0$ to $R=0.333$ was shown to affect both the PET control and PET-VGCNF samples slightly, while both samples exhibited an exacerbation effect (higher degradation of both residual strength and elastic modulus) with increasing residual strain.

The results from this chapter could be particularly useful for designers and engineers that wish to employ polymeric fibers as constituent materials in composites exposed to fatigue loading. By using the experimental results and computational results from this chapter, one can determine the mechanical behavior of the fibers (residual strength and elastic modulus) as a function of input mechanical testing variables.

CHAPTER 6

PREDICTING THE MECHANICAL BEHAVIOR OF PET AND PET-VGCNF FIBERS SUBSEQUENT TO FATIGUE LOADING USING GENETIC ARTIFICIAL NEURAL NETWORKS

Summary of Chapter 6

The constitutive behavior of poly(ethylene terephthalate) (PET) unreinforced (control) and PET fibers reinforced with 5 wt% vapor-grown carbon nanofibers (VGCNFs) under uniaxial tension and subsequent to fatigue loading has been evaluated utilizing various analytical models. Two types of fatigue tests were performed: 1) Long cycle fatigue at 50 Hz (glassy fatigue) to evaluate fatigue resistance and 2) fatigue at 5 Hz (rubbery fatigue) to evaluate residual strength performance. The long cycle fatigue results at 50 Hz indicate that the PET-VGCNF samples exhibited an increased fatigue resistance of almost two orders of magnitude when compared to the PET unreinforced filaments. The results of the fatigue tests at 5 Hz indicate that the constitutive response of both the PET control and PET-VGCNF samples changed subsequent to fatigue loading. The uniaxial constitutive response of the PET and PET-VGCNF fibers was modeled utilizing genetic-algorithm (GA) based neural networks. The results showed that the uniaxial tension constitutive behavior of both PET unreinforced and PET-VGCNF samples with and without prior fatigue can be represented with good accuracy utilizing neural networks trained via genetic-based backpropagation algorithms, once the appropriate post-fatigue constitutive behavior is utilized. Experimental data of uniaxial tensile tests and experimental post-fatigue constitutive data have been implemented into the networks for adequate training. The uniaxial tensile tests were conducted at an elongation rate of 0.17 mm/s. The fatigue tests were conducted in tension-tension fatigue

with variations in the stress ratio (R), maximum stress (σ_{max}), number of cycles (N), and the residual creep strain (ϵ_r).

The scientific and engineering community could benefit tremendously from a predictive constitutive model that evaluates the stress state of the materials when subjected to fatigue loading. In essence, the constitutive prediction results could be of great utility to researchers and manufacturers that wish to evaluate the effects of fatigue loading parameters on the mechanical behavior and the residual properties of the material subjected to fatigue loading. The genetic based neural network evaluation is rigorous in the sense that vital information about the mechanical testing parameters is correlated with the state of the material at certain points during the fatigue test.

Specifically, in this research, uniaxial tensile experiments and stress controlled fatigue experiments were conducted on PET-VGCNF samples at room temperature to ascertain the effects of cycling on the mechanical behavior and constitutive response. It is understood from the fatigue experiments and the results from Chapters 4 and 5 that cycling under stress-controlled conditions caused a cyclic creep to occur in the samples with the retention of a permanent residual strain. Due to the retention of the strains, it is known from the literature on unreinforced PET samples that the molecular orientation changed [8]. Other studies have been conducted to assess the effects of drawing on the molecular orientation in PET samples [149]. The authors observed that the PET samples retained the molecular orientation below T_g (glassy state), while above T_g , the molecular chains possessed sufficient energy for relaxation. The extent of drawing polyethylene terephthalate samples below T_g produced some crystallinity as observed from the DSC

results. Figure 6.1 provides a depiction of results from Ward [21] that idealizes the amorphous polymer chain configurations subsequent to fatigue.

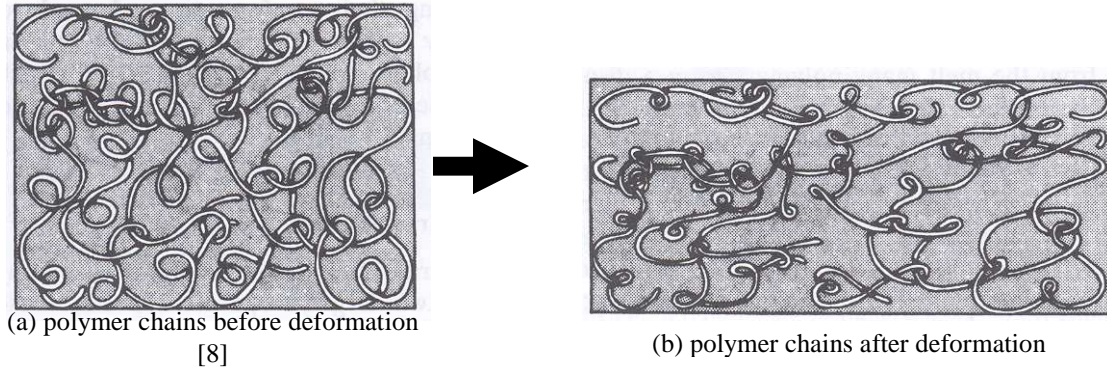


Figure 6.1. Schematics of (a) unoriented amorphous polymer chains and (b) oriented amorphous polymer chains [8]

With the inclusion of VGCNFs, the problem of constitutive behavior prediction becomes more complicated. Based on the results from this research, it is shown that cycling at a low frequency (5 Hz) in the rubbery regime changes the mechanical behavior (constitutive behavior) of the sample. Effects of the mechanical loading parameters and the residual creep strains have been used to assess how the mechanical properties changed based on the following input parameters: maximum stress (σ_{max}), stress ratio (R), number of cycles (N), and residual strain (ϵ_r).

6.1. Experimental

6.1.1. Sample Preparation and Mechanical Testing

The PET-VGCNF specimens were prepared and processed at the Georgia Institute of Technology as described in [128]. The details of the specimen preparation for the

mechanical testing paradigm are provided in [129]. The BOSE® ELeCtroForce® (ELF®) 3200 tensile and fatigue testing machine (Enduratec)) was used to conduct the mechanical experiments for uniaxial tension, uniaxial cyclic loading, and dynamic mechanical analysis (DMA). The uniaxial tensile tests were performed at an elongation rate of 10 mm/min and the fatigue tests were conducted at frequencies of 5 Hz and 50 Hz. Using the ELF 3200, DMA tests were conducted at various frequencies to determine the response of the phase lag component ($\tan \delta$) and stiffness of the sample as a function of frequency in the range 0.1 to 100Hz. All experiments were conducted at room temperature, laboratory air. The typical humidity of the laboratory air was about 50%.

6.1.2. Genetic neural network training

The process flow for the GA training scheme that was used in this research is shown in Figure 6.2.

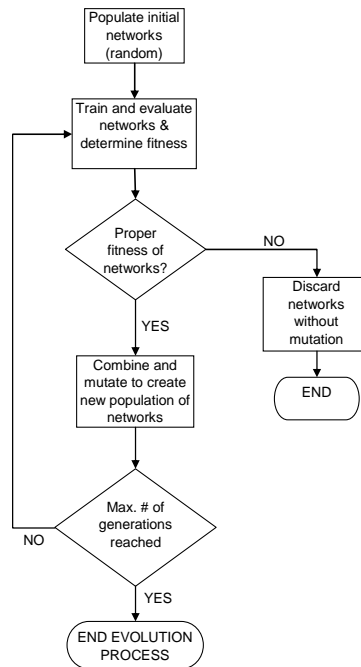


Figure 6.2. Process flow for Genetic Algorithm (GA) based training

Firstly, a random population of networks was created. Each of the networks in this population contained different parameters (input and network parameters). The networks were then trained using backpropagation with momentum or conjugate gradient and evaluated to determine their fitness (see [85] for description on backpropagation algorithms). In GA based training, the fitness corresponds to the lowest mean-squared error (MSE) of all the networks within a corresponding generation. The network weights were saved into a database for later retrieval during testing of the neural network and later for production datasets (see Appendix C for example). If the fitness of the networks did not meet the MSE requirement, they were not selected for mutation/reproduction. Proper fitness of the networks and selection can be performed using a variety of techniques, to include roulette, tournament, top percent, best, or random.

In conventional GA training, the combination of parameters can be performed via crossover, which can either be one-point, two-point, three-point, or n-point crossover. For the current research, one-point crossover was performed. In one-point crossover, a crossover point was randomly selected within a chromosome and was then interchanged with two parent chromosomes at this point to produce two new offspring. An example of the one-point crossover method using binary data is [99]:

Parent 1: 11001|010

Parent 2: 00100|111

Subsequent to the exchange of the parent chromosomes at the crossover point, the following offspring are produced:

Offspring 1: 11001|111

Offspring 2: 00100|010

The crossover probability was set to 0.9 in all experiments. After combination (crossover), mutation occurred in which one or more gene values in a chromosome was altered from its initial state. This operation resulted in new gene value creation, allowing the genetic algorithm to arrive at better solutions than previously possible. Mutation is an imperative step in the genetic search, because it decreases the chance of the network population stagnating at local optima. The mutation operation occurs during evolution according to a user-definable mutation probability. In this research, the mutation probability was set at a low value of 0.01 for optimal results. Other parameters that were used during the genetic computations relate to the step size optimization and the momentum rate optimization for the backpropagation algorithms. Table 6.1 prescribes the upper and lower bound values for these parameters.

Table 6.1. Upper and lower bound properties of step size, momentum, and PE element optimization parameters for genetic algorithm training

	Constitutive behavior prediction		Modified constitutive behavior	
	Lower bound	Upper bound	Lower bound	Upper bound
Step size optimization	0	1	0	1
Momentum optimization	0	1	0	1
PE element optimization	10	20	1	10

In the current research, the roulette method was utilized for selection of the best (most fit) networks. Roulette selection involved selection of networks based on the “survival of the fittest” methodology, in which selection was proportional to the fitness. In the roulette

selection, unfit networks were not selected for combination and mutation, while the “most fit” (high fitness) networks were selected for combination and mutation.

The evolutionary process ended once the maximum number of generations was reached. The maximum # of generations was 50 for this research, with a population size of 25 networks in each generation, which corresponded to 1,250 total networks that were evaluated for each computational experiment. For each network, the training iterations evolved for 2,000 epochs.

Subsequent to the evolution process, the network weights were saved to a *.bst file (best weights) for later retrieval. For an example of this type of file, see Appendix C. For an example of pseudocode that was used for GA training, please refer to Appendix D.

6.1.3. Artificial Neural Network (ANN) Computations

Neural network simulations were performed on a standard PC with a Pentium M processor at 1.86 GHz with 2.00 GB of RAM. The Neurosolutions SW (NeuroDimension, Inc., Gainesville, FL) package was utilized to model the data and perform the GA ANN simulations. For the genetic algorithm (GA) training, the *Train Genetic* function in Neurosolutions was implemented. For the constitutive behavior prediction of the samples with and without prior fatigue, a total of 43,825 data points were used for computation. From this, 70% were allocated for genetic training (30,678 points), 15% were allocated for cross-validation (6,574 points), and 15% were allocated for testing the networks (6,574 points). The genes of the network for the constitutive behavior prediction consisted of the 5-input vector space, denoted as:

$$X = \left\{ \sigma_{\max} \quad R \quad N \quad \tilde{\varepsilon} \quad \varepsilon_R \right\}^T \quad (6.1)$$

The output parameter was the stress (σ) from the neural network simulation. An example of the ANN architecture for prediction of the mechanical behavior of the fiber samples is shown in Figure 6.3. For the modified constitutive behavior approach, which will be described later in this chapter, approximately 70 points were used for each material property value (elastic modulus, hardening modulus, and yield point), where 70% of the data was devoted to training and 30% was devoted to testing the networks.

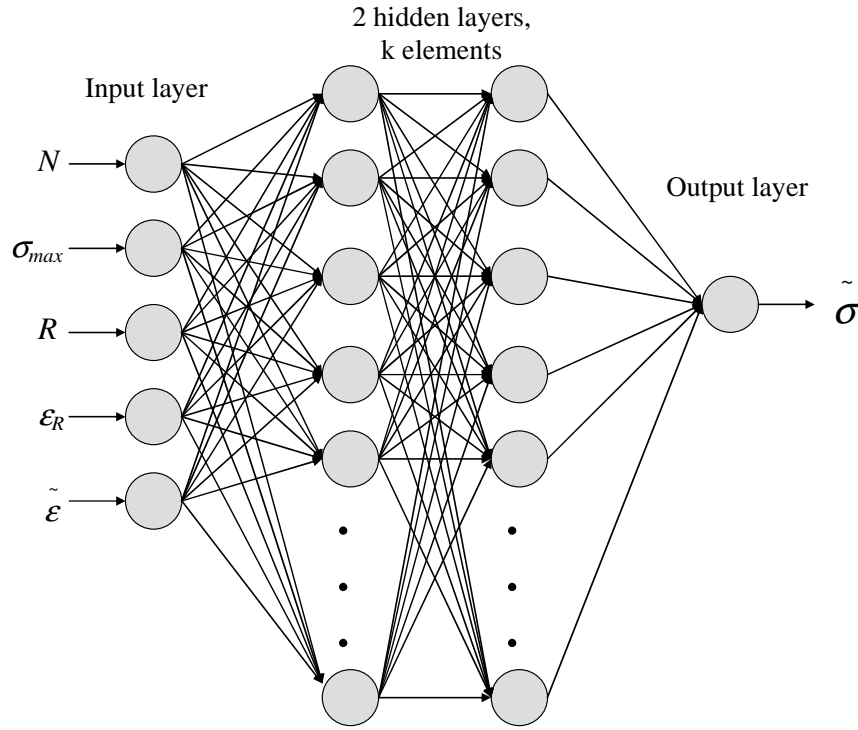


Figure 6.3. Schematic of ANN architecture used in this study for prediction of constitutive behavior of the PET-VGCNF samples subsequent to fatigue

An initial 5-10-10-1 architecture was utilized, which corresponded to 5 input neurons, 10 hidden neurons in the first hidden layer, 10 hidden neurons in the second hidden layer, and one output variable. In Figure 6.3, R represents the stress ratio, defined as:

$$R = \frac{\sigma_{\min}}{\sigma_{\max}} \quad (6.2)$$

Here, σ_{min} represents the minimum stress during fatigue loading and σ_{max} represents the maximum stress during fatigue loading. For PET control samples, stress ratios of $R=0$ and $R=0.333$ were utilized in this study and for the PET-VGCNF samples stress ratios of $R=0$, $R=0.333$, and $R=0.667$ were utilized. Also, in the input vector space, N represents the number of fatigue cycles, ε represents the strain in the axial loading direction (ε_{zz}), and ε_R represents the residual creep strain from the fatigue loading history, and was computed according to Equation (5.13).

All of the mechanical testing parameters, R , σ_{max} , and N were prescribed directly into the Enduratec machine. The parameter ε (uniaxial strain) was the result of the uniaxial test and ε_R (residual strain) is the function described in (5.13) that is the result of the fatigue loading test. An example of the strain evolution and retention of residual strain is shown in Figure 5.2.

6.2. Results and Discussion

6.2.1. Results from Fatigue – DMA Results

DMA tests were conducted on the samples to determine the transition from rubbery behavior (at low frequencies) to glassy behavior (at high frequencies) on the samples. A representative DMA curve is shown in Figure 6.4 illustrating the results. The samples showed a clear transition from rubbery to glassy behavior at approximately 40 Hz, based on the peak of the stiffness curve as shown in Figure 6.4. Frequencies that engendered shorter relaxation times (rubbery) are shown to the left of the 40 Hz bifurcation line and frequencies that resulted in longer chain relaxation times (glassy) are to the right of the 40 Hz bifurcation line in Figure 6.4.

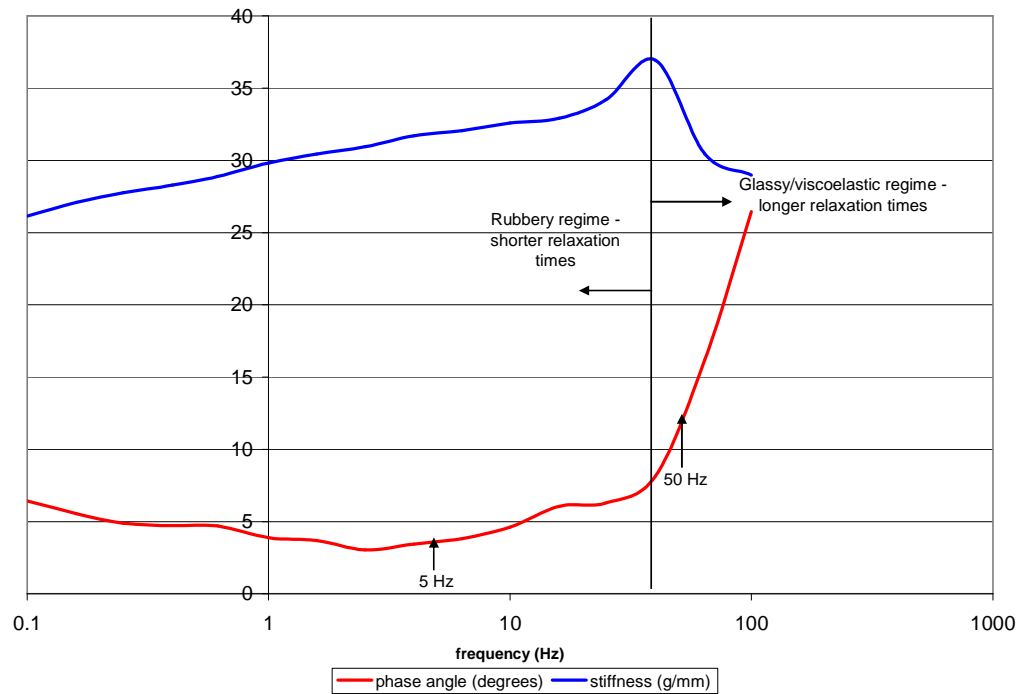


Figure 6.4. Representative DMA curve for PET-VGCNF sample indicating stiffness and phase angle vs. frequency

6.2.2. Results from Fatigue – Fatigue in the Viscoelastic/Glassy Regime

Fatigue tests were conducted on the PET control and PET-VGCNF fibers at 50 Hz to determine the fatigue resistance above the rubbery threshold. These fatigue tests were conducted at a maximum stress equal to 60% of the fracture stress of the respective samples, with a stress ratio of $R=0$.

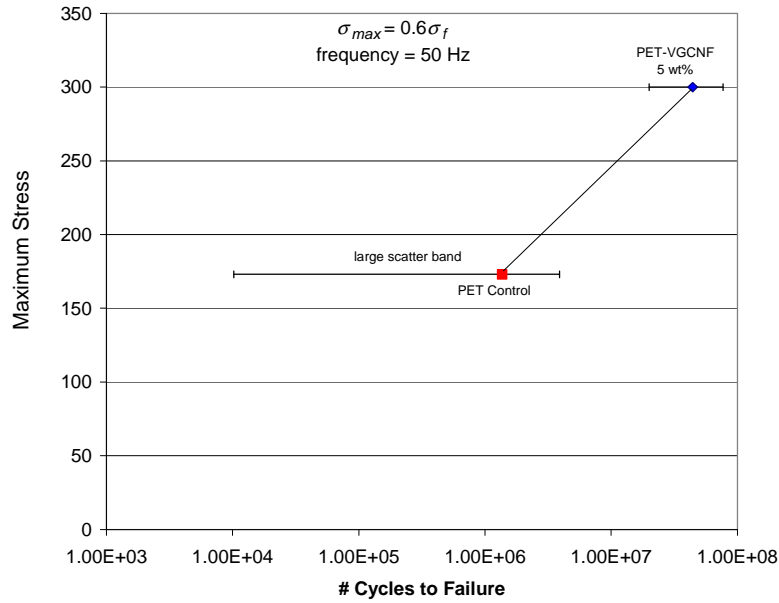


Figure 6.5. Results from fatigue tests at 50 Hz indicating the superior fatigue properties of the PET-VGCNF samples in the viscoelastic/glassy state

The results in Figure 6.5 indicate that the PET-VGCNF 5 wt% samples outperformed their respective unreinforced counterparts for almost two orders of magnitude more cycles at 50 Hz. There was significantly more scatter in the number of cycles to failure data for the PET control samples, as shown in Figure 6.5. These data represent the results from 7 samples tested under uniaxial fatigue conditions at 50 Hz. Four PET samples and three PET-VGCNF samples were tested to determine the average number of cycles to failure (N_f) value. These were lengthy experiments that took several weeks to complete due to the millions of cyclic iterations required for testing (i.e. 50E6 cycles @ 50 Hz requires 11.6 days of testing). These results are significant in the fact that one notices that PET-VGCNF fibers tested above the glass transition frequency are noticeably more resistant to failure than their PET unreinforced counterparts, even when tested at a

higher stress ($\sigma_{max}=300\text{MPa}$ for PET-VGCNF samples and $\sigma_{max}=170\text{MPa}$ for the PET control samples).

6.2.3. Results from Fatigue - Training & Testing Results

The genetic ANN training procedures were run two times and the results were averaged to obtain the stress-strain response of the materials with and without prior fatigue. The two training procedures represent different randomized data trials. The results from the conjugate gradient, GA training procedure are shown in Table 6.2. Results of the mean-squared error (MSE) were fairly low, with an average value of 0.00863 for the two runs. On average, the minimum MSE was reached between 3 and 4 generations. The testing results, which were obtained on stress values not previously provided to the neural network set, displayed mixed results, where the average correlation coefficient (r) for the two trials was 0.9269. To delineate the agreement of the testing results, the experimental stress values (actual) vs. the computational (predicted) stress values are shown in Figures 6.6 and 6.7. The R^2 value for Trial 1 was 0.8895 and the R^2 value for Trial 2 was 0.8297. What should be noticed from these results is that on Trial 1, good agreement was obtained between the experimental output stress and the predicted output stress. However, on Trial 2, which represents another randomized trial, although the R^2 value was 0.8297 there was a poor agreement due to the fact that the predicted output stress value was shifted from 0 up to approximately 100 MPa. This did not reflect the true experimental constitutive response of the material.

Table 6.2. Optimization summary results for GA neural networks-conjugate gradient (5-10-10-1 architecture) for PET-VGCNF samples

	Training Results		Testing Results
	Min MSE	Generation	r
Trial 1	0.00655	4	0.9431
Trial 2	0.0107	3	0.9108
Average	0.00863	3.5	0.9269

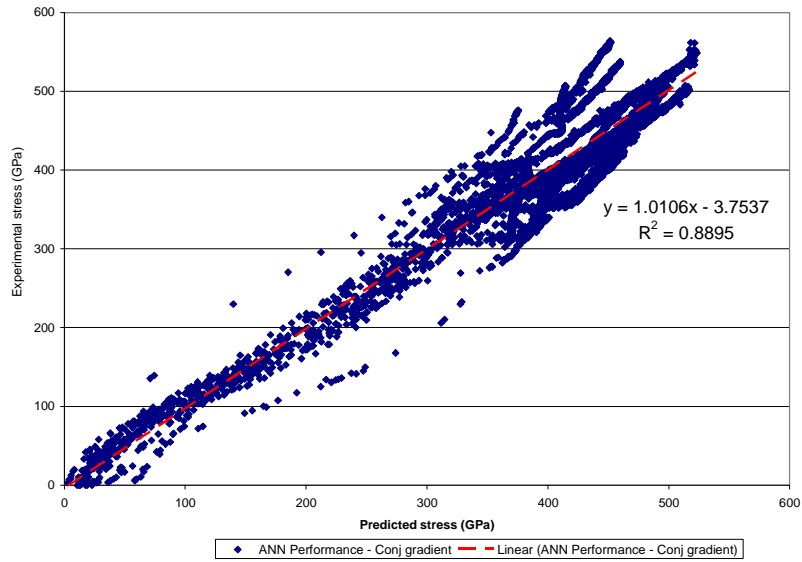


Figure 6.6. Randomized trial 1: Experimental stress (actual) vs. predicted stress from GA ANN for constitutive behavior prediction of samples representing good correlation

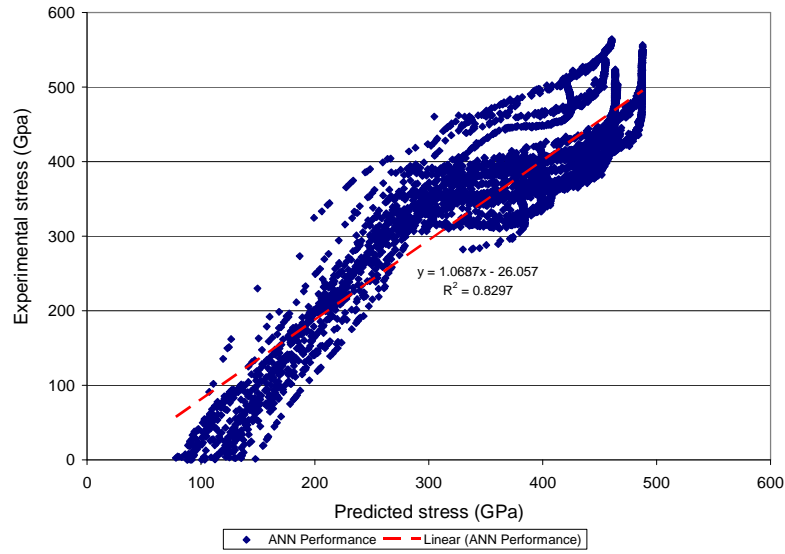


Figure 6.7. Randomized trial 2: Experimental stress vs. predicted stress from GA ANN for constitutive behavior prediction of samples representing overestimation of the predicted stress (poor correlation)

In addition to the results from the testing and training procedures, a sensitivity analysis was performed on the networks in Trials 1 and 2 to determine the effect of each input variable on the output (stress) signal. The results of this sensitivity analysis are shown in Figure 6.8. To conduct the sensitivity analysis, each individual input signal was varied while the other inputs remained constant. This was done in an effort to determine the change in the output signal (“sensitivity”) with respect to the variation of the input signal. It is seen from Figure 6.8 that the number of cycles (N) was the least important parameter in affecting the stress output. Intuitively, the strain (ϵ) showed the strongest correlation to the output stress signal. Surprisingly, the residual creep strain parameter (ϵ_R) exhibited the second lowest sensitivity. However, it is known from the experimental results and residual property predictions [129] that the post-fatigue mechanical behavior of both PET and PET-VGCNF fiber samples is a strong function of ϵ_R . The graphical results in Figure

6.9 that illustrate example stress-strain responses of the samples before and subsequent to fatigue loading exhibit results that correlate with the results in Figures 6.6 and 6.7. From Figure 6.9, it is shown that the GA based ANN trained via conjugate gradient procedure was very efficient at representing the unfatigued response of the materials. In contrast, the GA based ANN trained via backpropagation was not successful at representing the unfatigued constitutive behavior of the samples, as it displayed a distinct overshoot of the yield point. It should also be noticed from Figure 6.9 that both the BP with momentum and conjugate gradient based genetic algorithms were both unsuccessful at representing the constitutive response of the fatigued samples. Thus it was decided that the network should be modified to accommodate for the exclusion of the input variable N from the input vector set and the implementation of a new constitutive law to accurately reflect the linear elastic strain hardening constitutive behavior, which will be discussed in the next section. From Figure 6.9, one can see the gradual decreases in the hardening behavior with the further accretion of residual strain, as well as an abrupt change in slope subsequent to yield.

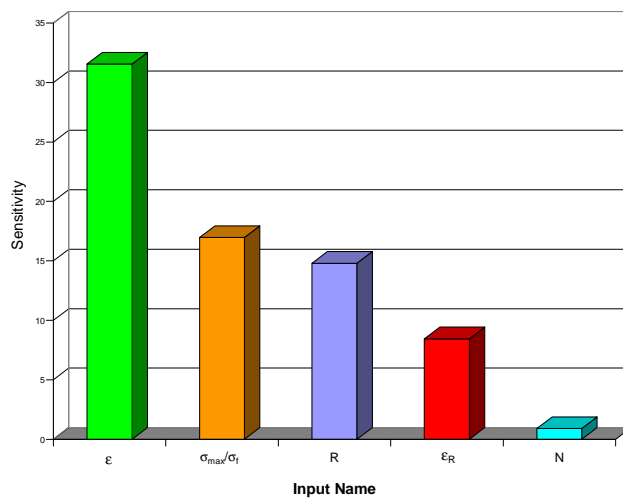


Figure 6.8. Genetic ANN sensitivity analysis of the input parameters for prediction of the constitutive behavior of PET-VGCNF samples

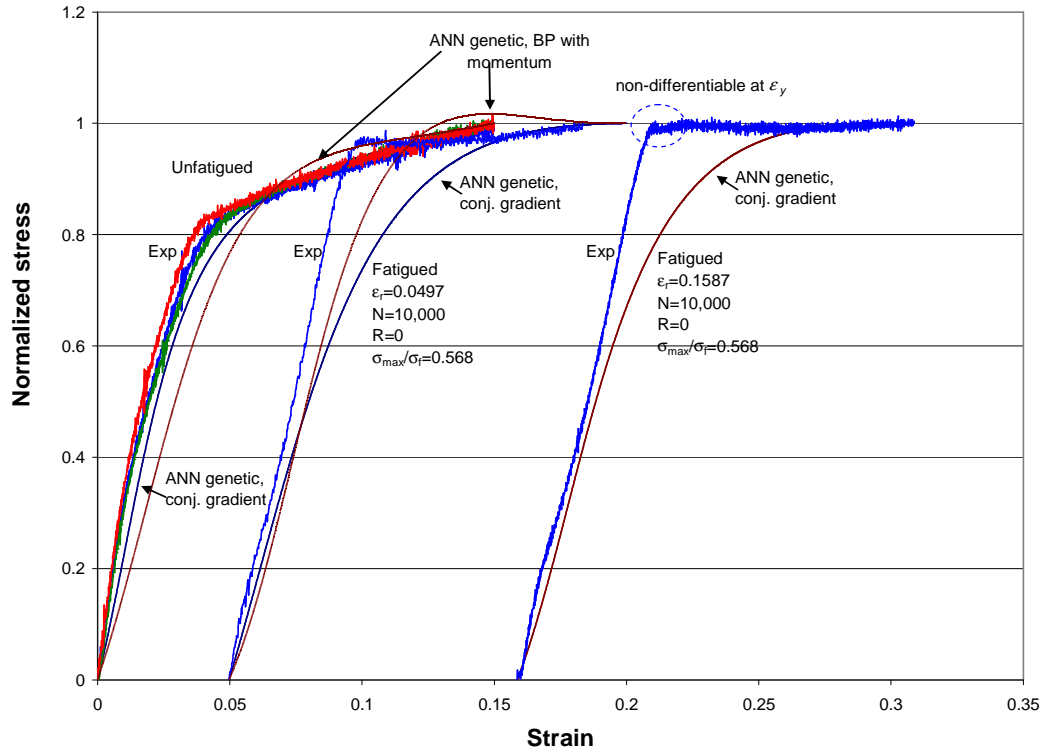


Figure 6.9. Results from Trials 1 and 2 from ANN genetic neural networks used to predict unfatigued and post-fatigue constitutive response of PET and PET-VGCNF fibers, indicating the poor capability of the ANN genetic procedure to capture the sharp transition in stress-strain behavior at ϵ_y

6.2.4. Results for Prediction of Constitutive Response – Different Approach

The ANN testing results from Section 6.2.3 indicate that a different approach was necessary for the successful modeling of the constitutive response of the PET and PET-VGCNF materials subsequent to fatigue loading. From the experimental results, it is known that the post-fatigue stress-strain response of the materials is linear-elastic, strain hardening with a clearly defined yield point. Thus, from a mathematics viewpoint, it can be stated that the post-fatigue constitutive response is non-differentiable at ϵ_y . The mathematical statement that expresses this discontinuity in the constitutive response at the yield point (ϵ_y) is:

$$f'(x) = \lim_{h \rightarrow 0} \frac{f(\varepsilon_y + h) - f(\varepsilon_y)}{h} \text{ is nonexistent} \quad (6.5)$$

Because of this discontinuity, an open-form solution was utilized to capture the stress-strain response, and the GA neural network was retrained to determine the correct response. The open-form mathematical relationship that appositely describes this piecewise constitutive behavior is:

$$\tilde{\sigma} = \tilde{\sigma}(\tilde{X}) = \begin{cases} E(\tilde{X})\varepsilon & \varepsilon < \varepsilon_y \\ E(\tilde{X})\varepsilon_y(\tilde{X}) + H(\tilde{X})\left[\varepsilon - \varepsilon_y(\tilde{X})\right] & \varepsilon \geq \varepsilon_y \end{cases} \quad (6.6)$$

In Equation (6.6), $E(\tilde{X})$, $\varepsilon_y(\tilde{X})$, and $H(\tilde{X})$ represent the modulus, yield strain, and hardening modulus as a function of the input mechanical testing parameters. Thus, the task was to determine the three functions (modulus, yield strain, and hardening modulus) as a function of the input vector space using the GA based neural networks. One should refer to Appendix E for a schematic representation of the structure of the ANNs utilized for these computations.

The ANNs were retrained using a GA based BP with momentum procedure. Figures 6.10-6.15 indicate the capability of the network in minimizing the MSE cost function over the number of network generations. In total, 9 trials were run to determine the mechanical properties stated in Equation (6.6) (3 trials for $E(\tilde{X})$, 3 trials for $\varepsilon_y(\tilde{X})$, and 3 trials for $H(\tilde{X})$). The parameters used for step size, momentum, and #PE optimization are provided in Table 1.

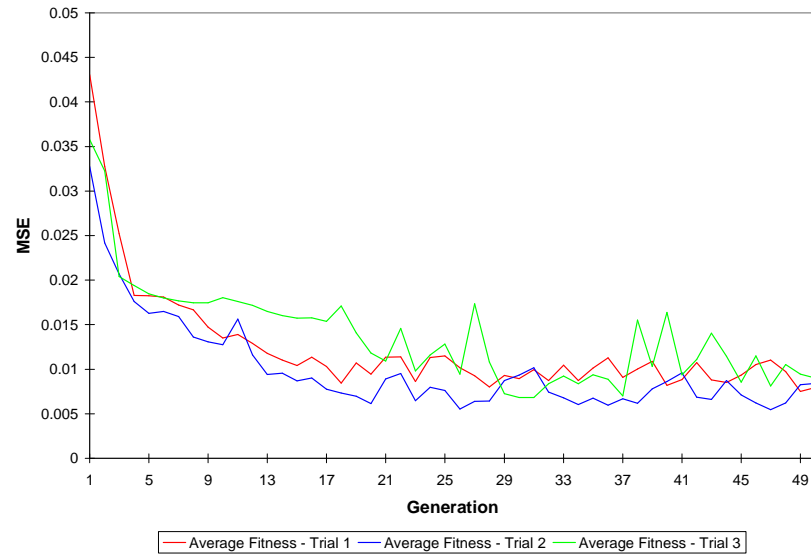


Figure 6.10. MSE vs. generation for 3 ANN genetic trials: hardening modulus ($H(X)$) prediction

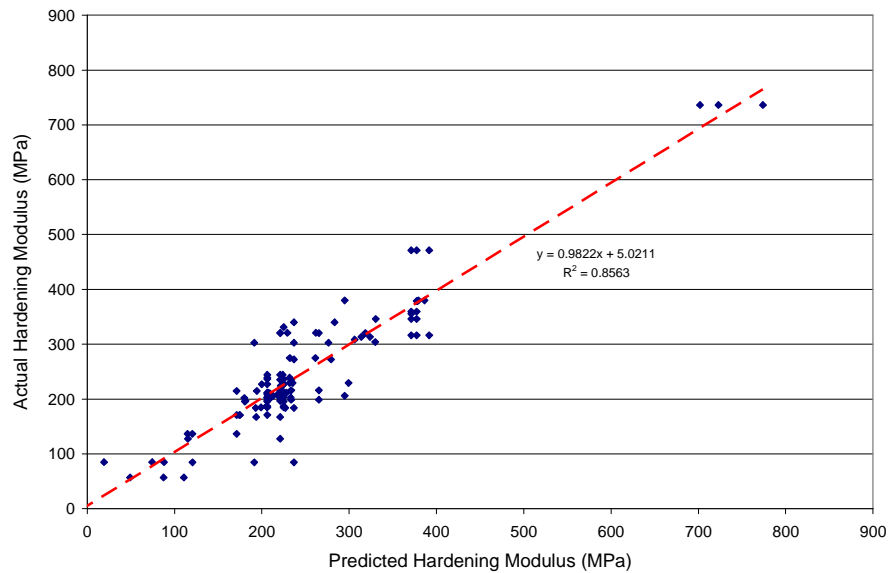


Figure 6.11. Actual vs. ANN genetic predicted hardening modulus ($H(X)$) of PET & PET-VGCNF fibers

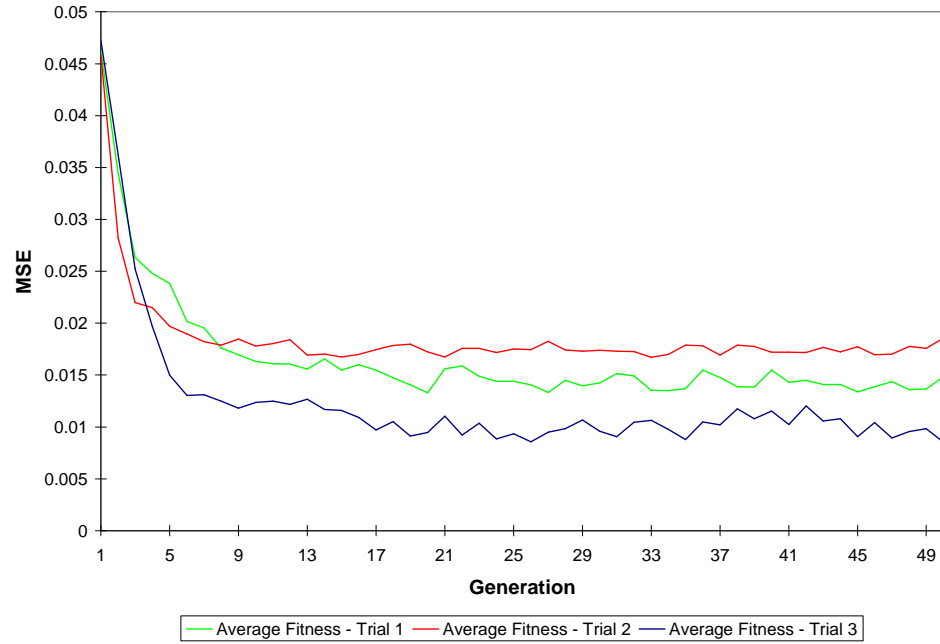


Figure 6.12. MSE vs. generation for 3 ANN genetic trials: yield strain ($\epsilon_y(X)$) prediction of PET & PET-VGCNF fibers

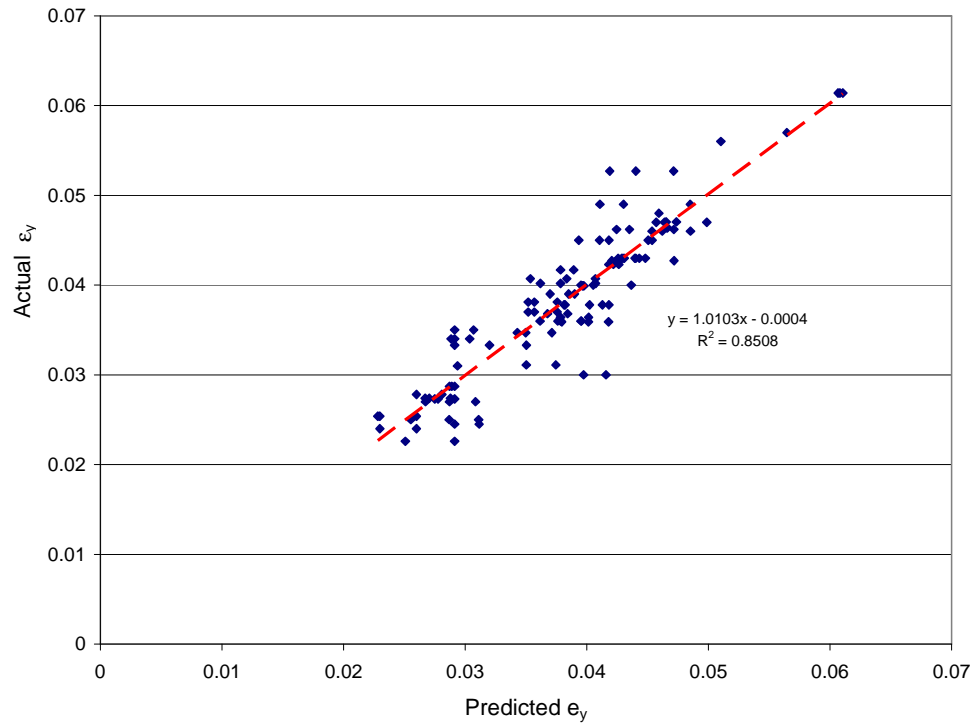


Figure 6.13. Actual vs. ANN genetic predicted yield strain ($\epsilon_y(X)$) of PET & PET-VGCNF fibers

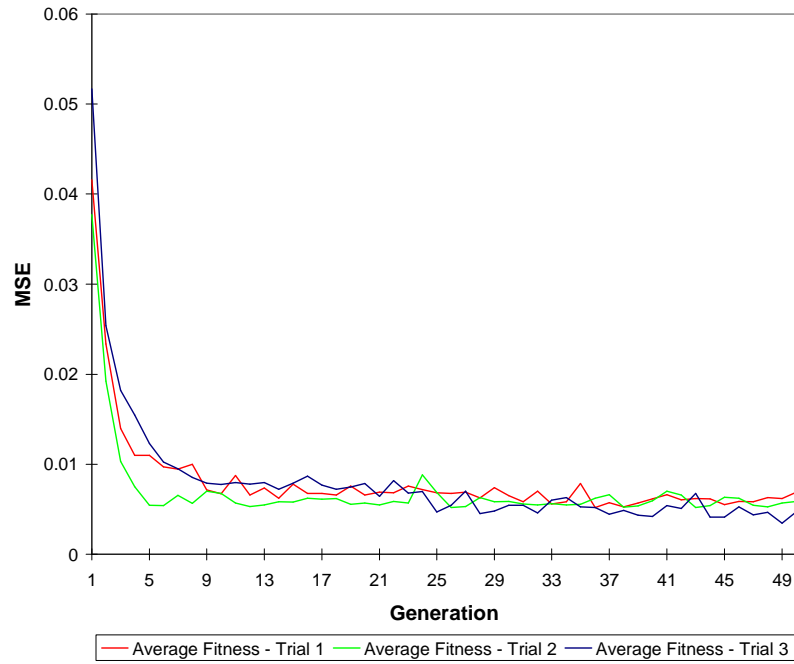


Figure 6.14. MSE vs. generation for 3 ANN genetic trials: elastic modulus ($E(X)$) prediction of PET & PET-VGCNF fibers

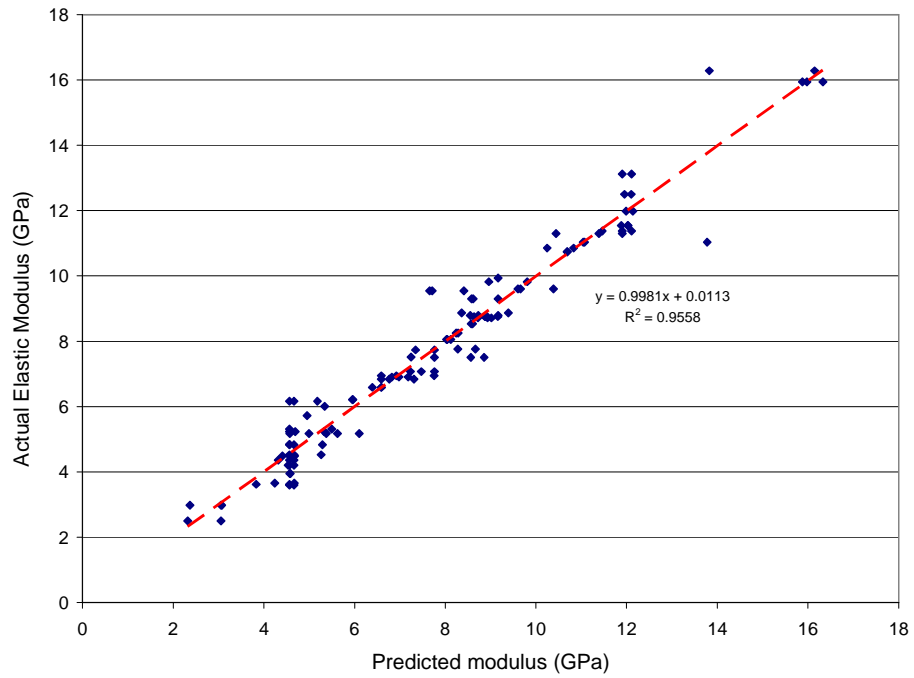


Figure 6.15. Actual vs. ANN genetic predicted elastic modulus ($E(X)$) of PET & PET-VGCNF fibers

The results from the simulations were satisfactory, as shown from Figures 6.10-6.15, where the MSE vs. generation and actual vs. ANN genetic plots are provided. The constitutive response of the materials was again plotted to illustrate the effectiveness of the new approach, and the results are displayed in Figure 6.16.

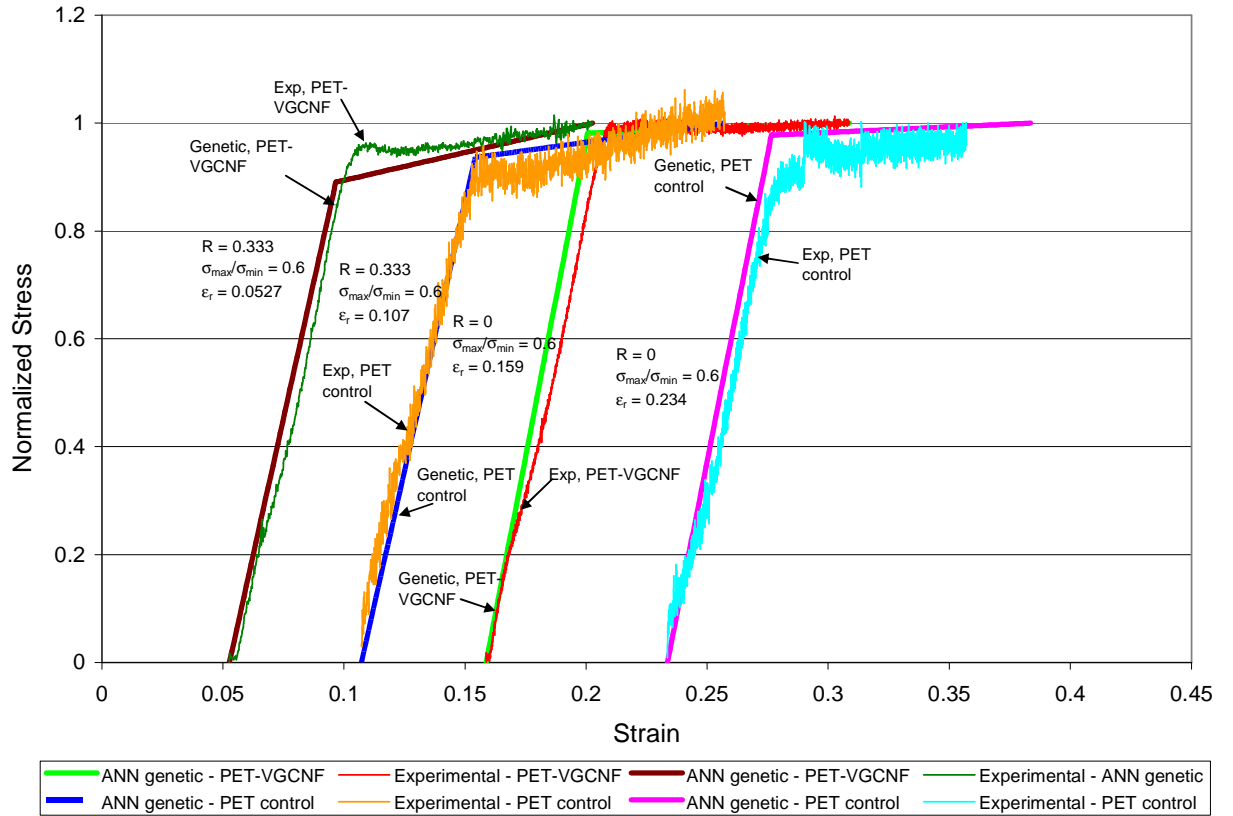


Figure 6.16. Representative normalized stress-strain curves of PET control and PET-VGCNF samples (experimental and GA neural network predictions) subsequent to fatigue loading. The data to the left of the curve prescribe the testing conditions of the sample

The results in Figure 6.16 indicate that the GA neural network procedure was more efficient than the aforementioned method at capturing the constitutive response of both PET and PET-VGCNF fibers, indicating the applicability of the open-form constitutive law outlined in Equation 6.6.

Conclusions for Chapter 6

Fatigue experiments were conducted on PET control and PET-VGCNF samples to determine the mechanical behavior of the materials. For both PET control and PET-VGCNF samples conducted at 50 Hz, the results indicate that the fatigue resistance of the PET-VGCNF samples was approximately 2 orders of magnitude higher than their unreinforced counterparts. For tests conducted at 5 Hz, residual strength tests were performed to ascertain the change in material properties and constitutive behavior subsequent to fatigue loading. Genetic algorithm (GA) based artificial neural networks (ANNs) were used to model the constitutive response of both PET control and PET-VGCNF samples with and without prior fatigue. The GA based ANNs were successful at replicating the constitutive behavior of samples without prior fatigue, due to the nonlinearity and continuity of the stress-strain curve. However, for samples with prior fatigue, an open-form solution was necessary to capture the stress-strain response of the materials, due to the non-differentiable behavior at ε_y . Based on the neural network testing results, the GA based ANNs were not successful at representing the post-fatigue response of the materials. In actuality, the ANNs generated continuous and differentiable functions. However, when a piecewise linear elastic strain hardening model was implemented, good results were achieved for the model of the post-fatigue stress-strain response. This work is significant in the sense that both computational researchers and other scientists and engineers can benefit from understanding the employment of neural networks applied to unreinforced polymeric and nanocomposite material behavior.

CONCLUSIONS OF DISSERTATION

Due to the results of the current study, the scientific community now has a better understanding of fatigue and degradation mechanisms that occur in VGCNF reinforced fibers and nanoclay reinforced composite films. Currently, there is little research related to fatigue of single polymeric fibers and their nanocomposite counterparts. In addition, there is very little work on fatigue of nanocomposite films. The research that does exist is limited in the sense that it does not reflect the evolution of damage accumulation in the material. Thus traditional approaches are not solely sufficient in the sense that they are purely phenomenological and do not reflect any microstructural changes that occur as a result of fatigue. The research that has been completed in this dissertation helped to mitigate this gap by indicating how the maximum stress and number of cycles to failure are correlated to the stress whitening (opaque regions) that are observed around the cracked region. Within the semi-phenomenological framework that was developed for the PET and PET-VGCNF fibers, the objective was to clarify and elucidate factors that affect the fatigue strength and other mechanical properties as a result of fatigue loading. This objective was accomplished utilizing experimental, ANN modeling, and fractography. The experimental, modeling, and fractography results from the fatigue experiments can serve as a great utility for manufacturers and fabrication specialists seeking to design unreinforced and nanocomposite materials that can withstand fatigue stresses.

Another objective of the research was to identify the primary cause of failure, or instability, for single nanocomposite fibers uniaxially loaded in tension and under fatigue loading. There is a void of research in the area of failure mechanisms that occur in single

fibers reinforced with vapor grown nanofibers and other nanofillers due to the fact that a testing methodology has not been established to specifically ascertain the primary cause of failure. This dissertation has helped to alleviate the gap by using an established fractography methodology to compare the results of both neat and nanocomposite fibers that were subjected to fatigue loading. A distinct difference in the fractography was observed between the neat samples and nanocomposite samples that were subjected to uniaxial and fatigue loading.

FUTURE WORK

Based on the experimental and computational results from this study, there are several areas can be expounded upon. Firstly, a computational study can be done on the PLA and PLA nanocomposite films utilizing neural networks to accurately predict the number of cycles to failure and the time to failure by relating these output variables to the input variables (maximum stress, frequency, % light transmission, etc). A structure similar to that shown in Figure 6.17 could be used to predict the number of cycles to failure. In addition, one could also replace the light transmission state variable with a more sensitive structural variable, such as the scattering intensity that is derived from small angle x-ray scattering (SAXS) experiments. It is believed that the SAXS experiments would be sensitive enough to damage accumulation to provide a strong enough sensitivity to the output variable, N_f .

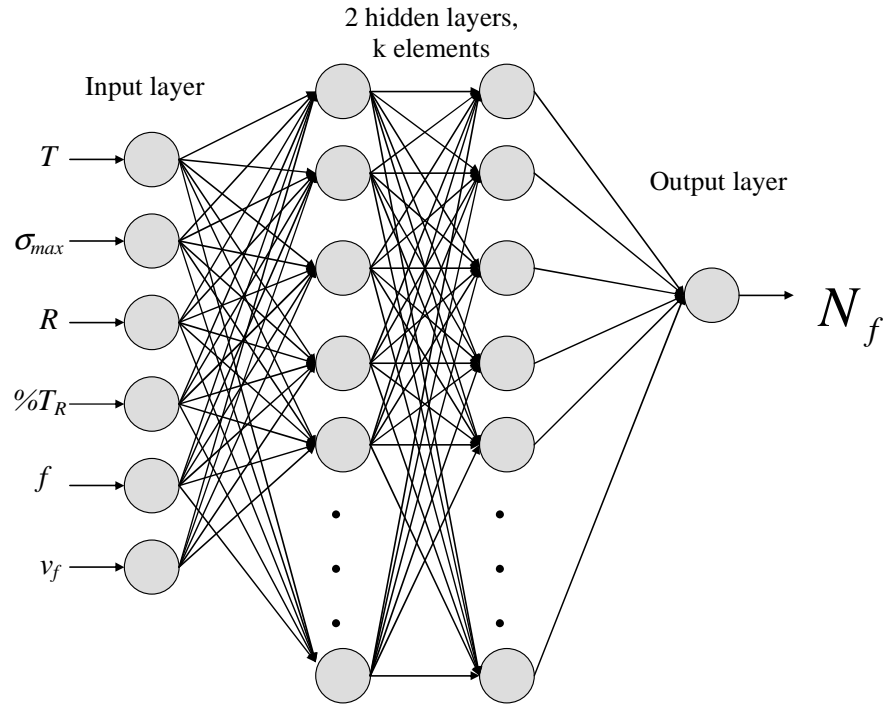
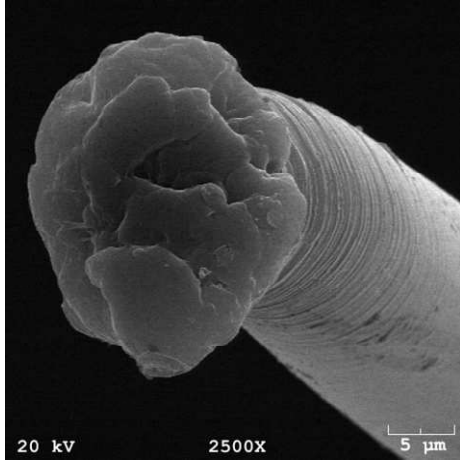


Figure 6.17. Idealized ANN architecture for prediction of number of cycles to failure (N_f) in PLA and PLA nanoclay films

Next, a thorough SEM study should be conducted on the films at high magnifications to ascertain the mode of failure (i.e. pull-out of platelet particles and/or platelet fracture) under uniaxial tension and fatigue loading conditions. A classification neural network scheme can then be used to predict the type of failure that is expected based upon certain mechanical input conditions. A fracture mechanics study should also be conducted on the films to provide a comparison of the differences in energy release rate vs. initial flaw size. A thorough impact fracture mechanics study should also be conducted on the PLA nanocomposite and PLA unreinforced films to determine their resistance to impact loads.

From the conclusions of the PET unreinforced and PET-VGCNF fibers, it would be interesting to determine how the fatigue resistance and residual property behavior of the samples behaves as a function of temperature. In addition, a study should be done with different types of reinforcement agents to determine the effect on fatigue resistance. Based on these results, a more robust computational neural network model could be developed and used to predict the mechanical behavior.

APPENDIX A: OTHER SEM FRACTOGRAPHS OF PET AND PET-VGCNF FIBERS

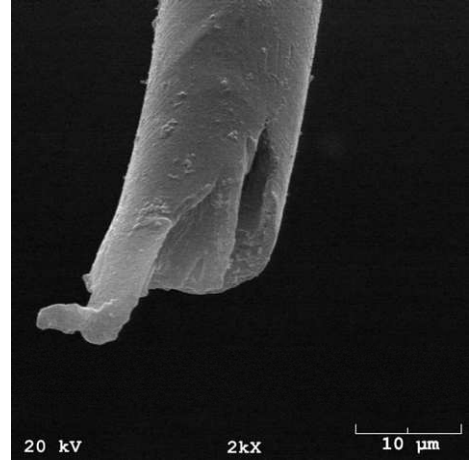


PET Control Sample

$$R=1/3$$

$$\epsilon_R = 10.7\%$$

$$N = 6,000 \text{ cycles}$$

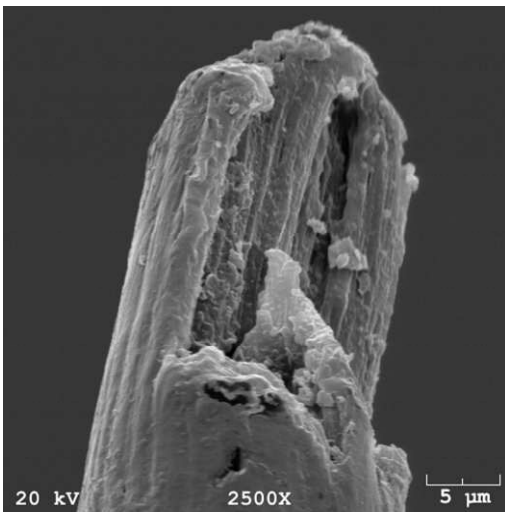


PET Control Sample

$$R=1/3$$

$$\epsilon_R = 2.7\%$$

$$N = 100,000 \text{ cycles}$$

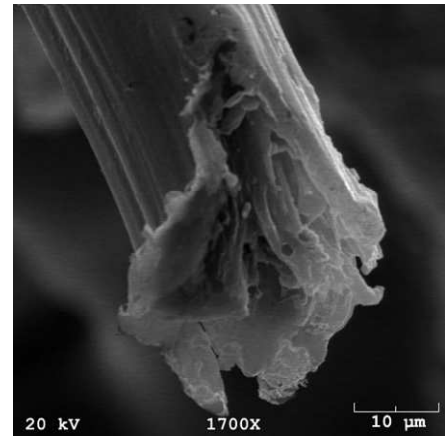


PET-VGCNF Sample

$$R=1/3$$

$$\epsilon_R = 0.78\%$$

$$N = 25,000 \text{ cycles}$$



PET-VGCNF Sample

$$R=0$$

$$\epsilon_R = 0$$

$$N = 1,000 \text{ cycles}$$

APPENDIX B: NEURAL NETWORK MODELS

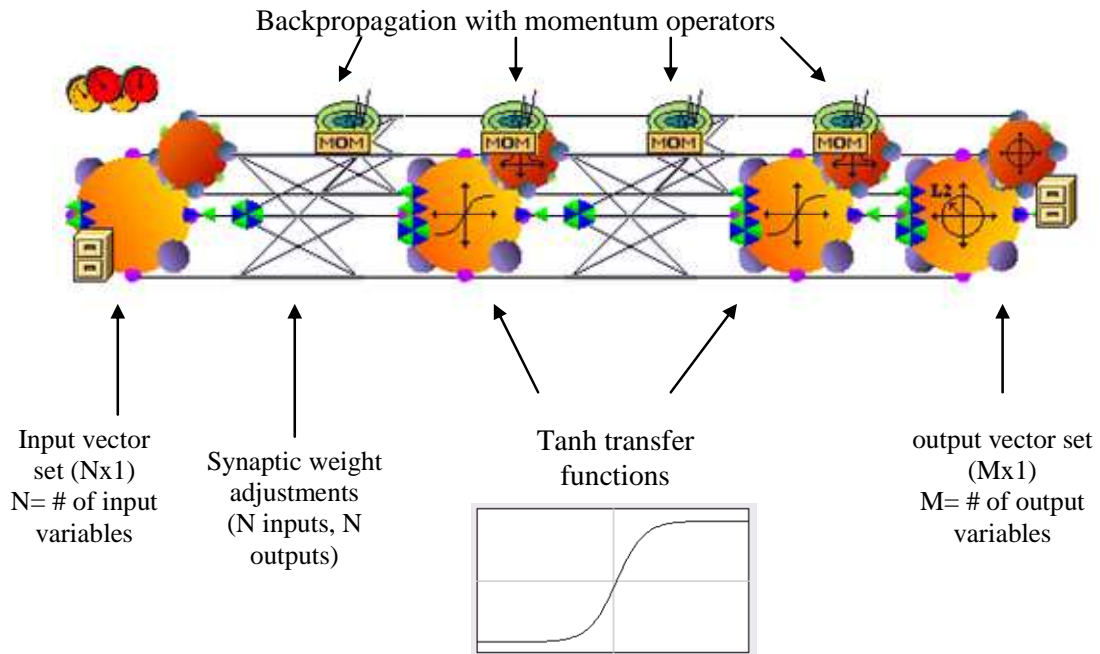


Figure B.1. Example BP with momentum ANN architecture with various network parameters utilizing Neurosolutions modeling SW

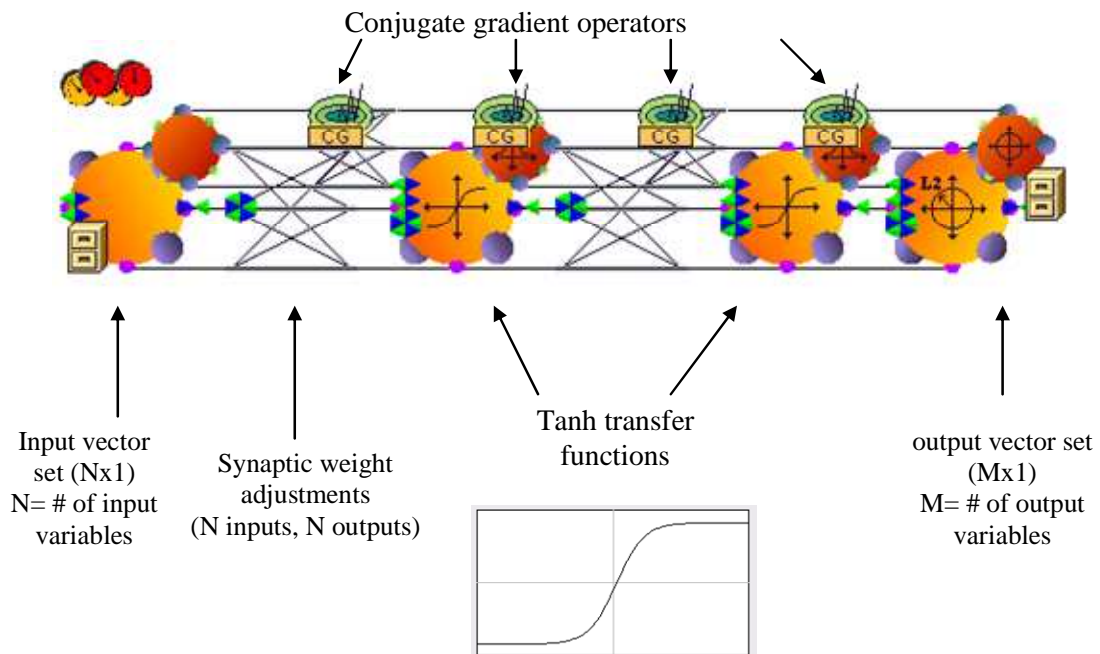


Figure B.2. Example conjugate gradient ANN architecture with various network parameters using Neurosolutions modeling SW

APPENDIX C: EXAMPLE ANN WEIGHT DATABASE FILE

```
//      Weights      saved      from      breadboard      C:\Documents      and
Settings\Rodney\Desktop\Ph.D.  Dissertation\PET  Fibers\PET  and  PET
piecewise data-BP with mom-Trial 3-E.nsb.

// Saved after epoch 2000, exemplar 0.

//Filename:  PET  and  PET  piecewise  data-BP  with  mom-Trial  3-
E.genetic.bst

#NSWeightFileVersion 243


#inputFile File

4
1.9565217391304346e-001 -2.1913043478260867e+000
7.7060509071912042e+000 -9.0000000000000002e-001
2.7449999996568755e+000 -9.00000000000000024e-001
2.6999999986500001e+000 -9.0000000000000002e-001

4
0
4
1
1
1
1
1
1
1
1
1
1

#desiredFile File
```

```

1
1.3061227868537131e-001 -1.2266597893182514e+000
0

#inputAxon Axon
4 1
1
0

#hidden1Axon TanhAxon
7 1
1
7          7.9095237631544549e+001          -1.9060069028715773e+001          -
2.2136014547787110e+002          -3.6017953932281323e+001
9.6353687230757316e+001          -1.6439352165475402e+001
3.2757545868036999e+000

#outputAxon TanhAxon
1 1
1
1 1.5946804361957878e-001

#criterion L2Criterion
1 1
1
0

#hidden1Synapse FullSynapse

```

28	-1.4127499076867585e+002	1.7310735845025840e+002	-
2.3699973717633817e+001		6.7599961913121433e+001	-
2.4891343126708879e+001		-8.8995582447045422e+001	-
4.3185911084428303e+000		-5.4219638586472016e+001	
1.4188597068463795e+002		-1.1765632492008375e+002	-
7.7794249186279629e+001	6.3575457297401421e+000	3.6631648108229335e+001	
-3.7951206547839064e+001		-1.1984342823342965e+001	
5.5913409861043899e+000		-3.1153339505348196e+001	
6.5135417354998140e+001		-2.0601316103305653e+001	
1.2979215901874763e+001		-2.3312569997905126e+001	-
3.7628493558679061e+001	2.4159483062849834e+001	2.9538339482560598e+000	
-5.0318881222283913e+001		4.1221253868020973e+001	
2.0278700993366783e+001	-7.7830114720013190e+000		

#hidden1SynapseBackprop BackFullSynapse

28	0.0000000000000000e+000	0.0000000000000000e+000
0.0000000000000000e+000	0.0000000000000000e+000	0.0000000000000000e+000
0.0000000000000000e+000	0.0000000000000000e+000	0.0000000000000000e+000
0.0000000000000000e+000	0.0000000000000000e+000	0.0000000000000000e+000
0.0000000000000000e+000	0.0000000000000000e+000	0.0000000000000000e+000
0.0000000000000000e+000	0.0000000000000000e+000	0.0000000000000000e+000
0.0000000000000000e+000	0.0000000000000000e+000	0.0000000000000000e+000
0.0000000000000000e+000	0.0000000000000000e+000	0.0000000000000000e+000
0.0000000000000000e+000	0.0000000000000000e+000	0.0000000000000000e+000
0.0000000000000000e+000	0.0000000000000000e+000	0.0000000000000000e+000
0.0000000000000000e+000	0.0000000000000000e+000	0.0000000000000000e+000

#outputSynapse FullSynapse

```
7 -2.6246067041756832e-001 2.0322565054490435e-001 7.9569725339638930e-
001 -1.5878424839894811e-001 1.8216397501796548e-002
2.3258017228538599e-001 -4.5547602973141049e-001
```

```
#outputSynapseBackprop BackFullSynapse
```

```
7 0.0000000000000000e+000 0.0000000000000000e+000
0.0000000000000000e+000 0.0000000000000000e+000 0.0000000000000000e+000
0.0000000000000000e+000 0.0000000000000000e+000
```

```
#hidden1SynapseBackpropGradient Momentum
```

```
28 -7.2134208043970596e-002 9.1539581217165947e-002 -
1.6425903105207681e-002 3.1104970570750668e-002 -1.2717547793109454e-
002 -4.7326311716032937e-002 -1.8062698036747811e-003 -
2.7905649234722250e-002 6.9911900018219175e-002 -6.5935239385609745e-
002 -3.8067269395222383e-002 6.2270920175213794e-003
1.8665632641082779e-002 -1.9280744183824125e-002 -5.4257680122097481e-
003 3.0607859151620211e-003 -1.9477236865748829e-002
3.3673288437948146e-002 -1.1308613623061530e-002 7.8785718139145391e-
003 -1.0512469069480772e-002 -2.2143192241054054e-002
1.5279319930692366e-002 -7.7908632430909047e-005 -2.6446922608194635e-
002 2.1288390457059950e-002 1.0567275790305515e-002 -
5.3624350786773715e-003
```

```
#hidden1AxonBackpropGradient Momentum
```

```
7 4.1851781544271667e-002 -9.9609225543008852e-003 -
1.1257890650615640e-001 -1.7432664471243153e-002 4.7202592699732898e-
002 -1.4165639989982352e-002 5.7798424311618730e-005
```

```
#outputSynapseBackpropGradient Momentum
```

```
7          -4.1540324599749252e-006          1.8451494008947929e-005          -  
1.4746945649507135e-004  4.3518184986320308e-005  6.4773113601926190e-005  
-2.1431216013797234e-005  1.6753765450055720e-005
```

```
#outputAxonBackpropGradient Momentum
```

```
1 -1.6187834218083755e-004
```

```
#control StaticControl
```

```
0
```

```
1.0000000000000000e+009
```

```
0
```

```
0
```

```
0
```

APPENDIX D: EXAMPLE PSEUDOCODE FOR GENETIC ALGORITHM COMPUTATIONS

Pseudocode for GA training and constitutive behavior determination of PET and PET-VGCNF samples – Adapted from Maiti et al. [155]

```
begin
Initialize GA parameters      “Initialize step sizes, momentum, inputs, populations,
generations, evolution time, #PEs”
g=0                          “g represents current generation”
initialize p(t)              “ p(t) represents the population at t-th generation”

evaluate p(t)
while ( not terminate condition )
{
t =t +1
select p(t) from p( t-1)
alter ( crossover and mutate ) p(t)
evaluate p(t)
upgrade the result, if possible
}
store weights of the best result found
end program
```

APPENDIX E: STRUCTURE OF NETWORKS USED FOR MODIFIED CONSTITUTIVE BEHAVIOR PREDICTION

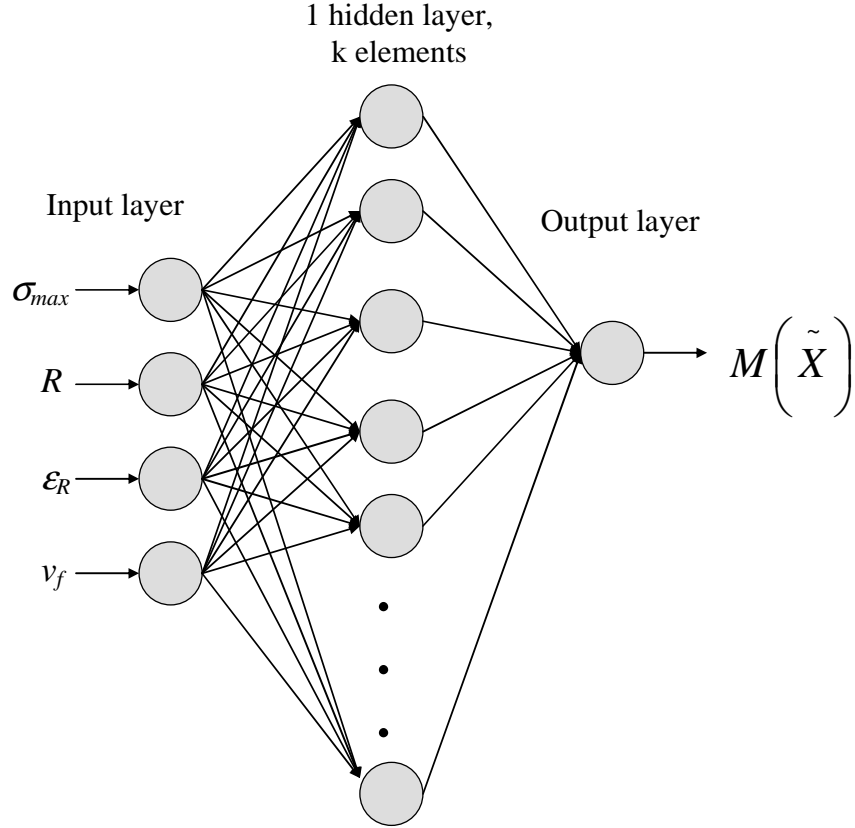


Figure E.1. ANN structure for material property prediction of PET and PET-VGCNF fibers using GA training. Here $M(X)$ corresponds to the material property output (elastic modulus, hardening modulus, or yield strain)

REFERENCES

1. Gyu-Ho Kim and Hongbing Lu, Characteristics of accelerated lifetime behavior of polycarbonate under athermal and high loading frequency conditions, *Polymer Testing*, Volume 26, Issue 7, October 2007, Pages 839-845.
2. M. Kawai and M. Koizumi, Nonlinear constant fatigue life diagrams for carbon/epoxy laminates at room temperature, *Composites Part A: Applied Science and Manufacturing*, In Press, Corrected Proof, Available online 30 January 2007.
3. E. Altus and A. Herszage, A two-dimensional micromechanic fatigue model, *Mechanics of Materials*, Volume 20, Issue 3, May 1995, Pages 209-223.
4. Z.D. Wang and X.X. Zhao, Modeling and characterization of viscoelasticity of PI/SiO₂ nanocomposite films under constant and fatigue loading, *Materials Science and Engineering: A*, In Press, Accepted Manuscript, Available online 25 September 2007.
5. Yuanxin Zhou, Vijay Rangari, Hassan Mahfuz, Shaik Jeelani and P.K. Mallick, Experimental study on thermal and mechanical behavior of polypropylene, talc/polypropylene and polypropylene/clay nanocomposites, *Materials Science and Engineering: A*, Volume 402, Issues 1-2, 15 August 2005, Pages 109-117.
6. Ming-Hwa R. Jen, Yu-Chung Tseng and Chun-Hsien Wu, Manufacturing and mechanical response of nanocomposite laminates, *Composites Science and Technology*, Volume 65, Issue 5, Papers presented at the European Materials Research Society 2004 Spring Meeting: Nano-Composites for Space and Infrastructure Applications, April 2005, Pages 775-779.
7. Jan Dusza, Pavol Sajgalik, Marc Steen and Ernst Semerad, Dynamic fatigue of a Si₃N₄+SiC nanocomposite at 1350[degree sign]C, *Materials Science and Engineering A*, Volume 291, Issues 1-2, 31 October 2000, Pages 250-255.
8. Ward, I., Hadley, DW, *An Introduction to the Mechanical Properties of Solid Polymers*. 1993, West Sussex: John Wiley & Sons, Ltd. 348.
9. A. G. Thomas., *Journal of Polymer Science.*, 31, 467 (1958).
10. G. J. Lake and A. G. Thomas., *Proc. Roy. Soc. A*300, 108 (1967).
11. G. J. Lake and P. B. Lindley, in *Proceedings of the Conference on the Physical Basis of Yield and Fracture*, Oxford, 1966, p. 176.
12. T. L. Anderson, "Fracture Mechanics: Fundamentals and Applications" (1995) CRC Press.

13. Norman E. Dowling. Mechanical Behavior of Materials: Engineering Methods for Deformation, Fracture, and Fatigue, 2/E. Prentice Hall. Upper Saddle River, New Jersey, 1999.
14. H. Jahed, A. Varvani-Farahani / International Journal of Fatigue 28 (2006) 467–473.
15. Anouk de Brauwere, Rik Pintelon, Fjo De Ridder, Johan Schoukens, Willy Baeyens, Estimation of heteroscedastic measurement noise variances, Chemometrics and Intelligent Laboratory Systems, Volume 86, Issue 1, 15 March 2007, Pages 130-138.
16. Kassapoglou, Christos. Fatigue life prediction of composite structures under constant amplitude loading. Journal of Composite Materials, v 41, n 22, November, 2007, p 2737-2754.
17. Wu, W.F., Ni, C.C. Statistical aspects of some fatigue crack growth data. Engineering Fracture Mechanics, v 74, n 18, December, 2007, p 2952-2963.
18. Bolick, Ronnie L., Kelkar, Ajit D. Innovative method for improving composite fatigue life estimations. Collection of Technical Papers - AIAA/ASME/ASCE/AHS/ASC Structures, Structural Dynamics and Materials Conference, v 4, Collection of Technical Papers - 48th AIAA/ASME/ASCE/AHS/ASC Structures, Structural Dynamics, and Materials Conference, 2007, p 3757-3763.
19. Zhang, Fu-Ze. Law of fatigue scatter factor versus test stress. Hangkong Xuebao/Acta Aeronautica et Astronautica Sinica, v 28, n 3, May, 2007, p 582-585.
20. Enrique Castillo, A. Fernandez-Canteli and Ali S. Hadi, On fitting a fatigue model to data, International Journal of Fatigue, Volume 21, Issue 1, January 1999, Pages 97-105.
21. Hongwei Shen, Jizhong Lin and Ensheng Mu, Probabilistic model on stochastic fatigue damage, International Journal of Fatigue, Volume 22, Issue 7, , August 2000, Pages 569-572.
22. T. Bucar, M. Nagode and M. Fajdiga, A neural network approach to describing the scatter of S-N curves, International Journal of Fatigue, Volume 28, Issue 4, , April 2006, Pages 311-323.
23. T. Bucar, M. Nagode and M. Fajdiga, An improved neural computing method for describing the scatter of S-N curves, International Journal of Fatigue, Volume 29, Issue 12, , December 2007, Pages 2125-2137.

24. Lechat, C., et al., Mechanical Behaviour of polyethylene terephthalate & polyethylene naphthalate fibers under cyclic loading. *Journal of Materials Science*, 2006. 41: p. 12.
25. Pecorini, T.J. and R.W. Hertzberg, The fracture toughness and fatigue crack propagation behaviour of annealed PET. *Polymer*, 1993. 34(24): p. 5053-5062.
26. Shuzo Sawada, K.K.S.O.K.Y., Degradation mechanisms of poly(ethylene terephthalate) tire yarn. *Journal of Applied Polymer Science*, 1991. 42(4): p. 1041-1048.
27. Hyun Hok Cho, K.H.L.Y.H.B., Effect of fine structure on fatigue resistance property of poly(ethylene terephthalate) tire cord fibers. *Journal of Applied Polymer Science*, 2000. 78(1): p. 90-100.
28. Herrera Ramirez, J. and A. Bunsell, Fracture initiation revealed by variations in the fatigue fracture morphologies of PA 66 and PET fibers, in *Journal of Materials Science*. 2005, Springer Science & Business Media B.V. p. 1269-1272.
29. Liang, T., et al., Effects of main chain rigidity on nonlinear dynamic viscoelasticity and fatigue performance for polymeric fibres. *Polymer*, 1998. 39(22): p. 5387-5392.
30. Le Clerc, C., A. Bunsell, and A. Piant, Influence of temperature on the mechanical behaviour of polyester fibers. *Journal of Materials Science*, 2006. 41: p. 15.
31. J. W. S. Hearle, R. Prakash, M. A. Wilding, Prediction of mechanical properties of nylon and polyester fibres as composites, *Polymer*, Volume 28, Issue 3, March 1987, Pages 441-448.
32. J. W. S. Hearle, S. C. Simmens, Electron microscope studies of textile fibres and materials, *Polymer*, Volume 14, Issue 6, June 1973, Pages 273-285.
33. J.W.S. Hearle, B. Lomas and W.D. Cooke, *Atlas of fibre fracture and damage to textiles* (2nd ed.), CRC Press, Boca Raton (1998).
34. C Lechat, AR Bunsell, P Davies, A Piant,. Mechanical behaviour of polyethylene terephthalate and polyethylene naphthalate fibres under cyclic loading. *Journal of Materials Science*, v. 41, n 6, March, 2006, p 1745-1756.
35. Ph Colomban, A Marcellan, AR Bunsell, R Piques. Micro-mechanisms, mechanical behaviour and probabilistic fracture analysis of PA 66 fibres. *Journal of Materials Science*, v. 38, n 10, May 15, 2003, p 2117-2123.
36. L Nasri, A Lallam, AR Bunsell. Fatigue failure in technical polyamide 66 fibers. *Textile Research Journal*, v. 71, n 5, May, 2001, p 459-466.

37. Ch Oudet, AR Bunsell. EFFECTS OF STRUCTURE ON THE TENSILE, CREEP AND FATIGUE PROPERTIES OF POLYESTER FIBRES. *Journal of Materials Science*, v. 22, n 12, Dec, 1987, p 4292-4298.
38. FATIGUE FAILURE AND ASSOCIATED MOLECULAR CHANGES IN POLYESTER FIBERS UNDER CYCLIC LOADING. Veve, J. Ch.; Bunsell, A. R.; Baillie, C.; Hagege, R. Source: *Kautschuk und Gummi Kunststoffe*, v 40, n 10, Oct, 1987, p 941-944.
39. FATIGUE AND CREEP FAILURE OF ORGANIC FIBRES SUBJECTED TO CYCLIC LOADING. Bunsell, A. R. Oudet, Ch.; Veve, J. Ch. Source: *Journal of Materials Science Letters*, v 5, n 11, Nov, 1986, p 1101-1103.
40. STRUCTURAL CHANGES IN POLYESTER FIBRES DURING FATIGUE. Bunsell, A. R., Oudet, Ch.; Veve, J. Ch.; Hagege, R.; Sotton, M. Source: *Plastics & Rubber Inst*, 1985, p 63. 1-63.
41. STRUCTURAL CHANGES IN POLYESTER FIBERS DURING FATIGUE. Oudet, Ch. (Ecole des Mines de Paris, Cent des Materiaux, Evry, Fr); Bunsell, A. R.; Hagege, R.; Sotton, M. Source: *Journal of Applied Polymer Science*, v 29, n 12 pt 2, Dec, 1984, p 4363-4376.
42. TENSILE FAILURE MECHANISMS IN CARBON FIBRE REINFORCED PLASTICS. Fuwa, M.; Bunsell, A. R.; Harris, B. Source: *Journal of Materials Science*, v 10, n 12, Dec, 1975, p 2062-2070.
43. FATIGUE OF SYNTHETIC POLYMERIC FIBERS. Bunsell, A. R.; Hearle, J. W. S. Source: *Journal of Applied Polymer Science*, v 18, n 1, Jan, 1974, p 267-291.
44. Michielsen S. The fracture toughness of single nylon 66 fibres. *J. Mater Sci Lett* 1992;11:982-4.
45. Adams GC, Bender RG, Crouch BA, Williams JG. Impact fracture toughness tests on polymers. *Polym Eng Sci* 1990;30(4):241-8.
46. Michielsen S. The effect of moisture and orientation on the fracture of nylon 66 fibers. *J Appl Polym Sci* 1994;52:1081-9.
47. Sandler, J.K.W., et al., A comparative study of melt spun polyamide-12 fibres reinforced with carbon nanotubes and nanofibres. *Polymer*, 2004. 45(6): p. 2001-2015.

48. Breton, Y., et al., Mechanical properties of multiwall carbon nanotubes/epoxy composites: influence of network morphology. *Carbon*, 2004. 42(5-6): p. 1027-1030.
49. Wuite, J. and S. Adali, Deflection and stress behaviour of nanocomposite reinforced beams using a multiscale analysis. *Composite Structures*, 2005. 71(3-4): p. 388-396.
50. Chen, W. and X. Tao, Production and characterization of polymer nanocomposite with aligned single wall carbon nanotubes. *Applied Surface Science*, 2006. 252(10): p. 3547-3552.
51. Jun Young Kim, H.S.P.S.H.K., Multiwall-carbon-nanotube-reinforced poly(ethylene terephthalate) nanocomposites by melt compounding. *Journal of Applied Polymer Science*, 2007. 103(3): p. 1450-1457.
52. Han Gi Chae, Marilyn L. Minus and Satish Kumar, Oriented and exfoliated single wall carbon nanotubes in polyacrylonitrile, *Polymer*, Volume 47, Issue 10, 3 May 2006, Pages 3494-3504.
53. Han Gi Chae, T.V. Sreekumar, Tetsuya Uchida and Satish Kumar, A comparison of reinforcement efficiency of various types of carbon nanotubes in polyacrylonitrile fiber, *Polymer*, Volume 46, Issue 24, 21 November 2005, Pages 10925-10935.
54. Jijun Zeng, Bethany Saltysiak, W. S. Johnson, David A. Schiraldi and Satish Kumar, Processing and properties of poly(methyl methacrylate)/carbon nanofiber composites, *Composites Part B: Engineering*, Volume 35, Issue 3, 2004, Pages 245-249.
55. Tetsuya Uchida, Thuy Dang, B.G. Min, Xiefei Zhang and Satish Kumar, Processing, structure, and properties of carbon nano fiber filled PBZT composite fiber, *Composites Part B: Engineering*, Volume 36, Issue 3, April 2005, Pages 183-187.
56. Satish Kumar, Harit Doshi, Mohan Srinivasarao, Jung O. Park and David A. Schiraldi, Fibers from polypropylene/nano carbon fiber composites, *Polymer*, Volume 43, Issue 5, March 2002, Pages 1701-1703.
57. Linda Vaisman, Ellen Wachtel, H. Daniel Wagner and Gad Marom, Polymer-Nanoinclusion Interactions in Carbon Nanotube Based Polyacrylonitrile Extruded and Electrospun Fibers, *Polymer*, In Press, Accepted Manuscript, Available online 28 September 2007.
58. T.D. Fornes, J.W. Baur, Y. Sabha and E.L. Thomas, Morphology and properties of melt-spun polycarbonate fibers containing single- and multi-wall carbon nanotubes, *Polymer*, Volume 47, Issue 5, 22 February 2006, Pages 1704-1714.

59. J. K. W. Sandler, S. Pegel, M. Cadek, F. Gojny, M. van Es, J. Lohmar, W. J. Blau, K. Schulte, A. H. Windle and M. S. P. Shaffer, A comparative study of melt spun polyamide-12 fibres reinforced with carbon nanotubes and nanofibres, *Polymer*, Volume 45, Issue 6, March 2004, Pages 2001-2015.
60. Chang, Y.N., Yang, P.C., Jin, Z., et al., 1996. Low molecular weight polylactic acid for controlled release of active agents. In: *Proceedings of the Corn Utilization Conference VI. National Corn Growers Association and National Corn Development Association*, St. Louis, MO, pp. 1-4.
61. Qi Fang, Milford A. Hanna, Rheological properties of amorphous and semicrystalline polylactic acid polymers, *Industrial Crops and Products*, Volume 10, Issue 1, June 1999, Pages 47-53.
62. Okuyama N, et al. Reduction of Retrosternal and Pericardial Adhesions With Rapidly Resorbable Polymer Films. *Ann Thorac Surg* 1999;68:913- 8.
63. Eren Ersoy, Vedat Ozturk, Aylin Yazgan, Mehmet Ozdogan, Haldun Gundogdu, Effect of Polylactic Acid Film Barrier on Intra-Abdominal Adhesion Formation, *Journal of Surgical Research*, Volume 147, Issue 1, 1 June 2008, Pages 148-152.
64. Marianne Strange, David Plackett, Martin Kaasgaard, Frederik C. Krebs, Biodegradable polymer solar cells, *Solar Energy Materials and Solar Cells*, Volume 92, Issue 7, Degradation and Stability of Polymer and Organic Solar Cells, July 2008, Pages 805-813.
65. Long Jiang, Jinwen Zhang, Michael P. Wolcott, Comparison of polylactide/nano-sized calcium carbonate and polylactide/montmorillonite composites: Reinforcing effects and toughening mechanisms, *Polymer*, Volume 48, Issue 26, 13 December 2007, Pages 7632-7644.
66. Yun Hui Lee, Jong Hoon Lee, In-Gu An, Chan Kim, Doo Sung Lee, Young Kwan Lee, Jae-Do Nam, Electrospun dual-porosity structure and biodegradation morphology of Montmorillonite reinforced PLLA nanocomposite scaffolds, *Biomaterials*, Volume 26, Issue 16, June 2005, Pages 3165-3172.
67. Freeman, James A. *Neural networks : algorithms, applications, and programming techniques*. Reading, Mass. : Addison-Wesley, c1991.
68. Abdi, Herve, A Neural Network Primer. *Journal of Biological Systems*. Vol 2(3), 247-283.
69. McCulloch, W.S., Pitts, W., A logical calculus of the ideas immanent in nervous activity. *Bull. Math. Phys.* 5 (1943) 115-133.

70. Rosenblatt F., The perceptron: a probabilistic model for information storage and organization in the brain. *Psychological Review* 65 (1958) 386-408.
71. Rosenblatt F., *Principles of Neurodynamics*. (Spartan Books, Washington, 1961).
72. Minsky M.L. and Papert S.A., *Perceptrons*. (MIT Press, Cambridge, 1969).
73. Functions of the Nervous System: Nerve Tissue.
http://training.seer.cancer.gov/module_anatomy/unit5_2_nerve_tissue.html.
74. Jones, D., 1999. Protein secondary structure prediction based on position-specific scoring matrices. *J. Mol. Biol.* 292 (1999).
75. Martin K. Dubois, Geoffrey C. Bohling and Swapan Chakrabarti, Comparison of four approaches to a rock facies classification problem, *Computers & Geosciences*, Volume 33, Issue 5, May 2007, Pages 599-617.
76. David Enke and Suraphan Thawornwong, The use of data mining and neural networks for forecasting stock market returns, *Expert Systems with Applications*, Volume 29, Issue 4, November 2005, Pages 927-940.
77. C.M. van der Walt and E. Barnard, "Data characteristics that determine classifier performance", in *Proceedings of the Sixteenth Annual Symposium of the Pattern Recognition Association of South Africa*, pp.160-165, 2006.
78. S. Lertworasirikul and Y. Tipsuwan, Moisture content and water activity prediction of semi-finished cassava crackers from drying process with artificial neural network, *Journal of Food Engineering*, Volume 84, Issue 1, , January 2008, Pages 65-74.
79. G. Santori, I. Fontana and U. Valente, Application of an Artificial Neural Network Model to Predict Delayed Decrease of Serum Creatinine in Pediatric Patients After Kidney Transplantation, *Transplantation Proceedings*, Volume 39, Issue 6, , July-August 2007.
80. Run Yu, PingSun Leung and Paul Bienfang, Predicting shrimp growth: Artificial neural network versus nonlinear regression models, *Aquacultural Engineering*, Volume 34, Issue 1, , January 2006, Pages 26-32.
81. Youngil Lim, Young-Sil Moon and Tae-Wan Kim, Artificial neural network approach for prediction of ammonia emission from field-applied manure and relative significance assessment of ammonia emission factors, *European Journal of Agronomy*, Volume 26, Issue 4.
82. Rojas, Raul. *Neural Networks - A Systematic Introduction*. Springer-Verlag, Berlin, New York, 1996.

83. C. Leone, G. Caprino and I. de Iorio, Interpreting acoustic emission signals by artificial neural networks to predict the residual strength of pre-fatigued GFRP laminates, *Composites Science and Technology*, Volume 66, Issue 2, Experimental Techniques and Design in Composite Materials, February 2006, Pages 233-239.
84. M. S. Al-Haik, H. Garmestani and A. Savran, Explicit and implicit viscoplastic models for polymeric composite, *International Journal of Plasticity*, Volume 20, Issue 10, October 2004, Pages 1875-1907.
85. Werbos, P.J., 1974. Beyond regression: new tools for prediction and analysis in the behavioral sciences. Ph.D. Dissertation, Applied Mathematics, Harvard University, Boston, MA.
86. Jan A. Snyman (2005). *Practical Mathematical Optimization: An Introduction to Basic Optimization Theory and Classical and New Gradient-Based Algorithms*. Springer Publishing.
87. Levenberg, K. "A Method for the Solution of Certain Non-Linear Problems in Least Squares." *Quart. Appl. Math.* 2, 164-168, 1944.
88. Marquardt, D. "An Algorithm for Least-Squares Estimation of Nonlinear Parameters." *SIAM J. Appl. Math.* 11, 431-441, 1963.
89. E.M. Bezerra, A.C. Ancelotti, L.C. Pardini, J.A.F.F. Rocco, K. Iha and C.H.C. Ribeiro, Artificial neural networks applied to epoxy composites reinforced with carbon and E-glass fibers: Analysis of the shear mechanical properties, *Materials Science and Engineering: A*, Volume 464, Issues 1-2, 25 August 2007, Pages 177-185.
90. Haykin, S., 1999. *Neural Networks: A Comprehensive Foundation*, second ed. Prentice-Hall, Englewood Cliffs, NJ.
91. Li, H.J., Qi, L.H., Han, H.M., Guo, L.J. Neural network modeling and optimization of semi-solid extrusion for aluminum matrix composites. *Journal of Materials Processing Technology* 151 (2004) 126-132.
92. M. Kemal Apalak, Mustafa Yildirim, Recep Ekici, Layer optimisation for maximum fundamental frequency of laminated composite plates for different edge conditions, *Composites Science and Technology*, Volume 68, Issue 2, , February 2008, Pages 537-550.
93. Li Aijun, Li Hejun, Li Kezhi, Gu Zhengbing, Applications of neural networks and genetic algorithms to CVI processes in carbon/carbon composites, *Acta Materialia*, Volume 52, Issue 2, 19 January 2004, Pages 299-305.

94. S. Suresh, P.B. Sujit, A.K. Rao, Particle swarm optimization approach for multi-objective composite box-beam design, *Composite Structures*, Volume 81, Issue 4, December 2007, Pages 598-605.
95. M. Abouhamze, M. Shakeri, Multi-objective stacking sequence optimization of laminated cylindrical panels using a genetic algorithm and neural networks, *Composite Structures*, Volume 81, Issue 2, November 2007, Pages 253-263.
96. Xia-Ting Feng, Chengxiang Yang, Genetic evolution of nonlinear material constitutive models, *Computer Methods in Applied Mechanics and Engineering*, Volume 190, Issue 45, 31 August 2001, Pages 5957-5973.
97. Surajit Pal, G. Wije Wathugala, Sukhamay Kundu, Calibration of a constitutive model using genetic algorithms, *Computers and Geotechnics*, Volume 19, Issue 4, 1996, Pages 325-348.
98. H. Sudarsana Rao, Vaishali G. Ghorpade, A. Mukherjee, A genetic algorithm based back propagation network for simulation of stress-strain response of ceramic-matrix-composites, *Computers & Structures*, Volume 84, Issues 5-6, January 2006, Pages 330-339.
99. NeuroSolutions Software. Copyright 2006 NeuroDimension, Inc. <http://www.neurosolutions.com/products/ns/>.
100. Rami Haj-Ali and Hoan-Kee Kim, Nonlinear constitutive models for FRP composites using artificial neural networks, *Mechanics of Materials*, Volume 39, Issue 12, December 2007, Pages 1035-1042.
101. L.A. Dobrzanski, M. Drak and J. Trzaska, Computer simulation of hard magnetic composite materials Nd-Fe-B properties, *Journal of Materials Processing Technology*, Volumes 192-193, The Seventh Asia Pacific Conference on Materials Processing (7th APCMP 2006), 1 October 2007, Pages 595-601.
102. Umesh Pendharkar, Sandeep Chaudhary and A.K. Nagpal, Neural network for bending moment in continuous composite beams considering cracking and time effects in concrete, *Engineering Structures*, Volume 29, Issue 9, September 2007, Pages 2069-2079.
103. E.M. Bezerra, A.C. Ancelotti, L.C. Pardini, J.A.F.F. Rocco, K. Iha and C.H.C. Ribeiro, Artificial neural networks applied to epoxy composites reinforced with carbon and E-glass fibers: Analysis of the shear mechanical properties, *Materials Science and Engineering: A*, Volume 464, Issues 1-2, 25 August 2007, Pages 177-185.

104. P. Cavaliere, Flow curve prediction of an Al-MMC under hot working conditions using neural networks, *Computational Materials Science*, Volume 38, Issue 4, February 2007, Pages 722-726.
105. N. Selvakumar, P. Ganesan, P. Radha, R. Narayanasamy and K.S. Pandey, Modelling the effect of particle size and iron content on forming of Al-Fe composite preforms using neural network, *Materials & Design*, Volume 28, Issue 1, 2007, Pages 119-130.
106. Yousef Al-Assaf and Hany El Kadi, Fatigue life prediction of composite materials using polynomial classifiers and recurrent neural networks, *Composite Structures*, Volume 77, Issue 4, February 2007, Pages 561-569.
107. Peter A. Lucon and Richard P. Donovan, An artificial neural network approach to multiphase continua constitutive modeling, *Composites Part B: Engineering*, Volume 38, Issues 7-8, October-December 2007, Pages 817-823.
108. C. Basaran, H. Tang and S. Nie, Experimental damage mechanics of microelectronic solder joints under fatigue loading, *Mechanics of Materials*, Volume 36, Issue 11, , November 2004, Pages 1111-1121.
109. Ju, J.W., 1989. On energy-based coupled elastoplastic damage theories: constitutive modeling and computational aspects. *International Journal of Solids and Structures* 25 (7), 803–833.
110. Dasgupta, A., Oyan, C., Barker, D., Pecht, M., 1992. Solder creep-fatigue analysis by an energy-partitioning approach. *Trans. ASME, Journal of Electronic Packaging* 114, 152–160.
111. Hayakawa, K., Murakami, S., 1997. Thermodynamical modeling of elastic–plastic damage and experimental validation of damage potential. *International Journal of Damage Mechanics* 6, 333–363.
112. Basaran, C., Yan, C., 1998. A thermodynamic framework for damage mechanics of solder joints. *Journal of Electronic Packaging, Trans. ASME* 120, 379–384.
113. Basaran, C., Tang, H., 2002. Implementation of a thermodynamic framework for damage mechanics of solder interconnects in microelectronics packaging. *International Journal of Damage Mechanics* 11, 87–108.
114. Basaran, C., Chandaroy, R., 1998. Mechanics of Pb40/Sn60 near-eutectic solder alloys subjected to vibration. *Applied Mathematical Modeling* 22, 601–627.
115. Chow, C.L., Yang, F., 1998. Damage mechanics characterization on fatigue behavior of a solder joint material. *ASME International Mechanical Engineering Congress Exposition, Anaheim, CA*, pp. 1–13.

116. Qian, Z., Ren, W., Liu, S., 1999. A damage coupling framework of unified viscoplasticity for the fatigue of solder alloys. *Journal of Electronic Packaging* 121, 162–168.
117. Lemaitre, J., Chaboche, J.L., 1990. *Mechanics of Solid Materials*. Cambridge University Press.
118. Basaran, C., Jiang, J., 2002. Measuring intrinsic elastic modulus for Pb/Sn solder alloys. *Mechanics of Materials* 34, 349–362.
119. Lemaitre, J., 1990. *A Course on Damage Mechanics*, second ed. Springer.
120. Kachanov, L.M., 1986. *Introduction of Continuum Damage Mechanics*. Martinus, Nijhoff, Dordrecht.
121. F.A. Jenkins, H.E. White, *Fundamental of Optics*, McGraw-Hill, 1981, p. 231.
122. Joao M. P. Coelho, Manuel A. Abreu, F. Carvalho Rodrigues, Methodologies for determining thermoplastic films optical parameters at 10.6 μm laser wavelength, *Polymer Testing*, Volume 23, Issue 3, May 2004, Pages 307-312.
123. W. C. J. Zuiderduin, C. Westzaan, J. Huetink, R. J. Gaymans, Toughening of polypropylene with calcium carbonate particles, *Polymer*, Volume 44, Issue 1, January 2003, Pages 261-275.
124. A. S. Argon, R. E. Cohen, Toughenability of polymers, *Polymer*, Volume 44, Issue 19, In Honour of Ian Ward's 75th Birthday, September 2003, Pages 6013-6032.
125. M. Pluta, J.K. Jeszka, G. Boiteux, Polylactide/montmorillonite nanocomposites: Structure, dielectric, viscoelastic and thermal properties, *European Polymer Journal*, Volume 43, Issue 7, July 2007, Pages 2819-2835.
126. Ward IM. Mechanical behavior of poly(ethylene terephthalate). *J. Macromol Sci, Phys* 1967;1(4):667-94.
127. Q. Yuan, R.D.K. Misra, Impact fracture behavior of clay-reinforced polypropylene nanocomposites, *Polymer*, Volume 47, Issue 12, 31 May 2006, Pages 4421-4433.
128. Ma, H., et al., Processing, structure, and properties of fibers from polyester/carbon nanofiber composites. *Composites Science and Technology*, 2003. 63(11): p. 1617-1628.

129. Averett, R.D., et al., Mechanical behavior of nylon 66 fibers under monotonic and cyclic loading. *Composites Science and Technology*, 2006. 66(11-12): p. 1671-1681.
130. Mostaghel, N. and R.A. Byrd, Inversion of Ramberg-Osgood equation and description of hysteresis loops. *International Journal of Non-Linear Mechanics*, 2002. 37(8): p. 1319-1335.
131. Herrera Ramirez, J. and A. Bunsell, Fracture initiation revealed by variations in the fatigue fracture morphologies of PA 66 and PET fibers, in *Journal of Materials Science*. 2005, Springer Science & Business Media B.V. p. 1269-1272.
132. Brown, N. and I. Ward, Load Drop at the Upper Yield of a Polymer. *Journal of Polymer Science: Part A-2*, 1968. 6: p. 607-620.
133. Mullins, L., Softening of Rubber by Deformation. *Rubber Chemistry and Technology*, 1969. 42: p. 339-362.
134. Achibat, T., et al., Low-frequency Raman spectroscopy of plastically deformed poly(methyl methacrylate). *Polymer*, 1995. 36(2): p. 251-257.
135. Aoyama, T., et al., Strain recovery mechanism of PBT/rubber thermoplastic elastomer. *Polymer*, 1999. 40(13): p. 3657-3663.
136. Cunningham, A., et al., An infra-red spectroscopic study of molecular orientation and conformational changes in poly(ethylene terephthalate). *Polymer*, 1974. 15(11): p. 749-756.
137. Hutchinson, I.J., et al., Infra-red measurements on one-way drawn poly(ethylene terephthalate) films subjected to constant strain. *Polymer*, 1980. 21(1): p. 55-65.
138. Sakin, Raif, Ay, Irfan. Statistical analysis of bending fatigue life data using Weibull distribution in glass-fiber reinforced polyester composites. *Materials and Design*, v 29, n 6, 2008, p 1170-1181.
139. Uma Divakaran and Amit Dutta. Critical behavior of random fibers with mixed Weibull distribution. *Physical Review E - Statistical, Nonlinear, and Soft Matter Physics*, v 75, n 1, 2007, p 011109.
140. Zafeiropoulos, N.E. and Baillie, C.A. A study of the effect of surface treatments on the tensile strength of flax fibres: Part II. Application of Weibull statistics. *Composites Part A: Applied Science and Manufacturing*, v 38, n 2, February, 2007, p 629-638.
141. W. Weibull. A statistical function of wide applicability. *Journal of Applied Mechanics*, 18 (1951) pp. 293-297.

142. N.L. Post, J. Cain, K.J. McDonald, S.W. Case, J.J. Lesko, Residual strength prediction of composite materials: Random spectrum loading, *Engineering Fracture Mechanics*, Volume 75, Issue 9, *Fracture of Composite Materials*, June 2008, Pages 2707-2724.
143. R.M. Guedes, Durability of polymer matrix composites: Viscoelastic effect on static and fatigue loading, *Composites Science and Technology*, Volume 67, Issues 11-12, , September 2007, Pages 2574-2583.
144. S. J. V. Frankland and V. M. Harik, Analysis of carbon nanotube pull-out from a polymer matrix, *Surface Science*, Volume 525, Issues 1-3, 10 February 2003, Pages L103-L108.
145. S.C. Chowdhury and T. Okabe, Computer simulation of carbon nanotube pull-out from polymer by the molecular dynamics method, *Composites Part A: Applied Science and Manufacturing*, Volume 38, Issue 3, March 2007, Pages 747-754.
146. Yuan Qinlu, Li Yulong, Li Hejun, Li Shuping, Guo Lingjun, Quasi-static and dynamic compressive fracture behavior of carbon/carbon composites, *Carbon*, Volume 46, Issue 4, , April 2008, Pages 699-703.
147. Yueping Ye, Haibin Chen, Jingshen Wu, Lin Ye, High impact strength epoxy nanocomposites with natural nanotubes, *Polymer*, Volume 48, Issue 21, , 5 October 2007, Pages 6426-6433.
148. Nathan L. Post, John Bausano, Scott W. Case, John J. Lesko, Modeling the remaining strength of structural composite materials subjected to fatigue, *International Journal of Fatigue*, Volume 28, Issue 10, , The Third International Conference on Fatigue of Composites, October 2006, Pages 1100-1108.
149. Lu XF and Hay JN. Crystallization orientation and relaxation in uniaxially drawn poly(ethylene terephthalate). *Polymer* 42 (2001) 8055-8067.
150. Tibbetts, GG and McHugh, JJ. Mechanical properties of vapor-grown carbon fiber composites with thermoplastic matrices. *Journal of Materials Research*. Vol. 14, No. 7, Jul 1999.
151. H.L. Cox, *Brit. J. Appl. Phys.* 3, 72 (1982).
152. G.G. Tibbetts, in *Carbon Fibers Filaments and Composites* (Kluwer Academic Publishers, The Netherlands, 1990), p. 73.
153. Andrews, E.H., in R.N. Haward (ed): "The Physics of Glassy Polymers," Chap 7, Wiley, New York, 1973.

154. Bassir DH et al., Hybrid computational strategy based on ANN and GAPS: Application for identification of a non-linear model of composite material, *Compos Struct* (2008), doi:10.1016/j.compstruct.2008.04.007.
155. A.K. Maiti et al. An application of real-coded genetic algorithm (RCGA) for mixed integer non-linear programming in two-storage multi-item inventory model with discount policy. *Applied Mathematics and Computation* 183 (2006) 903–915.